AGH UNIVERSITY OF SCIENCE AND TECHNOLOGY

FIELD OF SCIENCE ENGINEERING AND TECHNOLOGY

SCIENTIFIC DISCIPLINE INFORMATION AND COMMUNICATION TECHNOLOGY

DOCTORAL DISSERTATION

Integrated Sensing and Communication Using Random-Padded Orthogonal Time Frequency Space Modulation

Author: Pavel Karpovich

Supervisor: Prof. Tomasz P. Zieliński, PhD, DSc

Completed at: Faculty of Computer Science, Electronics and Telecommunications

Kraków, 2025

Special thanks to my academic advisor, prof. Tomasz P. Zieliński, for his support not only in scientific and technical matters, but also in uplifting my morale. I would also like to thank the team from the Politechnika Warszawska (Karol Abratkiewicz, Piotr Samczyński and Radoslaw Maksymiuk and others) for very fruitfill discussions and conducting the practical experiment. My gratitude goes to my mother, who scolded me when I did not want to study, and to my wife, who did not scold a lot me when I finally did. Also thank to my kids who gave me the strength to finish this dissertation.

Abstract

Integrated Sensing and Communication (ISAC) is an increasingly active area of research because of its potential to combine sensing and communication functions within a single system. A key advantage of ISAC is the ability to share information between the radar and communication components, thereby improving the overall performance of the system. Orthogonal Frequency Division Multiplexing (OFDM) is a widely adopted waveform in modern communication standards such as 5G, LTE, and DVB-T2, and is also commonly used in ISAC systems. However, as carrier frequencies increase—particularly in 5G systems beyond, OFDM becomes less effective due to susceptibility to the Doppler effect.

To address this challenge, a new class of waveforms, known as Orthogonal Time Frequency Space (OTFS), has been developed. In this Ph.D. thesis, we propose a novel variant: Random-Padded OTFS (RP-OTFS). This waveform is specifically designed to enhance communication performance in high-Doppler environments and improve radar sensing capabilities in ISAC systems.

RP-OTFS introduces a dedicated pilot zone in the resource grid. Unlike existing OTFS-based schemes, the pilot zone in RP-OTFS does not contain zero padding, enabling a potentially higher signal-to-noise ratio (SNR) for reference/pilot signals. We demonstrate the superiority of RP-OTFS over conventional OTFS and OFDM waveforms in terms of communication reliability under strong Doppler conditions and target detection performance.

We also analyze the limitations of RP-OTFS. Specifically, our method assumes quasi-static channel impulse responses (CIRs) within the pilot zone, which is a common assumption in OFDM. However, since the pilot zone in RP-OTFS is significantly shorter than in conventional OFDM symbols, the validity period of this assumption is reduced.

A significant contribution of this work is the development of a new channel equalization method. To reduce inter-carrier interference (ICI) and interference between multiple devices sharing the same resource grid, we propose a transmitter-side channel orthogonalization technique, conceptually similar to strategies used in MIMO systems.

Furthermore, we investigate the application of RP-OTFS for radar purposes, including optimization of resource grid parameters for various radar use cases. The dissertation concludes with the presentation of practical simulation and experimental results that validate the proposed concepts.

In summary, in this work the following thesis was put forward and proofed: *It is possible to design a better OTFS modulation scheme than Zero-Padded OTFS which offers lower BER in a communication/transmission part and higher PNFR in a sensor/radar part of the integrated sensing and communication (ISAC) system working in high Doppler environment.*

Streszczenie

Zintegrowane wykrywanie i komunikacja (ISAC - Integrated Sensing and Communication) to obecnie intensywnie rozwijający się obszar badań ze względu na możliwość połączenia dwóch funkcji w jednym urządzeniu. Dodatkowo, w urządzeniach ISAC jest możliwa wymiana danych między częścią radarową a telekomunikacyjną w celu poprawy jakości usług. Fala nośna OFDM (Orthogonal Frequency Division Multiplexing) jest de facto standardem w nowoczesnych systemach komunikacyjnych (5G NR, 4G LTE, DVB-T2, DVB-S2, itd.) i jest również szeroko stosowana w systemach ISAC. Jednakże wzrost częstotliwości nośnej, np. w systemach 5G i 6G („poza 5G"), sprawia, że stosowanie OFDM staje się problematyczne z powodu efektu Dopplera. W związku z tym opracowano niedawno nową technikę transmisji radiowej, nazwaną Orthogonal Time Frequency Space (OTFS).

W niniejszej pracy doktorskiej zaproponowano nową wersję OTFS o nazwie Random-Padded Orthogonal Time Frequency and Space (RP-OTFS), mającą na celu: 1) przezwyciężenie problemów OFDM podczas transmisji danych w środowiskach z silnym efektem Dopplera oraz 2) optymalizację działania radaru w systemie ISAC. RP-OTFS posiada dedykowaną strefę pilotów na swojej siatce zasobów, tzw. pilot zone. W przeciwieństwie do innych wersji OTFS, konfiguracja strefy pilotowej w RP-OTFS nie zawiera zer, co zapewnia wyższy stosunek sygnału do szumu (SNR) dla sygnałów referencyjnych/pilotów. W rozprawie doktorskiej pokazano przewagę RP-OTFS nad innymi znanymi nam wersjami OTFS oraz nad OFDM w kontekście telekomunikacji w warunkach silnego efektu Dopplera i detekcji obiektów.

W pracy omówiono także ograniczenia RP-OTFS. W przypadku RP-OTFS zakłada się stałość (lub prawie stałość) odpowiedzi impulsowej kanału (CIR - Channel Impulse Response) w strefie pilotowej. To samo założenie przyjmuje się w OFDM, jednakże w RP-OTFS czas trwania strefy pilotowej jest znacznie krótszy niż czas trwania konwencjonalnego symbolu OFDM. To powoduje, że wymagany czas „stałości" CIR jest znacznie krótszy.

W głównej części pracy rozważono konkretne przykłady zastosowania RP-OTFS w radarze. Zoptymalizowano wartości parametrów siatki zasobów dla różnych scenariuszy radarowych. Rozpatrzono dwa podejścia do projektowania radaru opartego na RP-OTFS.

Pracę kończy prezentacją otrzymanych wyników praktycznych, symulacyjnych i pomiarowych, które potwierdzają efektywność zaproponowanej metody.

Podsumowując, w pracy postawiono i udowodniono nastepującą tezę: *Możliwe jest zaprojektowanie lepszej modulacji OTFS niż ZP-OTFS, która zaoferuje niższy BER w części telekomunikacyjnej/transmisyjnej oraz wyższy PNFR w części radarowej/sensorowej systemu telekomunikacyjno-radarowego ISAC, pracującego w środowisku z silnym efektem Dopplera.*

Contents

List of Figures

Chapter 1

Introduction

1.1 State of the Art, Motivation and Goals

As 5G communication systems were delivered in 2019, today the scientific community is focused on next-generation systems, called 6G. Currently, there is no official specification for 6G from the 3rd Generation Partnership Project (3GPP) group, but there are many publications on the vision of 6G systems — the most noticeable are [5], [6]. There are different opinions on some aspects of 6G. At the same time, there are some common points in most of the articles: increasing the scale of massive Multiple Input, Multiple Output (mMIMO) technology, the usage of intelligent reflecting surfaces (IRS) [7], a more reliable network with more spectral efficiency, the use of artificial intelligence (AI) technologies [8], etc., but the most important of the common points for new waveform research are higher operating frequencies and the emergence of Integrated Sensing and Communication (ISAC) [9] [10] [11].

The increase in operating carrier frequency is the answer to the demand for an increasing data rate for potential 6G applications, for example, holographic video calls [6]. But this also brings new challenges. One of the main problems in physical layer processing is the Doppler effect. From a Doppler frequency shift point of view, the increase in the carrier frequency will further aggravate the situation, as the Doppler shift is directly proportional to the carrier frequency. The Orthogonal Frequency Division Multiplexing (OFDM) wavefrom (de facto the standard waveform for most modern communication systems since the mid-1990s) assumes that the channel impulse response during the OFDM symbol does not change. In environments with strong Doppler effects, this assumption is violated. As a result, the orthogonality between subcarriers is lost, leading to inter-carrier interference (ICI). This limits the performance of OFDM systems in high-mobility scenarios, making their use problematic under such conditions. For example, in 5G special numerologies for frequency range 2 (FR2 - above 24 GHz) [12] were introduced to make OFDM symbols shorter and to keep the subcarriers away from each other [13]. But this also has its own drawback: more bandwidth is occupied for the same number of subcarriers. To reduce the cyclic prefix (CP) overhead rate, the length of the CP also decreases proportionally to the length of the OFDM symbol, and this will limit the maximum allowed channel impulse response length [14].

The Orthogonal Time Frequency Space (OTFS) waveform was designed to ensure reliable communication in a strong Doppler environment. OTFS is a two-dimensional transmission technique that modulates data in the Doppler-delay (DD) domain. This new modulation is very attractive for ISAC systems, as in the case of OTFS both parts of the system (sensing/radar and communication) use the DD domain to represent the data [15]. More details on OTFS can be found in [16] [4], [17], [18].

In [19] a good comparison is made between OFDM and OTFS waveforms in terms of the achievable communication rate. In this work, the authors explicitly address the problem of channel estimation by considering a pilot scheme adapted to the sparse channels in the DD domain for both simulations. Different time frequency selective channels are considered here, the channel state information (CSI) results from the considered pilot schemes. The paper shows that OTFS offers a better bit rate performance compared to its OFDM counterpart for static channels under practical channel estimation and detection approaches. We made a similar comparison of performance in [20]. In our paper, we used a very simple pilot configuration for OTFS. To put both modulation under the same conditions, we used equivalent pilot power criteria. In both papers ([19] and [20]), it is shown that OTFS achieves a more robust performance than OFDM for high-mobility channels.

The paper [21] investigates the performance of coded OTFS in terms of diversity gain and coding gain. It shows that there is a fundamental trade-off between the coding gain and the diversity gain for the OTFS systems; that is, the diversity gain of the OTFS systems improves with the number of resolvable paths, while the coding gain declines. The error performance for the coded OTFS system is evaluated for the high mobility channel. Here, the authors use the OFDM waveform as a baseline in their research; therefore, we obtain the performance comparison for both waveforms: OTFS and OFDM.

As noted above, the usage of the DD domain makes OTFS very attractive from the ISAC point of view. In general, there are two main approaches to radar detection in ISAC systems, based on the estimation of: 1) the cross-ambiguity function (CAF) [22], or 2) the channel state information (CSI) [9]. The CAF-based processing practically does not depend on the waveform. This means that for the OTFS, the processing chain could be the same as for the OFDM [23]. However, the CSI-based approach uses pilot-based channel estimation for moving object detection, so pilot configuration in case of CSI-based sensing plays a very important role.

A Zero-Padded OTFS (ZP-OTFS) has the most simple pilot configuration among all existing configurations. It has a dedicated pilot zone with only one active carrier in its center, all other carriers in the pilot zone are inactive, i.e. equal to zero. The visualization of ZP-OTFS is shown in Figure 2.4. Due to a low number of active carriers and a large number of inactive carriers, ZP-OTFS is not very efficient and its modification, ZP-BOX-OTFS, was introduced in [24]. The ZP-BOX-OTFS waveform has more active carriers in the pilot zone of the DD grid, but is more complex from a computational point of view. Another important advantage of ZP-BOX-OTFS over the ZP-OTFS is a significant reduction of the peak-to-average power ratio (PAPR). In the paper [25], the authors provide a detailed analysis of the application of the message passing (MP) algorithm for CSI estimation in the case of ZP-BOX-OTFS. The Cramer-Rao lower band (CRLB) is delivered to verify the performance of different algorithms for the ZP-BOX-OTFS CSI estimation. The PAPR analysis in the context of ZP-BOX-OTFS is also provided in the paper.

The uncommon approach to pilot configuration and channel estimation is presented in [26]. Here, there is no dedicated pilot zone on the DD grid. Both pilot and data symbols are superimposed on all DD grid cells in an OTFS frame. In the paper, two approaches to channel estimation and data detection are considered. In the first, the data component in the DD cells is considered as a signal that interferes with pilots during the channel estimation procedure. The large number of pilot cells allows one to significantly increase the signal-interference-to-noise ratio (SINR). Later, during bit detection, the pilot component is considered as interfering, but it could be eliminated as pilots are known and the receiver has CSI estimation. The second approach uses iterative switching between channel estimation and data detection procedures and results in higher performance, especially for a high input SNR.

In turn, a random padded OTFS (RP-OTFS), a hybrid method, takes advantage of the OTFS technique for data and makes use of very short OFDM symbols as pilots [27]. The initial channel impulse response (CIR) estimation itself is performed in the time-frequency (TF) domain, by means of these very short OFDM symbols having pilots only. The final RP-OTFS CSI estimate is computed by exploiting initial instantaneous CIR estimations from the TF domain. Basically, RP-OTFS is a compromise between the strictly DD pilot configuration, such as ZP-OTFS, and the strictly TF pilot configuration, as it is done in OFDM. The advantages of RP-OTFS are the low computational complexity and the ability to use well-known OFDM channel estimation approaches to OTFS after some adaptations. However, too high Doppler in the channel may corrupt the estimation results, as pilots in RP-OTFS are still OFDM symbols.

All of the methods described above result in the estimation of CSI in the DD domain. And this is, in fact, a significant part of the radar signal processing. The first study in the literature of OTFS-based sensing and communication is in [28]. The scenario that is considered here includes a monostatic radar wishing to communicate data to its target - the receiver, while estimating the parameter of interest related to this receiver (target). It is assumed that the receiver has already been detected, and thus only the parameter estimation question is considered in the paper. For the radar parameter estimation part, the authors of the paper derive an efficient approximated Maximum Likelihood (ML) algorithm and the corresponding CRLB for range and velocity estimation. It is shown that OTFS can achieve as accurate radar estimation as state-of-the-art performance in frequency-modulated continuous wave (FMCW) radar and at the same time transmit data. Moreover, OTFS has been shown to perform better than OFDM in terms of channel capacity and overhead. The paper [29] presents a framework for OTFS-based ISAC systems in vehicular networks. Using the time variation of the OTFS channel, the delay and Doppler shifts obtained from sensing of the echoes can be employed to infer the communications channel, which is similarly characterized by delays and Doppler shifts. Consequently, a novel data frame structure is designed to fully exploit the DD grids, thereby reducing the overhead for channel estimation. An iterative receiver is proposed to continuously update channel information and detect data symbols. The simulation results indicate that the sensing information can enhance the performance of OTFS-based communication. The OTFS-ISAC system with spatial spreading (SS) is considered in [30]. The most important conclusion in this paper is that the power allocation should be designed leaning towards sensing in a practical SS-OTFS-based ISAC system.

The first practical results of the OTFS-ISAC system can be found in our paper [31]. In this article, multiple velocity scenarios for the OTFS-ISAC system are simulated, to estimate the potential root mean square error (RMSE) in the target parameter estimation. The practical part of the paper shows successful data transmission and radar detection at the same time in an urban area. In the practical part, comparison of different radar detection methods (based on CSI and CAF), different pilot configurations, and primary radar parameters (such as integration time) are reported.

From a communication point of view, CSI estimation and bit detection are the most challenging parts of the processing, both for OTFS and OFDM waveforms. In case of the OTFS additional difficulties arise when the parameters of the reflections (delay and Doppler offsets) are not consistent with the DD grid.

Reflection inconsistency with the DD grid could be in the delay direction, Doppler direction, or both at the same time. These effects are known as fractional delay, fractional Doppler shift, or fractional reflection, respectively [32, 33, 34]. Creating a guard interval between the pilot and the data zone in RP-OTFS adds additional overhead. Also, because of a limited number of estimated samples of the CSI in the case of RP-OTFS (and also in ZP-OTFS and others), the CSI oscillations from the fraction reflections cannot be estimated directly. The accuracy of the CSI estimation is extremely important not only for communication but also, as mentioned before, for radar. In the paper [35], we examine the problem of interference between pilot carriers and data carriers and propose its solutions.

For the bit detection common methods, that are well known for OFDM, could be used, but some of them should be modified to work in the OTFS environment. A good overview of different bit detection approaches is given in [36]. The paper [4] introduces the maximum rate combining (MRC) method for OTFS bit detection. MRC combines interfering components from different DD cells to increase the SINR of each cell of the grid. The article [4] also provides a very good mathematical framework for the OTFS data transmission system model.

The work [37] introduces low-complexity realization of both zero-forcing (ZF) and MMSE detectors for the OTFS. The processing is based on exploiting the block circulant structure of the OTFS channel matrix, which enables its diagonalization via Kronecker products of discrete Fourier transform (DFT) matrices. This allows expressing the detectors in terms of the eigenvalues of the channel matrix, thereby avoiding large matrix inversions and significantly reducing computational complexity.

The neural network-based bit detection approach in the context of OTFS is presented in [38]. Using reservoir computing (a special recurrent neural network), it is shown that the resulting one-shot online learning is sufficiently flexible to cope with channel variations among different OTFS frames. The main benefit is that the proposed scheme does not rely on the knowledge of explicit channel state information. Moreover, a better trade-off between the processing complexity and the equalization performance is achieved for OTFS modulation compared to its neural network-based counterparts for OFDM.

This work focuses on the novel waveform RP-OTFS, which was introduced in our work [27]. This waveform is specifically designed to enhance communication performance in high-Doppler environments and improve radar sensing capabilities in ISAC systems.

RP-OTFS introduces a dedicated pilot zone in the resource grid. Unlike existing OTFS-based schemes, the pilot zone in RP-OTFS does not contain zero padding, enabling a potentially higher signal-to-noise ratio (SNR) for pilot signals. We demonstrate the superiority of RP-OTFS over conventional OTFS and OFDM waveforms in terms of communication reliability under strong Doppler conditions and target detection performance.

We also analyze the limitations of RP-OTFS. Specifically, our method assumes quasi-static CIRs within the pilot zone, which is a common assumption in OFDM. However, since the pilot zone in RP-OTFS is significantly shorter than in conventional OFDM symbols, the validity period of this assumption is reduced.

A significant contribution of this work is the development of a new channel equalization method with reduced ICI.

Furthermore, we investigate the application of RP-OTFS for radar purposes, including optimization of resource grid parameters for various radar use cases. The dissertation concludes with the presentation of practical simulation and experimental results that validate the proposed concepts.

1.2 Thesis and Publications

In summary, in this work **the following thesis was put forward and proofed:** ***It is possible to design a better OTFS modulation scheme than Zero-Padded OTFS which offers lower BER in a communication/transmission part and higher PNFR in a sensor/radar part of the integrated sensing and communication (ISAC) system working in a high Doppler environment.***

The results presented in this Ph.D. thesis have already been published in a series of publications [27, 20, 39, 40, 41, 42, 31]. The historical perspective of our work on RP-OTFS is given in the following.

An investigation of the baseline waveform ZP-OTFS, taking into account various bit detection algorithms, is presented in [20].

An apparent drawback of ZP-OTFS, the large number of zeros in the pilot region, was initially considered by us primarily from the radar system perspective. Our first publication on this topic is [27]. In this work, we proposed RP-OTFS and examined the RP-OTFS based ISAC system mainly in the context of CAF-based radar processing. The main results demonstrated that, at least from the CAF-based approach perspective, RP-OTFS enables target detection at lower SNR levels. In addition, communication performance also showed improvements, particularly in high-speed train (HST) channel scenarios.

At the IEEE International Communication Conference ICC-2023, we presented the first practical results of an ISAC system based on RP-OTFS [39]. The conducted experiment successfully demonstrated simultaneous data transmission and vehicle detection. In these tests, we still considered RP-OTFS as a CAF-based radar system within the ISAC framework. The results of the second part of this experiment, in which ZP-OTFS was used instead of RP-OTFS, are presented in [40] at the 2023 IEEE Radar Conference.

A more detailed study of the RP-OTFS receiver in terms of channel estimation was presented in [41]. Various interpolation techniques were employed to reconstruct the channel impulse response. The analysis was performed for different modulation orders and channel types.

The results of a comparison between two radar detection approaches, CAF-based and CIR-based, for RP-OTFS are presented in [42].

The results of our second practical experiment are presented in [31]. In this case, the performance of CAF-based and CIR-based radar approaches was compared. Simultaneous data transmission was also carried out during the experiment. For the RP-OTFS-based CIR-based ISAC system, unlike in the previous experiment, only a single antenna was used.

The latest simulation results are presented in [43]. The article is mainly devoted to methods of reducing interference, both within the RP-OTFS symbol itself and from multiple users simultaneously sharing the same DD grid.

1.3 Outline

The outline of the thesis is as follows.

Chapter 2 provides the theoretical background necessary to understand the operation of ISAC systems based on RP-OTFS. We begin with an explanation of the OTFS waveform designed to address the challenges of data transmission over doubly selective channels. Next, we examine the properties and issues associated with such channels and formally define their most important parameters. This section also includes an important note on the limitations of OFDM performance in doubly selective environments. Then we present an overview of signal detection algorithms for OTFS reception. Finally, the chapter focuses on the radar subsystem, where we describe the fundamentals of two main target detection approaches, the CAF and CIR ones, as well as the specific characteristics of bistatic radar geometry.

Chapter 3 gives a detailed description of the novel RP-OTFS waveform. We begin by discussing the DD grid structure specific to RP-OTFS. We then analyze the physical characteristics of the signal, such as the PAPR and levels of the ICI, both within the pilot cells and between pilots and data symbols. Strategies are proposed to mitigate the impact of these interferences. Subsequently, we address RP-OTFS signal transmission, including pilot generation and placement on the grid, as well as reception procedures such as channel estimation and bit detection. The chapter concludes with a discussion of the radar subsystem in the context of OTFS, along with considerations for selecting appropriate grid parameters.

Chapter 4 presents, analyzes, and discusses the results obtained from both simulations and real-world experiments, providing a comprehensive evaluation of the proposed RP-OTFS-based ISAC system.

The thesis ends with conclusions, a list of references, and an appendix presenting features of the Zak transform.

Chapter 2

Theoretical Basics

In many modern wireless systems, the transmitter and/or receiver are/is mobile. Even if both link ends are static, scatters, i.e. objects that reflect, scatter, or diffract the propagating waves, may move with significant velocities. These situations give rise to time variations of the wireless channel due to the Doppler effect. The growth of the operating carrier frequency further increases the Doppler influence.

In conditions of multipath propagation and high Doppler frequency shift, the channel should be considered as *doubly selective*. The doubly selective channels are also termed TF dispersive or doubly dispersive, as well as TF selective.

The OFDM waveform is primarily intended for operation in frequency-selective channels. Thus, the use of OFDM in the case of time-selective channels is limited. Moreover, the use of OFDM in doubly selective channels is even more problematic. In this chapter, we begin with describing a new modulation technique that uses the DD domain to transmit data, namely the OTFS. Also, here we discuss the OTFS-specific properties that result from the Zak transform (ZT) features listed in appendix A. After that, we will discuss the double selective channel in the context of the DD domain. Here, we present the fundamental equations that will be used throughout this work. After the channel is described, we provide an overview of the OTFS signal receivers. The chapter concludes with a description of the radar subsystem as part of the ISAC framework.

2.1 Modulation in Delay-Doppler Domain

2.1.1 General Considerations

In this section, our starting point will be the time-delay (or *slow time - fast time*) domain signal representation or the time-delay (TD) grid. The TD data representation is often used in radar signal processing; for example, in classical Radar Data Cubes, there are three dimensions: fast time, slow time, and space. In the context of communication, the TD signal representation is obtained by division of a time signal into N pieces by samples M and combining these pieces into a 2D matrix $\mathbf{X}$. The discrete-time baseband signal $x[q]$ can be transformed to the TD domain by a simple transformation:

$$\mathbf{X} = \begin{bmatrix} x_{0,0} & x_{0,1} & \cdots & x_{0,N-1} \\ x_{1,0} & x_{1,1} & \cdots & x_{1,N-1} \\ \vdots & \vdots & \ddots & \vdots \\ x_{M-1,0} & x_{M-1,1} & \cdots & x_{M-1,N-1} \end{bmatrix}, \tag{2.1}$$

$$x_{m,n} = x[m + nM]. \tag{2.2}$$

Starting from TD-domain signal representation and applying the Fourier transform in different directions, the signal can be represented in several domains - see Figure 2.1. An important point is that each domain provides a specific representation not only of the signal but also of the CSI.

The domains are as follows:

- TD domain - the most basic domain; usually the CSI is denoted by $h(t, \tau)$, i.e. the time-varying channel impulse response;
- TF domain - this domain is used for OFDM modulation of carriers; the CSI is denoted $H(t, f)$, i.e. time-varying channel frequency response;
- DD domain - this domain is used in OTFS modulation of carriers; the CSI is denoted $G(\nu, \tau)$, i.e. Doppler-delay channel response;
- Doppler-frequency domain - there are limited cases of usage of this domain, it is out of the scope of this work.

The relationship between these domains is explained in Figure 2.1. The three domains of greatest interest to us are: TD, TF, and DD. TD domain is closely connected to the time domain through a simple expression (2.2). Therefore, it is convenient to use it instead of the time domain, while preserving the 2D matrix with dimensions M by N. We will often address the TF domain as a baseline in our research, because the OFDM waveform uses the TF domain for bit allocation. Finally, it is important to highlight the first advantage of using the DD domain for bit allocation in the context of ISAC systems. When using OTFS (a modulation scheme that operates in the DD domain): the modulation of information bits, the channel estimations, and the target detection take place within the same domain. This could reduce the processing overhead of the ISAC system because some parts of the processing cloud be shared between bit demodulation and target detection. In addition, the DD domain has close resemblance with the physical geometric parameters of the environment, such as the distance and relative velocity of the reflectors.

Since the Fourier transform is reversible, the transition between domains can be carried out in several ways. For example, there are two routes from the TD to DD domain (in Figure 2.1 they are indicated by red and green arrows). These two paths will be discussed at the end of this subsection in more detail. For now let us continue the introduction of the general idea of the DD domain. The shortest way from TD to DD lies through the Zak transform.

Let us denote the DD grid on the transmitter side as $\mathbf{X_{DD}} \in \mathbb{C}^{\mathbf{M}\times\mathbf{N}}$, where M is a number of carriers in the delay direction and N is a number of carriers in the Doppler directions. The same dimensions have

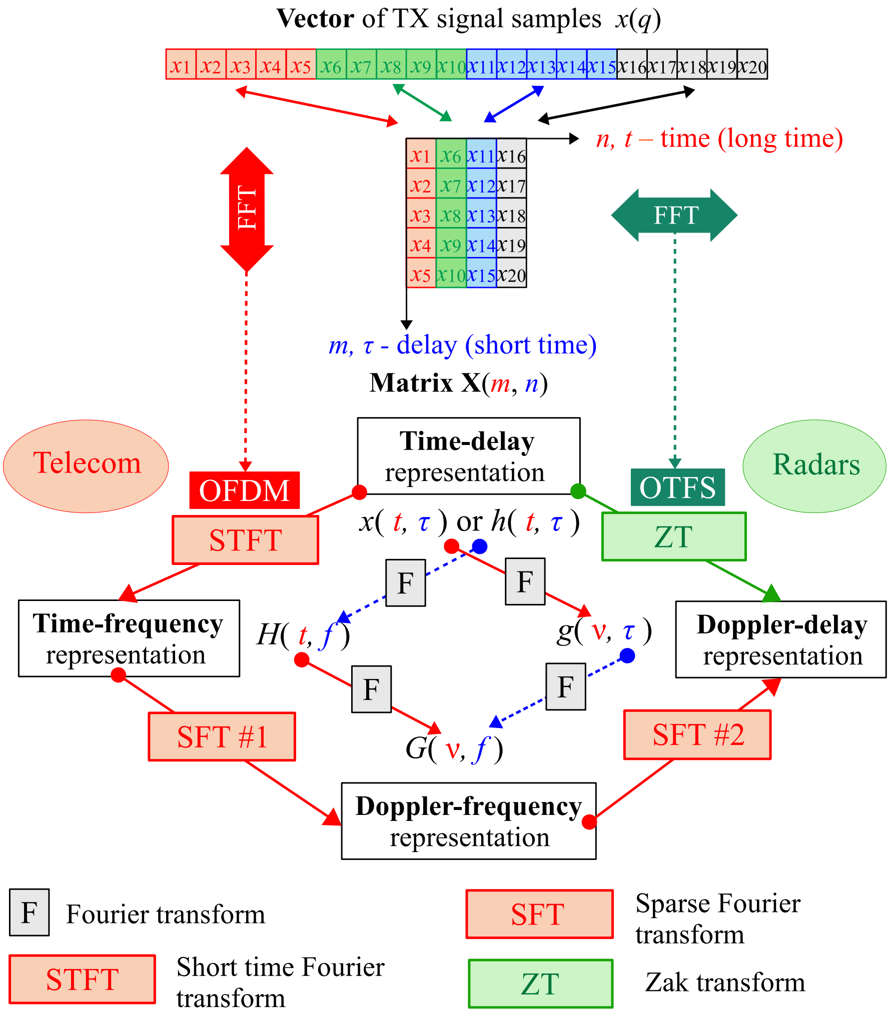

Figure 2.1: The representation of the signal and channel state information in different domains. Note that switching between TD and DD domain could be achieved in two different routes: following red arrows, and directly from TD to DD (green arrow).

matrices in other domains have different physical meaning, for example, TF domain $\mathbf{X_{TF}} \in \mathbb{C}^{\mathbf{M}\times\mathbf{N}}$, M is a number of subcarriers, N is the number of OFDM symbols. Given a continuous-time signal $x(t)$, we define the Zak transform with step $T = \tau_p$ as the bivariate function over the DD (τ, ν) plane [36]:

$$x_{DD}(\tau, \nu) = \mathcal{Z}\{x(t)\}(\tau, \nu) = \sqrt{\tau_p} \sum_{n=-\infty}^{+\infty} x(\tau + nT) e^{-j2\pi nT\nu} \tag{2.3}$$

The inverse Zak transform:

$$x(t) = \mathcal{Z}^{-1}\{x_{DD}(\tau, \nu)\} = \sqrt{\tau_p} \sum_{n=-\infty}^{+\infty} \int_0^{\nu_p} x_{DD}(\tau + n\tau_p, \nu) e^{j2\pi n\tau_p\nu} d\nu \tag{2.4}$$

Although the summation in the Zak transform formulas (2.3) and (2.4) is taken over all integers, in practice we do not deal with infinite signals. Rather, we consider limited dimensions in both directions of the DD domain:

$$D_0 = (\tau, \nu),\ 0 \leq \tau < \tau_0,\ 0 \leq \nu < \nu_0. \tag{2.5}$$

The matrix D_0 repeats along the delay and Doppler axis with periods τ_0 (delay period) and $\nu_0 = 1/\tau_0$ (Doppler period). The period D_0 form (2.5) is called the fundamental period. In case of OTFS modulation, the data is carried by sub-carriers that are located in the fundamental period of DD domain. In the context of OTFS, the Zak transform serves a role analogous to that of the Fourier transform in OFDM [36].

The pulse in the DD domain at (τ_i, ν_i) is given by:

$$x_{DD}(\tau, \nu; \tau_i, \nu_i) = \sum_{n\in\mathbb{Z}} \sum_{m\in\mathbb{Z}} e^{j2\pi n \nu_i \tau_0} \delta(\tau - \tau_i - n\tau_0 p)\delta(\nu - \nu_i - m\nu_0). \tag{2.6}$$

The DD pulse from (2.6) in time domain [44]:

$$x(t) = \sqrt{\tau_0} e^{j2\pi\nu_i(t-\tau_i)} \left[\sum_{n\in\mathbb{Z}} \delta(t - \tau_i - n\tau_0) \right]. \tag{2.7}$$

It can be seen that formula (2.7) describes the train of impulses in the time-domain that are modulated by the complex exponent $e^{j2\pi\nu_i(t-\tau_i)}$. The impulse period inside the train is equal to τ_0 seconds. This pulse modulated with a tone is appropriately called a *pulsone*. A closer examination of equations (2.6) and (2.7) reveals that all pulses on the DD grid x_{DD} are orthogonal either in time (simply shifted relative to each other) or in frequency. The OTFS waveform is biorthogonal: it is orthogonal in both directions as proofed in [45]. Hence, it can be concluded that the OTFS signal in the time domain can be represented as a sum of orthogonal pulses.

From the above discussion, one very important feature of the DD grid can be noticed. The DD grid is quasi-periodic [36, 44], i.e.

$$x_{DD}(\tau + n\tau_0, \nu + m\nu_0) = e^{j2\pi n\nu\tau_0} x_{DD}(\tau, \nu) \tag{2.8}$$

The visualization of this quasi-periodic property is shown in Figure 2.2. More properties of the DD grid that come from the Zak transform can be found in the Appendix A.

It should be noted that (2.8) is also valid for delays and Doppler shifts that are not integer multiples of the fundamental period. This property represents a fundamental distinction from waveforms such as OFDM and, when combined with the linearity of the Zak transform, provides one of the key advantages of OTFS. In OTFS, signal replicas shifted in both Doppler and delay directions are linearly superimposed in DD domain (with multiplication by a complex exponential). Consequently, neither Doppler shifts nor delays introduce nonlinear distortions into the signal.

Similarly with OFDM, for the modulated signals in the DD domain, we can define a function that corresponds to the convolution in the time domain. In case of the DD domain it is *twisted convolution*. In other words, the DD representation ($y_{DD}(\tau, \nu)$) of the received time domain signal $y(t)$ is given by twisted convolution of the channel function $h(t, \tau)$ and the DD representation $x_{DD}(\tau, \nu)$ of the transmitted time domain signal $x(t)$. We will denote the twisted convolution with the symbol $\star$:

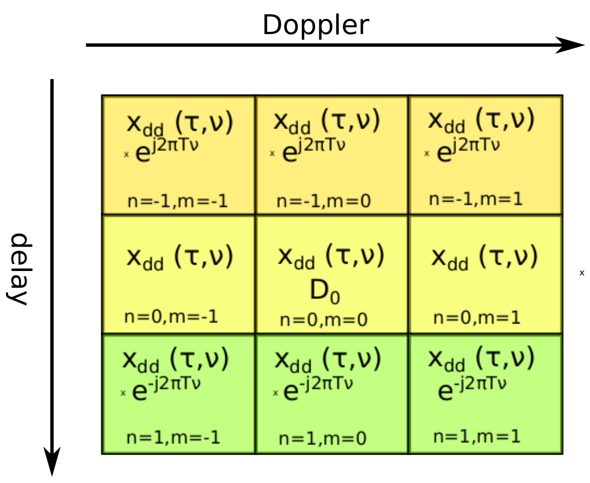

Figure 2.2: The quasi-periodic property of the DD grid. D_0 is the fundamental period.

$$y_{DD}(\tau,\nu) = h(t,\tau) \star x(t) = \int_0^{\tau_p} \int_0^{\nu_p} e^{j2\pi(\tau-\theta)} \mathcal{Z}\{h(t,\tau)\}(\theta,u) x_{DD}(\tau-\theta,\nu-u)\, d\theta\, du. \tag{2.9}$$

As mentioned above, there are two ways to switch between TD and DD domains. For simplicity, here we will consider only the fundamental period of the DD matrix and the discrete representation of $x(t)$.

In conclusion, from Figure 2.1 the switching options between the transmitted TD $\mathbf{X}(m,n)$ and DD $\mathbf{X_{DD}}(m,n)$ are following (the transformation from DD to TD could be done in a similar way).

To emphasize the different physical meanings of the indices in various domains, in Equations (2.10)-(2.13) we will use dedicated discrete indexes: $t \leftrightarrow b'$ (time), $\tau \leftrightarrow a$ (delay), $v \leftrightarrow b$ (Doppler) and $f \leftrightarrow a'$ (frequency), also we added here an explicit index TD for $\mathbf{X}$

1. directly via IZT, i.e. IDFT (if no windowing is used) of $\mathbf{X_{DD}}(a,b)$ rows:

$$\text{DD} \to \text{TD},\ \text{IDFT[rows]}: \qquad \mathbf{X_{TD}}(a,b') = \frac{1}{\sqrt{N}} \sum_{b=0}^{N-1} \mathbf{X_{DD}}(a,b) e^{j\frac{2\pi}{N}bb'}; \tag{2.10}$$

2. around via 2D inverse SFT of $\mathbf{X_{DD}}(a,b)$ followed by IDFTs of columns of obtained $\mathbf{X_{TF}}(a',b')$:

$$\text{DD} \to \text{DF},\ \text{DFT[cols]}: \qquad \mathbf{X_{DF}}(a',b) = \frac{1}{\sqrt{M}} \sum_{a=0}^{M-1} \mathbf{X_{DD}}(a,b) e^{-j\frac{2\pi}{M}aa'}, \tag{2.11}$$

$$\text{DF} \to \text{TF},\ \text{IDFT[rows]}: \qquad \mathbf{X_{TF}}(a',b') = \frac{1}{\sqrt{N}} \sum_{b=0}^{N-1} \mathbf{X_{DF}}(a',b) e^{j\frac{2\pi}{N}bb'}, \tag{2.12}$$

$$\text{TF} \to \text{TD},\ \text{IDFT[cols]}: \qquad \mathbf{X_{TD}}(a,b') = \frac{1}{\sqrt{M}} \sum_{a=0}^{M-1} \mathbf{X_{TF}}(a',b') e^{j\frac{2\pi}{M}aa'}. \tag{2.13}$$

It can be seen that the last step (2.13) in the second method is equivalent to the generation of the OFDM waveform $\mathbf{X_{TD}}(a,b')$ from the given $\mathbf{X_{TF}}(a',b')$ IQ values. Therefore, OTFS modulation can be interpreted as OFDM modulation with specific precoding. Consequently, the existing OFDM hardware can be used in joint OFDM & OTFS-based ISAC systems.

The sequential application of Equations (2.11)–(2.12) to the signal is referred to as the inverse Symplectic Finite Fourier Transform (ISFFT). This operation maps the signal representation from the DD domain into the TF domain. The forward transform (SFFT) can be obtained by conjugating the exponential terms, enabling the mapping in the opposite direction [36].

In this work, we do not employ the pulse-shaping (or windowing) function for OTFS sub-carriers to maximize the density of the sub-carriers in the DD grid. Now, as we defined the most important properties of the modulation in the DD domain, we will focus on basic characteristics of the DD grid itself.

2.1.2 Delay-Doppler Grid

Assuming that the sampling rate of the signal is f_s, we can calculate the basic parameters of the signal, the OTFS resolution parameters as well as the maximum delay and the maximum Doppler of the DD-grid. The length of the OTFS frame is $T = M \times N/f_s$ and the signal bandwidth is $B = f_s$. The basic characteristics of the DD grid are given in Table 2.1, while in the Figure 2.3 the connection between the parameters of the TF and DD domains is shown. We assume that the OTFS signal is critically sampled, this means $\frac{B}{f_s} = 1$.

Table 2.1: Basic characteristics of the DD grid of the OTFS signal.

Parameter name	**Value**	**Comment**
T	$M \times N/f_s$	Length of the frame, s
B	$1/f_s$	Bandwidth, Hz
Δt	$1/f_s$	Delay resolution, s
Δf	$\pm f_s/2M$	Doppler offset resolution, Hz
τ_{max}	M/f_s	Maximum delay, s
$f_{d_{max}}$	$\pm f_s/2MN$	Maximum Doppler offset, Hz

In OTFS, the grid is usually divided into two parts: a data zone and a zone containing signals used for channel estimation (the so-called pilots). Depending on the pilot configuration, several variants of OTFS can be distinguished (we describe the most significant among them):

- ZP-OTFS - this is the oldest and the most common pilot configuration used for channel estimation in OTFS [24];
- ZP-BOX-OTFS - it was designed to address some of the drawbacks of ZP-OTFS (low number of active carriers in OTFS pilot zone) [25, 24];
- RP-OTFS - proposed by us [27, 31], this OTFS-like waveform will be thoroughly investigated in the next chapter;
- Zadoff-Chu OTFS (ZC-OTFS) - an attempt to use a ZC sequence as a pilot [46], practically it is subset of RP-OTFS.

The visualization of these and other possible (not all) configurations of the DD grid in OTFS is shown in Figure 2.4.

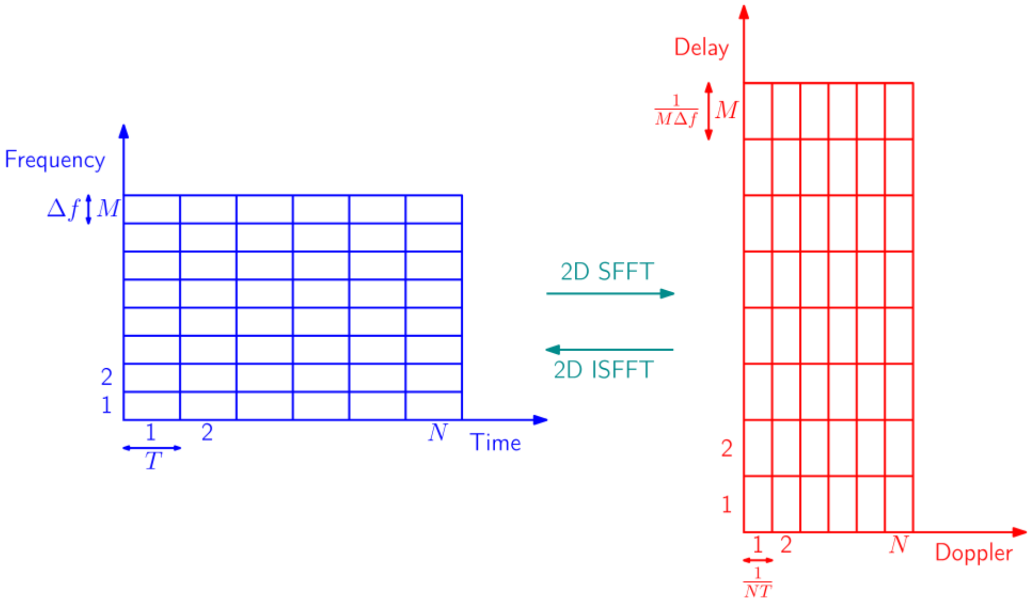

Figure 2.3: The parameters correspondence in TF and DD domains. The domain transformation between TF to DD done by (I)SFFT, the sequential application Equations (2.11)–(2.12) to the signal.

The physical sense of the parameters M and N (and their corresponding indices m, n) depends on the domain in which the processing is performed. In this work, three domains for analysis and processing are used: TD, TF, and DD. The physical meaning of the parameters is explained in Table 2.2 (also see Figure 2.1).

Table 2.2: The physical sense of the parameters M and N in different domains

Domain	M **meaning**	N **meaning**
TD	Decimation rate of a time domain signal $x(q)$	Number of decimated signal samples
TF	Number of OFDM sub-carriers	Number of OFDM symbols
DD	Number of delay taps	Number of Doppler taps

2.2 Doubly-Spread Channel

2.2.1 General Considerations

Due to the different lengths of propagation paths, the receiver observes a temporally smeared version of the transmitted signal. It is shown in [1] that such channels, termed time-dispersive, are frequency-selective in the sense that different frequencies are attenuated differently. In general, the multipath propagation is not the only source of time dispersion, other sources could be: imperfect timing recovery, sampling jitter, etc.

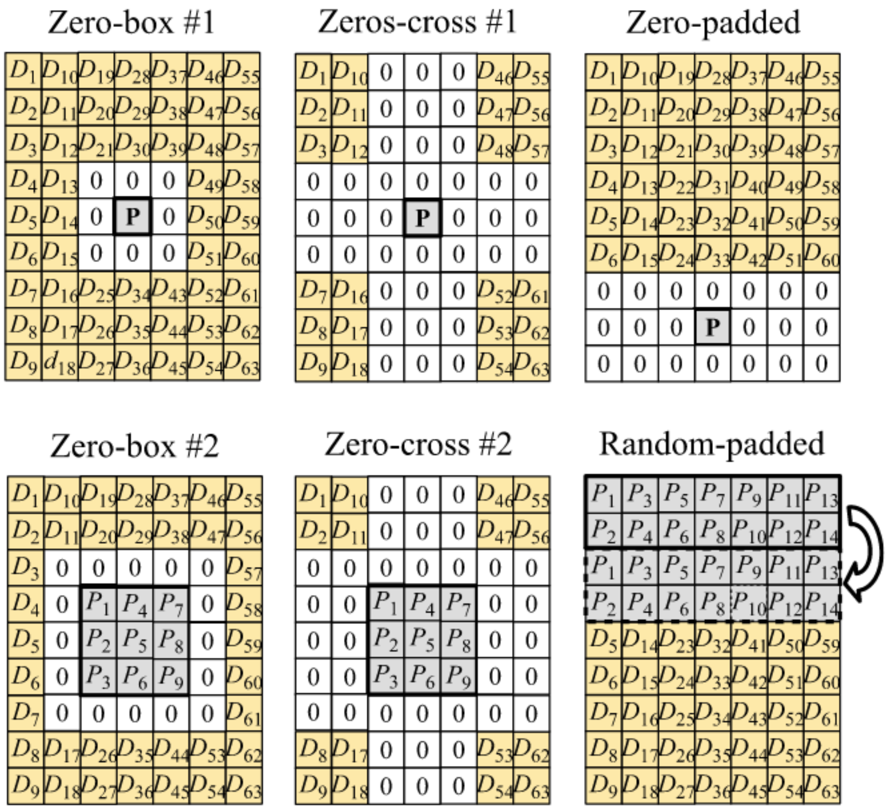

Figure 2.4: Different OTFS pilot configurations. The cells denoted with symbol D are used for data transmission, those denoted with symbol P are used for pilot signal transmission, while the cells marked with 0 are inactive and do not participate in transmission.

Starting from here and until the end of this thesis, we assume that the signal meets the narrowband criterion (the bandwidth of the signal B is much smaller than the carrier frequency f_c, $B/f_c << 1$).

In many wireless systems, the transmitter, receiver, or scatters are moving. In such situations, the signal experiences the Doppler effect. For the narrowband signal, the Doppler effect essentially results in a frequency shift proportional to velocity v and carrier frequency f_c. It is important to note here that for the Doppler frequency shift only the projection of the velocity vector on the propagation path should be considered. For example, the transmitter moving around the receiver and the receiver in the center of the transmitter's trajectory circle will not experience any Doppler shift, despite the fact that the relative position of the transmitter and the receiver will change all the time. In general case of multipath propagation and moving receiver, transmitter, or scatters, the received signal experiences superposition of different Doppler frequency shifts, and such a channel is called frequency-dispersive (or time-selective). Channels that have both time-dispersive and frequency-dispersive components are called doubly dispersive channels.

Although multipath propagation has been viewed as a transmission impairment, in modern communication systems it is considered a degree of freedom and widely used in MIMO systems (it is known as channel diversity). In the context of OTFS, it is also appropriate to mention another form of diversity, Doppler diversity, which can potentially be exploited in OTFS MIMO as well. More information can be found in [44].

One of the key parameters at the receiver end is the received power of the signal. Usually, it is modeled as the sum of three components:

- the pass loss - this component describes the distance-dependent power decay [47];
- the large-scale fading (slow fading) - this component describes shadowing of the huge objects and absorption loss (for example, fog);
- the small-scale fading (fast fading) - this component describes different propagation path in the multipath environment; the magnitude coefficient of this component is usually described by Rayleigh (or Rice) distribution.

In this thesis, we will consider only the fast fading component, as it has the greatest impact on the SNR at the receiver (and other related characteristic, for example, SINR). We consider the scenario in which pass loss and slow fading could be compensated by the power control loop on the transmitter side.

In the thesis (at least in its communication part) we will treat the channel as a dual spread wide-sense stationary uncorrelated scattering (WSSUS) channel [1].

Strictly speaking, there are multiple ways to characterize the channel. The dual spread channel function could be represented in TF, TD, time-scale (for wideband signals, Doppler "scales" the signal in the frequency domain), or DD domain. In the Introduction, it was noted that the OTFS waveform uses a DD domain to modulate the carriers, so we will mainly focus on the DD channel representation. Although we will also discuss the TF representation as it is useful for the OFDM waveform (as a baseline) and the Random-Padded OTFS (RP-OTFS), which will be introduced later. Let us denote for the p-th propagation path: the complex gain as h_p, the delay as τ_p, and the Doppler offset as ν_p. For P propagation paths, the spreading function is defined as

$$G(\tau, \nu) = \sum_{p=1}^{P} h_p \delta(\tau - \tau_p)\delta(\nu - \nu_p). \tag{2.14}$$

The channel transfer function in the TF domain is equal:

$$H(t, f) = \int_{-\infty}^{+\infty} \int_{-\infty}^{+\infty} G(\tau, \nu) e^{j2\pi(t\nu - f\tau)} d\tau d\nu. \tag{2.15}$$

The dual-selective channel could also be described in the TD domain as

$$h(t, \tau) = \int_{-\infty}^{+\infty} G(\tau, \nu) e^{j2\pi\nu(t-\tau)} d\nu = \sum_{p=1}^{P} h_p e^{j2\pi\nu_p(t-\tau)} \delta(\tau - \tau_p). \tag{2.16}$$

Regardless of the channel representation domain, the relationship between $x(t)$ and $y(t)$ can be expressed using equations (2.14), (2.15), or (2.16):

$$y(t) = \int_{\tau} h(t, \tau) x(t - \tau) d\tau = \int_{f} H(t, f) X(f) e^{j2\pi f t} df = \int_{\nu} \int_{\tau} G(\tau, \nu) x(t - \tau) e^{j2\pi\nu t} d\tau d\nu, \tag{2.17}$$

where $X(f)$ is the result of the Fourier transform of $x(t)$, $X(f) = \mathscr{F}\{x(t)\}$.

To obtain convenient expressions for the discrete-time case that is connected to the OTFS parameters, we perform several substitutions. For simplicity, we will normalize the delay and Doppler to the resolution of the grid elements in the following way: $\ell_p = \tau_p \times \frac{T}{MN}$ is a normalized delay, and $\kappa_p = \nu_p \times NT$, T is the length of the OTFS frame. Here, it is important to note that ℓ_p and κ_p are not necessarily integers. We will denote the set of delays by $\mathcal{L} = \{\ell_p\}$, and $K_\ell = \{\kappa_p \mid \ell = \ell_p\}$. In this work, we will assume that the maximum delay does not exceed the length of the grid in the delay direction, $\frac{M}{f_s}$, and that the Nyquist criterion in the Doppler direction is also met ($-N/2 \leq \kappa_p \leq N/2$).

Using the new notation and sampling $x(t)$ at time $t = qT/M$, where $q = 0, ..., MN - 1$ the equation (2.16) could be rewritten as follows [16, 4]:

$$h[l,q] = h(lT/M, qT/M) = \sum_{\ell \in \mathcal{L}} \left(\sum_{\kappa \in K_\ell} \nu_\ell(\kappa) e^{\frac{j2\pi\kappa(q-l)}{MN}} \right) \operatorname{sinc}(l - \ell), \tag{2.18}$$

where

$$\nu_\ell(\kappa) = \begin{cases} h_p, \text{ if } \ell = \ell_p \text{ and } \kappa = \kappa_p, \\ 0, \text{ otherwise,} \end{cases} \tag{2.19}$$

and $\operatorname{sinc}(x) = \frac{sin(\pi x)}{(\pi x)}$. Finally, the received signal in the discrete-time domain is:

$$y[q] = y(qT/M) = \sum_{l=0}^{M-1} h[l,q]x[q-l]. \tag{2.20}$$

2.2.2 Channel Coherence Intervals

The value of the spreading function from (2.14) at a given point on the DD grid (τ, ν) characterizes the attenuation and scatter reflectivity associated with the path with delay τ and Doppler ν. The example of the spreading function is given in Figure 2.5.

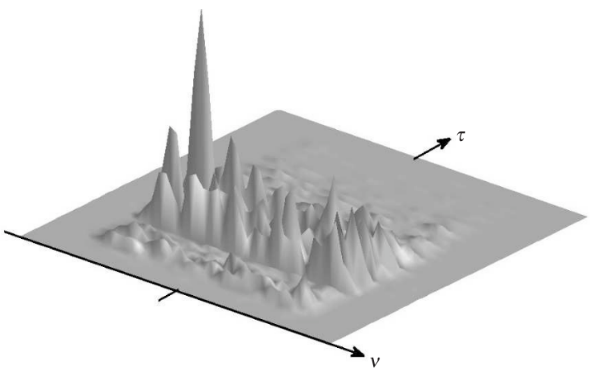

Figure 2.5: The example of dual spreading channel spread function $S_h(\tau, \nu)$ in DD domain [1].

For further analysis, we will need the stochastic description of the dual spread channel in the DD domain. In the case of the WSSUS channel

$$\mathrm{E}\{G(\tau,\nu)G^*(\tau',\nu')\} = C_H(\tau,\nu)\delta(\tau - \tau')\delta(\nu - \nu'). \tag{2.21}$$

The symbol G^* denotes the complex conjugate of G. The scattering function C_H characterizes the average strength of scatters with delay τ and Doppler frequency ν.

In the case of the WSSUS channel, the path loss is equal to the volume of the scattering function, or, equivalently, the maximum amplitude of the TF correlation function. That is, we have $P_L = -10log_{10}(\rho_H^2)$ with

$$\rho_H^2 = \int_{-\infty}^{+\infty}\int_{-\infty}^{+\infty} C_H(\tau,\nu)d\tau d\nu = \mathrm{E}\{|H(t,f)|^2\} = R_H(0,0). \tag{2.22}$$

Note that $\mathrm{E}\{|H(t,f)|^2\}$ does not depend on t and f due to the stationarity of the WSSUS channels.

Other useful parameters are mean delay and mean Doppler:

$$\bar{\tau} = \frac{1}{\rho_H^2}\int_{-\infty}^{+\infty}\int_{-\infty}^{+\infty} \tau C_H(\tau,\nu)d\tau d\nu, \tag{2.23}$$

$$\bar{\nu} = \frac{1}{\rho_H^2}\int_{-\infty}^{+\infty}\int_{-\infty}^{+\infty} \nu C_H(\tau,\nu)d\tau d\nu. \tag{2.24}$$

The mean delay $\bar{\tau}$ and the mean Doppler $\bar{\nu}$ describe the overall location of the scattering function $C_H(\tau,\nu)$ in the DD plane. The extension of $C_H(\tau,\nu)$ around $(\bar{\tau},\bar{\nu})$ can be measured by the delay spread and the Doppler spread, which are defined as the root mean square (RMS) widths of the delay power profile and Doppler power profile, respectively:

$$\sigma_\tau = \frac{1}{\rho_H^2}\sqrt{\int_{-\infty}^{+\infty}\int_{-\infty}^{+\infty} (\tau-\bar{\tau})^2 C_H(\tau,\nu)d\tau d\nu}, \tag{2.25}$$

$$\sigma_\nu = \frac{1}{\rho_H^2}\sqrt{\int_{-\infty}^{+\infty}\int_{-\infty}^{+\infty} (\nu-\bar{\nu})^2 C_H(\tau,\nu)d\tau d\nu}. \tag{2.26}$$

The reciprocals of the delay spread (σ_τ) and the Doppler spread (σ_ν) give us the fundamental quantities of the channel, the coherence time T_c and the coherence frequency F_c:

$$T_c = \frac{1}{\sigma_\nu}, \tag{2.27}$$

$$F_c = \frac{1}{\sigma_\tau}. \tag{2.28}$$

These two quantities provide an estimate of the time period (for the coherence time T_c) and the bandwidth (in case of the coherence frequency F_c) during which we can consider our channel to be approximately constant (or at least strongly correlated).

It is shown in [1] that in the case of Jake's Doppler spectrum [48], the RMS delay and Doppler spread $\sigma_\tau = \bar{\tau}$ and $\sigma_\nu = \frac{f_{dmax}}{\sqrt{2}}$. This gives us:

$$T_c = \frac{\sqrt{2}}{f_{dmax}},\ F_c = \frac{1}{\bar{\tau}}. \tag{2.29}$$

Using the formula below, the maximum Doppler frequency f_{dmax} could easily be estimated:

$$f_{dmax} = f_c\left[1 - \frac{v}{c_0}cos(\phi)\right], \tag{2.30}$$

where c_0 is the speed of light, v - the mutual velocity of the transmitter and receiver, ϕ is an angle between the velocity vector v and the direction of the wave at the receiver [48].

In the concluding part of this subsection, it is appropriate to mention OFDM. In OFDM, we assume that the channel is constant during the whole OFDM symbol, but also that our sub-carriers (at least between two pilots) are not too far apart from each other. Here, the values that we recently obtained become crucial. On the one hand, the coherence time limits the length of our symbol, while on the other hand, the coherence bandwidth sets the spacing between subcarriers. In addition to this, considering that the bandwidth occupied by the signal is inversely proportional to its duration, makes the situation even more contradictory.

To better understand this, let us consider the following example. Let the number of OFDM subcarriers be constant. To operate in channels with strong Doppler (short coherence time), we want to shorten the duration of the OFDM symbol, while keeping the number of subcarriers constant. This means increasing the spacing between them. However, on the other hand, increasing the sub-carrier spacing can lead to exceeding the coherence interval in the frequency domain. The 5G standard introduced OFDM options with different subcarrier spacing (so-called numerologies), an attempt to find a compromise between coherence time and coherence bandwidth. It is worth noting that they all have a short cyclic prefix, not only to reduce transmission overhead, but also because the large subcarrier spacing means a small time $\bar{\tau}$ (see (2.29)).

This leads us to the main challenge of OFDM, its inability to operate effectively in channels with strong Doppler spread and significant delay spread. We are omitting the fact that increasing sub-carrier spacing also increases the occupied bandwidth, which is a significant limiting factor, as we cannot increase bandwidth indefinitely. Taking this considerations in account makes OTFS waveform more attractable.

2.3 OTFS Receivers

In previous subsections, we discussed the OTFS modulation and the influence of the fading channel in order to understand the signal processing that is needed in an OTFS receiver.

Regardless of the channel estimation method, equalization (or, as referred to in some literature, signal detection) is one of the most critical steps. Here, we examine the specific features of the OTFS receiver design. Signal detection approaches for OTFS can be divided into three categories: linear, maximum a posteriori probability (MAP), and cross-domain.

Linear Detection

Examples of such detection methods are the well-known zero-forcing (ZF) and the linear minimum mean squared error (LMMSE) approach. These receivers use a linear transformation to estimate the transmitted signal. In the context of OTFS, certain properties of the channel matrix allow for the optimization of these methods, significantly reducing computational complexity.

Compared to the ZF detector, the LMMSE detector offers improved robustness against noise amplification, especially in scenarios with low signal-to-noise ratios. By incorporating statistical knowledge of noise and signal power, LMMSE achieves a better trade-off between interference suppression and noise enhancement.

The LMMSE detector can be defined in both domains, TD and DD [36]:

$$\hat{x} = R_{hh^{inst}} R^{-1}_{h^{inst}h^{inst}} h^{inst} y, \tag{2.31}$$

where h_{inst} is the instantaneous estimate of the channel. Here, we intentionally omit the indices of the variables to emphasize that this approach is applicable not only to specific domains such as TD or DD. $R_{hh^{inst}}$ is a covariance matrix between the channel coefficients and their instantaneous estimates, $R_{h^{inst}h^{inst}}$ is the autocovariance matrix of the instantaneous estimates. Given that we have additive white Gaussian noise (AWGN) with variance σ_n^2 channel, $R_{hh^{inst}} = R_{hh}$ and $R_{h^{inst}h^{inst}} = (R_{hh} + (xx^T)^{-1}\sigma_n^2 I)$. The (xx^T) is the normalization factor, if the signal power is normalized and equals to 1, then it can be skipped. The channel correlation function is unknown at the receiver $R_{hh} = R\{h^* h^T\}^*$. In fact, samples of R_{hh} are simply obtained by the Fourier transform of the channel intensity profile. It is usual to model the channel intensity profile as a decreasing exponential over $\tau \in [0, \tau_{max}]$. Thus, the samples of $r_{u,v}$ (u-th row and v-th column of the R matrix) can be expressed as

$$r_{u,v} = \mathscr{F}_\tau(Ce^{\tau/\tau_{max}}) = PC\frac{1 - e^{2\pi j \frac{u-v}{L}\tau_{max}}}{1 + 2\pi j \frac{u-v}{L}\tau_{max}}, \tag{2.32}$$

where C is normalization factor, P - number of propagation paths.

As mentioned earlier, formula (2.31) can be applied in multiple domains, in the sense that its idea remains unchanged while only the variables in the equation vary. This formula, in the case of a discrete two-dimensional DD grid, will be demonstrated later in Section 3.2.2. The original LMMSE algorithm has complexity $\mathcal{O}(N^3M^3)$ [49]. This makes its usage computationally complex and slow, even for relatively small grid sizes.

Several studies have been conducted on optimization of the LMMSE complexity in the context of OTFS. One of the key observations when building an LMMSE receiver for OTFS is that the spreading function $G(\tau, \nu)$ is generally close to zero almost everywhere, except for certain regions where the reflectors are concentrated. As a result, the channel matrix in DD domain $\mathbf{G}$ is sparse, allowing optimization of the computational complexity of the LMMSE detector. Another way to optimize is to use the block circular nature of the OTFS channel matrix. More information on OTFS LMMSE receivers can be found in [49, 37, 50, 51].

MAP Detection

MP detector approximates the MAP in the following way:

$$\hat{\mathbf{X}}_{\mathbf{DD}} = \arg\max_{x \in \mathbb{A}^{M\times N}} Pr(\mathbf{X}_{\mathbf{DD}} | \mathbf{Y}_{\mathbf{DD}}, \mathbf{G}), \tag{2.33}$$

where $\mathbb{A}^{M\times N}$ is a set of constellation symbols Several algorithms of this class have been described in the OTFS literature.

- **Message Passing (MP) detector.** It has linear complexity and quite good performance. This algorithm involves the computation of approximate a posteriori probabilities of the modulation symbols by passing messages on a sparsely connected graph (Figure 2.6). The algorithm operates iteratively and the graph elements update the probability estimates sequentially. The graph consists of two types of nodes: check nodes (yy) and variable nodes (xx) [52]. A simplified version of this algorithm (without taking into account probabilities) is described here [4].

- **Variational Bayes-Based Detector.** This algorithm approximates the optimal MAP detection by approximating the joint a posteriori distribution by the product of local marginals [53].

- **Hybrid MAP and Parallel Inference Cancellation (PIC) Detection.** The algorithm is very similar to MP, but processes a subset of it with high and low gain in the channel separately [54]. This algorithm is inspired by [55].

- **Markov Chain Monte Carlo (MCMC) Sampling Based Detection.** MCMC techniques are computational techniques commonly used for calculating complex integrals by expressing the integral as an expectation of some probability distribution and then estimating this expectation from the generated samples of that distribution. In this technique, a new sample value is generated randomly from the most recent sample. The transition probabilities between samples are only a function of the previous sample, and hence the name MCMC [56].

Cross-Domain Detection

The key idea of this algorithm is to combine information from two domains: TD and DD. It is beneficial when the Doppler resolution of the DD is not very high and huge side-lobes from reflections (fractional Doppler) are expected. The unitary transformation between TD and DD allows the detection/estimation errors in one domain to be principally orthogonal to errors in the other domain. This can suppress the correlation between the input and output errors for each domain detection/estimation and improve the error performance. In TD and DD, some basic detection algorithm can be used, for example, LMMSE [57].

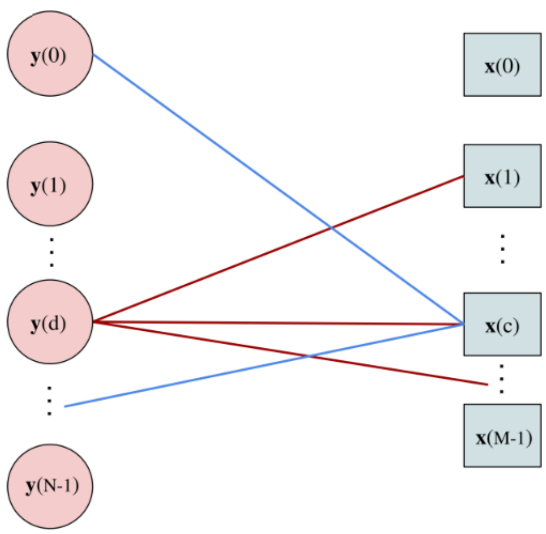

Figure 2.6: MP detector graph.

2.4 Integrated Sensing and Communication

As noted previously, ISAC systems are essentially a hybrid of two subsystems: radar and communication. Since the communication subsystem was discussed in the preceding subsections, we will focus here on the radar module in the ISAC context. In case of ISAC systems it implies simultaneous target detection and data transmission. Typically, such systems are considered in the context of bistatic radar architectures, where the transmitter and receiver are located at different positions. At the beginning of this section, we will discuss the basic radar principles that are common for all types of radar. After that, we examine the bistatic radar geometry and some other aspects of signal processing.

General Considerations

The same as in classical radar systems, one of the key characteristics that determines both the accuracy of estimation and the probability of target detection is the SNR. The SNR on the detector input (γ_{det}) consists of two components:

$$\gamma_{det} = \gamma_{in} + G_P, \tag{2.34}$$

where G_p is a processing gain. The γ_{input} at the input of the receiver is defined as:

$$\gamma_{in} = \frac{P_{rx}}{\underbrace{k_B \cdot \theta \cdot N_F}_{\text{Noise power density}} \cdot B}, \tag{2.35}$$

where P_{rx} is the power of the signal at the receiver input, $k_b \approx 1.38 \times 10^{-23}\ J \cdot K^{-1}$ is the Boltzmann constant, θ - the temperature of the receiver, N_F - the noise figure of the analog part of the receiver, B_W - the bandwidth of the receiver. The power at the receiver input is defined by [22]:

$$P_{rx} = \frac{P_{tx} G_{tx}}{4\pi R_T^2} \times \frac{\sigma_{RCS}}{4\pi R_R^2} \times G_{rx}, \tag{2.36}$$

where G_{tx} and G_{rx} - antenna gain in the receiver and transmitter, R_T and R_R - distance to the target from the transmitter and receiver, σ_{RCS} - radar cross section (RCS) of the target.

Filtering a received signal $y(t)$ with its matching filter corresponds to computing the continuous-time autocorrelation function of $x(t)$:

$$R_{xy}(t) = \int_{-\infty}^{+\infty} x^*(\tau) y(t-\tau) d\tau. \tag{2.37}$$

Then, for a discrete-time and time-limited system, (2.37) can be written as follows [2]:

$$R_{xy}[n] = \sum_{m=0}^{MN-1} x^*[m] y[n-m], -\infty < n < +\infty. \tag{2.38}$$

In the following subsection, we will describe the ways in which processing can be performed specifically for the ISAC radar.

In the context of OTFS, it can be assumed that the most convenient observation time for the signal is the duration of one or multiple OTFS frames. Intuitively, it makes sense that an optimal detector would accumulate the energy received from all elements of $y[q]$ in one bin of the DD grid. The maximum processing gain G_{Pmax} is the following [58]:

$$G_{Pmax} = 10log_{10}(MN). \tag{2.39}$$

Increasing the integration time can lead to an improved SNR and, consequently, to enhance the probability of target detection. But the integration time is limited mainly by two factors. Firstly, by the time duration in which the target remains within a resolution cell: a longer integration time reduces the spatial scanning rate, which in turn may hinder target tracking. Secondly, by sidelobes of the signal's own autocorrelation function: even in the case of stationary targets, it is important to remember that the autocorrelation function of any signal has a certain level of sidelobes, which depends only on the signal waveform. As processing gain continues to increase, there comes a point at which the sidelobes begin to dominate over the noise, and further increasing integration time no longer yields the desired improvements.

The next step of radar processing is to determine whether a target echo is present within a given resolution cell. The decision is made in the detector. The objective of the detector is to identify peaks on the DD (in radar literature often called range-Doppler (RD)) grid that are caused by actual targets and to distinguish them from spurious fluctuations. The main sources of such inferences are the peaks caused by the AWGN channel and the peaks resulting from the sidelobes of the signal correlation function. Based on the measurements and some threshold, the detector chooses one of the two hypotheses: 1) H_0 - the measurements contain energy only from interfering sources, or 2) H_1 - the measurements contain energy from interfering sources and the target.

After the detector makes a decision, there are three possible outcomes [2]:

- **correct decision** - the detector correctly declares the presence or absence of a target;
- **false alarm** - the detector declares the presence of a target while in reality a target's return in not present in the measured data;
- **missed detection** - the detector declares the absence of a target when in truth the measurement contains a target return.

There are numerous algorithms on how to select the optimal decision threshold η for the detector. The **constant false alarm ratio (CFAR)** maintains a given probability of false alarm in the presence of heterogeneous or changing interference. In the context of an OTFS frame, the false alarm ratio (R_{FA}) is equal [58]:

$$R_{FA} = MN \cdot P_{FA} \tag{2.40}$$

where P_{FA} is the probability of false alarm in one resolution cell. A large number of false alarms may overload the signal/data processor, which would result in dropped detections or tracks and a reduction in the timeline and processing capacity available for other radar processing parts. This is one of the main reasons why CFAR is a popular algorithm.

A **square-law detector** is commonly applied in radar systems and makes a decision based on $|y|^2$. The interference with the Rayleigh distribution is distributed exponentially [2]:

$$p_{sl}(|y|^2) = \frac{1}{\sigma^2} e^{\frac{-|y|^2}{\sigma^2}} \tag{2.41}$$

in the case of the square-law detector. By integrating (2.41) from η to $+\infty$ (in case of absence of the target, this will give the probability of false alarm), then solving for η gives us the threshold for the desired $P_{FA,cell}$ in one resolution cell:

$$\eta = -\ln(P_{FA,cell})\sigma^2. \tag{2.42}$$

To maintain the desired level of false alarms during the OTFS frame (2.42) should be recomputed to take into account all the resolution cells in the DD grid [58]:

$$\eta = \ln(1 - (1 - P_{FA})^{1/MN})\sigma^2. \tag{2.43}$$

In the most simple case, η could be computed based on statistics collected simply by averaging the DD grid cells in the neighborhood of the cell under test (CUT) with some guard interval – see Figure 2.7. The guard interval is needed to ensure that there is no influence of the target's echo on the estimation of η. In this case, the following assertions should be met: the interferences are i.i.d. and target returns are present only in the CUT cell (such environments are called homogeneous).

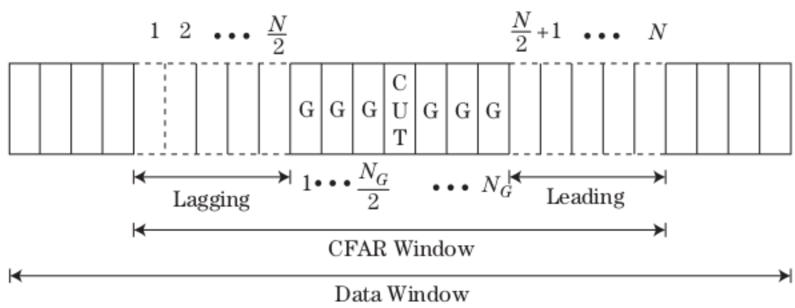

Figure 2.7: In the CFAR detector, necessary statistics for the threshold computations are collected from the neighborhood cells (no target return should be present in the guard interval when the statistics are calculated) [2]

.

The Doppler dimension of the DD is partitioned into endo- and exo-clutter regions. The endo-clutter region is heterogeneous in nature, and a clutter boundary exists between the two regions. In these cases, the Doppler dimension is less conducive to CFAR processing, and the CFAR is applied only in the range dimension. In addition, for heterogeneous environments, some modifications of the CFAR algorithms are designed. More details are given in [2, 22].

2.4.1 Types of ISAC Sensing Processing

The primary challenge in designing ISAC radar subsystems lies in the severely limited ability to control the transmitted signal. Although there are proposals to allocate a certain amount of resources specifically for radar functionality, for example, here [59], such approaches have not been implemented in any of the widely adopted modern communication standards. It can be said that the majority of modern communication systems are communication-centric nowadays. Effortless radar signal detection usually requires knowledge of the transmitted signal [2]. Thus, the information about the transmitted signal without any interference (in the context of radar, we can call it the reference signal) should be somehow delivered to the ISAC receiver. There are two most apparent approaches to addressing this issue:

- **spatial diversity based** - in this approach, separate beams could be used to observe the targets (surveillance beam) and to receive the reference signal (reference beam). The interference between surveillance and reference beams, and also clutter seriously limits the performance. Additional processing is needed to remove them; an example of such an algorithm can be found in [60].
- **time and frequency diversity based** - in this approach, the known parts of the signal (for example, pilots) or the signal itself after the demodulation and re-modulation is used [61, 62]. In this case, there is no need for separate beams to distinguish the reference signal and reflections, but signal processing inside the receiver becomes more complicated.

After the reference signal was delivered to the receiver, there are also two common options how to build further processing (both of them have been already mentioned in the Introduction): cross-ambiguity function-based (CAF-based) and channel state information-based (CSI-based).

CAF Based Approach

The CAF-based radar uses the CAF to process the signal [31]:

$$\chi(\tau,\nu) = \int_0^{T_i} y(t)\hat{y}^*(t-\tau)e^{-j2\pi\nu t}dt, \tag{2.44}$$

where T_i is the observation interval of the signal (also called integration time), $\hat{y}$ is the signal from the reference antenna, it is usually called the reference signal. It is important to emphasize that this approach is largely independent of the specific signal structure, in the sense that (2.44) is applicable not only to OTFS, but also to other signal formats such as OFDM (e.g. DAB, DVB-T2, DVB-S2) or other signal types [62].

Nevertheless, it cannot be claimed that this method is entirely signal-structure independent since the internal structure of the signal influences the magnitude of the sidelobes or/and additional (secondary) peaks in the ambiguity function. For example, repeating components of the signal, such as the cyclic prefix in OFDM, can self-correlate, leading to the appearance of *ghost* peaks in (2.44) that do not correspond to any real targets. In some cases, this may limit the maximum range and Doppler shift over which the radar can operate, as the origin of these secondary peaks could be ambiguous. The example of the DVB-T2 signal ambiguity function with a significant number of secondary peaks is shown in Figure 2.8.

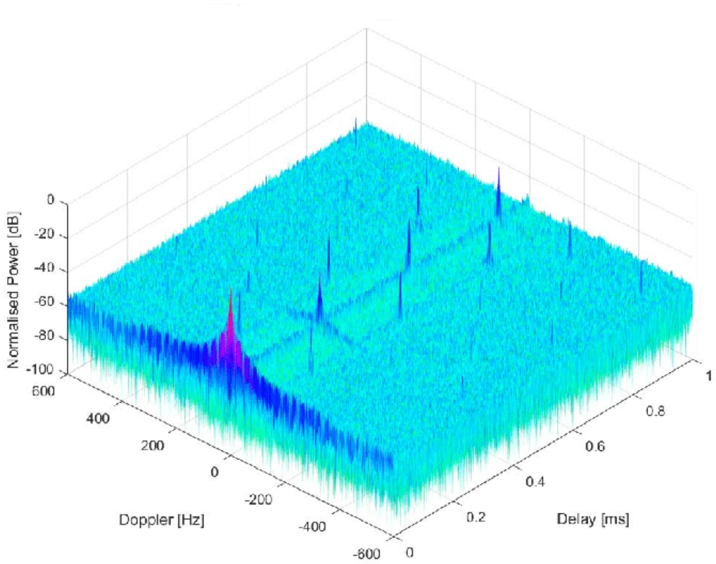

Figure 2.8: The example of the ambiguity function of a DVB-T2 signal (OFDM) [3]. A large number of secondary peaks can be observed; these originate from the pilots, i.e., the repeating sequences within the signal that correlate with each other and introduce such artifacts.

CSI Based Approach

Considering the fact that our work aims to optimize computational complexity by reusing processing blocks for both radar and communication, this approach is more preferable from that perspective. Furthermore, this approach is particularly relevant in the context of OTFS signaling, since both the communication symbols and the target reflection information reside in the same domain. In fact, it can be argued that in the case of OTFS, channel representation in the DD domain alone is sufficient for target detection. In this subsection, we try to abstract from the specific signal OTFS, OFDM or other. However, we will use the concept of 2D signal representation, which we introduced earlier in Subsection 2.1.2.

Recall the dual channel model in the discrete-time domain: (2.18) and (2.20). For simplicity of explanation, let us assume that there is only one target and that the target is located in such a range that $\ell = \tau \times \frac{T}{MN}$ is an integer. The last condition will remove oscillations of the sinc function in (2.18). Assuming a single target with delay ℓ, and substituting equation (2.18) into equation (2.20) and adding noise (w_q), the resulting expression can be written as follows:

$$y[q] = \nu_\ell(\kappa) e^{\frac{j2\pi\kappa(q-l)}{MN}} x[q-l] + w_q. \tag{2.45}$$

In the radar context, the complex scaling coefficient $\nu_\ell(\kappa)$ depends not only on distance and antenna gain, but also on RCS σ_{RCS}, (see (2.36)). This could be used in further processing stages, for example target classification, that are beyond the scope of this work.

After switching from time to TD domain, the received signal is

$$\mathbf{Y} = \begin{bmatrix} y_{0,0} & y_{0,1} & \cdots & y_{0,N-1} \\ y_{1,0} & y_{1,1} & \cdots & y_{1,N-1} \\ \vdots & \vdots & \ddots & \vdots \\ y_{M-1,0} & y_{M-1,1} & \cdots & y_{M-1,N-1} \end{bmatrix}. \tag{2.46}$$

Taking (2.45) and (2.18) into account, the elements of the matrix in (2.46) can be expressed as follows:

$$y_{m,n} = \sum_{p=0}^{P-1} \sum_{i=0}^{M-1} \sum_{j=0}^{N-1} h_p x_{i,j} e^{j2\pi(i+jM)f_{d,p}/f_s} + w_{m,n}. \tag{2.47}$$

By examining the rows of the matrix $\mathbf{Y}$ from the Doppler perspective, one can observe that each element of a row element „samples" the Doppler exponent from (2.45), decimated by a factor of M. The delay of the target can be extracted from the instantaneous CIR estimations. By performing: 1) estimating the instantaneous CIRs along the columns of matrix $\mathbf{Y}$ (for example, with least squares LS estimator), 2) combining them into a new matrix, 3) performing FFTs over rows of the new matrix (i.e., performing spectral analysis of individual CIR coefficients), one can obtain estimates of the target delay and Doppler frequency shift. This means that within the CSI-based approach, the processing can be treated as detecting the peak of a complex sinusoid [58]. Details on how to recompute the estimated ℓ and κ for the actual physical parameters are given in Section 2.4.2. It is shown in [58] that finding the target's peak based on such a method is equivalent to the Maximum Likelihood Estimator (MLE).

2.4.2 The Bistatic Radar Geometry

Before proceeding with the discussion, it should be noted that, within the ISAC framework, the radar subsystem is not necessarily bistatic. For example, the transmitter and receiver could be located in one place. However, in this work, we focus on the case where the transmitter and receiver are located at different sites. This configuration is considered because it allows for greater spatial diversity, improved coverage, and enhanced capability to separate communication and sensing functions.

As mentioned above, the main peculiarity of bistatic radars is the spatial separation between the transmitter and the receiver. The bistatic geometry is visualized in Figure 2.9. The distance L_B between the transmitter and the receiver is called the *baseline range* or simply the *baseline*. R_T is the range between the transmitter and the target. R_R is the range between the receiver and the target. The angles θ_T and θ_R are, respectively, the transmitter and receiver *look angles*, which are taken as positive when measured clockwise from north. They are also called direction-of-arrival (DoA), angle-of-arrival (AoA). The *bistatic angle*, $\beta = \theta_T - \theta_R$, is the angle between the transmitter and receiver with the vertex at the target. It is also called the *cut angle* or the *scattering angle*. It is convenient to use β in the calculation of target-related parameters and θ_T and θ_R in the calculation of transmitter- and receiver-related parameters. The transmitter-to-target-to-receiver range measured by a bistatic radar is the range sum $(R_T + R_R)$. The range sum locates the target somewhere on the surface of an ellipsoid whose focuses are in the transmitter and receiver sites. Usually we are interested in the range between receiver and target. The sum of the range could be recomputed as R_R [22]:

$$R_R = \frac{(R_T + R_R)^2 - L_B^2}{2(R_T + R_R + L_B \sin(\theta_R))} = \frac{L_B \cos(\theta_T)}{\sin(\beta)}. \quad (2.48)$$

To estimate the velocity, it is also necessary to know the angles in the bistatic case [22]:

$$v = \frac{\lambda}{2\cos(\beta/2)\cos(\delta)} f_d, \quad (2.49)$$

where λ is the wavelength of the transmitted signal.

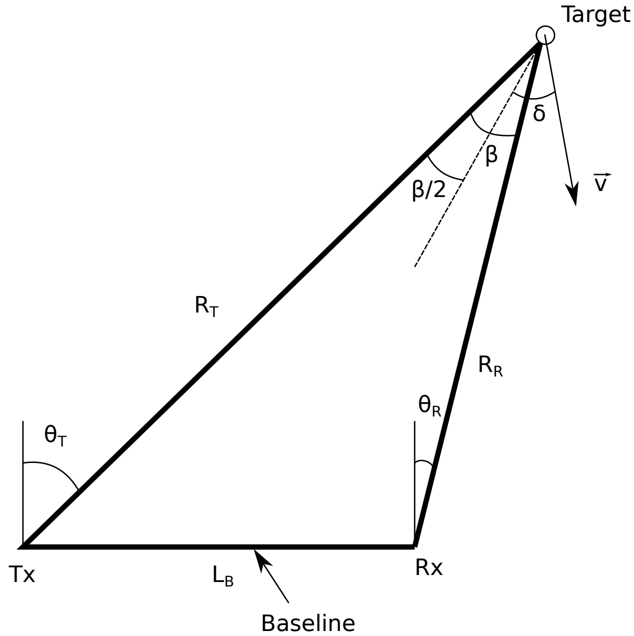

Figure 2.9: The bistatic radar geometry.

The range resolution and velocity resolution of the bistatic radar (without taking into account the accuracy of the measurement θ_R, θ_T, and β) could be calculated as [23]:

$$\Delta R_b = \frac{c}{2\cos(\beta/2)B}, \ \Delta V_b = \frac{\lambda}{2\cos(\beta/2)T}. \quad (2.50)$$

A more detailed analysis of (2.50) reveals that, in the case of a bistatic radar, the space can be divided into three distinct regions:

1. **pseudo monostatic**, $\beta \approx 0°$, in this region the resolution is practically the same as in the monostatic case. This region is located behind the transmitter or receiver.

2. **bistatic**, $0° << \beta << 180°$, in this region, the influence of the bistatic position on the radar characteristics is large.

3. **no resolution**, $\beta \approx 180°$, in this region, there is no resolution in range. This region is located close to the line between the transmitter and receiver.

The bistatic angle affects not only the resolution of bistatic radars but also the RCS. For example, in region 3 (no resolution), forward scattering is observed. In case of forward scattering, the RCS does not depend on the object's shape or material composition, but only on the object's projected area [63].

As shown in (2.48) – (2.50) above, in bistatic radar systems, the angles between the receiver, transmitter, and target play a crucial role in determining the accuracy of the measurements. This angular dependence often necessitates the use of complex antenna configurations for accurate coordinate estimation. In certain cases, targets may enter region 3 (no resolution), where the acquisition of any measurements becomes unfeasible. An alternative solution is offered by multistatic radar systems, in which receivers and/or transmitters are distributed across multiple locations and are capable of exchanging information, thereby enhancing measurement accuracy.

A comprehensive analysis of errors in position determination is presented in [64]. Here, we will only present the results of the error evaluation. We put separate formulas for each type of error:

$$
\begin{aligned}
\frac{\delta R_R}{\delta(R_T+R_R)} &= \frac{1+e^2+2e\sin(\theta_R)}{2(1+e\sin(\theta_R))^2},\\
\frac{\delta R_R}{\delta L} &= -\frac{(e^2+1)\sin(\theta_R)+2e}{2(1+e\sin(\theta_R))^2},\\
\frac{\delta R_R}{\delta \theta_R} &= -\frac{L(1-e^2)\cos(\theta_R)}{2(1+e\sin(\theta_R))^2},
\end{aligned}
\tag{2.51}
$$

where $e = L/(R_T + R_R)$.

In Figure 2.10 the dependence of errors on the angle θ_T is depicted for different baseline lengths.

The $\theta_R = \pm 90^\circ$ end points represent the pseudo-monostatic case, in which the $R_T + R_R$ and θ_R error slopes are a minimum. In general, the maximum error slope (positive or negative) occurs for $-90^\circ < \theta_R < 0^\circ$, that is, when the target is in a region between the transmitter and receiver. Furthermore, the maximum error slope increases almost always as e increases. The exception to these maximum and minimum trends occurs in some regions of the baseline error slope, which, as will be shown in subsequent examples, is generally not a significant contributor to the R_R error.

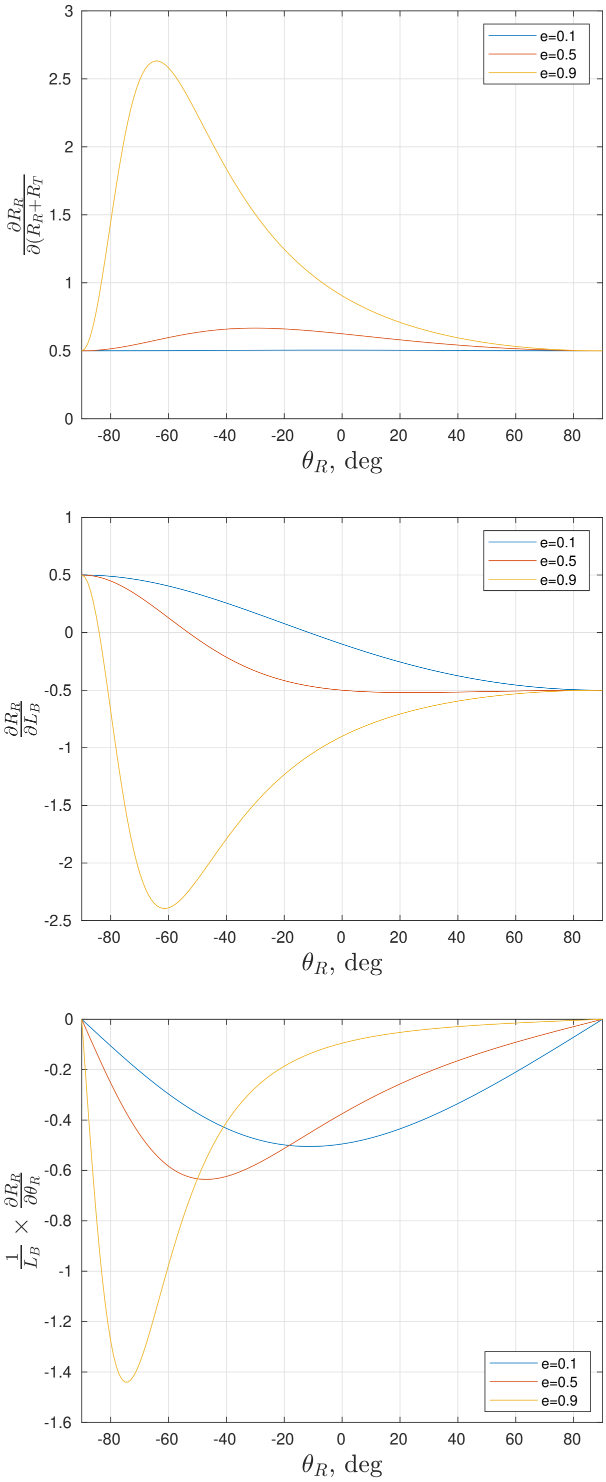

Figure 2.10: The dependency of the errors in position determination on the angle θ_R for different e parameter, depending on bistatic length ($R_R + R_T$), baseline length (L_B) and receiving angle (θ_R).

Chapter 3

Random-padded OTFS in Integrated Sensing and Communication Systems

In this section, the proposed RP-OTFS waveform will be described in detail. The basic idea of the RP-OTFS is to reuse some of the techniques and ideas from the OFDM and apply them to OTFS.

From the communication point of view, the RP-OTFS is a compromise between such waveforms as ZP-OTFS (this waveform can work in a very strong Doppler environment) and OFDM (this waveform is sensitive to Doppler). The RP-OTFS inherits features from both of these signal types: 1) it is Doppler resistant, although to a lesser extent, 2) it employs a straightforward approach to the channel impulse response estimation, very similar to the OFDM waveform.

The RP-OTFS overcomes other known OTFS waveforms in the sense of efficiency of usage of the DD grid resources. In the other types of OTFS, guard intervals are used in the pilot zone of the DD grid to separate the pilots from the data cells after passing through the multipath channel. This requires inserting zero cells into the DD grid. However, this operation reduces the mean power of the pilots in the transmitted signal and subsequently reduces the SNR in the receiver due to inaccurate channel estimation.

However, the absence of zeros in the pilot zone leads to another important improvement: the reduction of the PAPR, at the cost of increasing additional interference between pilots and data. These and other issues, along with possible solutions, will be discussed in the current chapter.

3.1 RP-OTFS Introduction

3.1.1 RP-OTFS Grid

RP-OTFS is an OTFS variant that is designed to make a more efficient use of the resources of the DD grid (see other OTFS-like waveforms in Figure 2.4). In the case of RP-OTFS, the DD grid consists of two zones: the pilot zone and the data zone. The RP-OTFS grid structure is very similar to that of other OTFS variants. But in RP-OTFS, there is no guard zone (inactive carriers with values set to zero) between the pilot zone and the data zone of the grid. Instead, these carriers in the RP-OTFS are used as additional active carriers in the pilot zone.

The pilot zone of the RP-OTFS consists of very short OFDM symbols used for channel estimation, i.e without any data subcarriers inside. This reduces the length of one pilot OFDM symbol without an increase in the sub-carrier spacing, which increases the acceptable channel coherency range (see Section 2.2).

An illustration of RP-OTFS in multiple domains, DD (up) and time (down) domain, is shown in Figure 3.1.

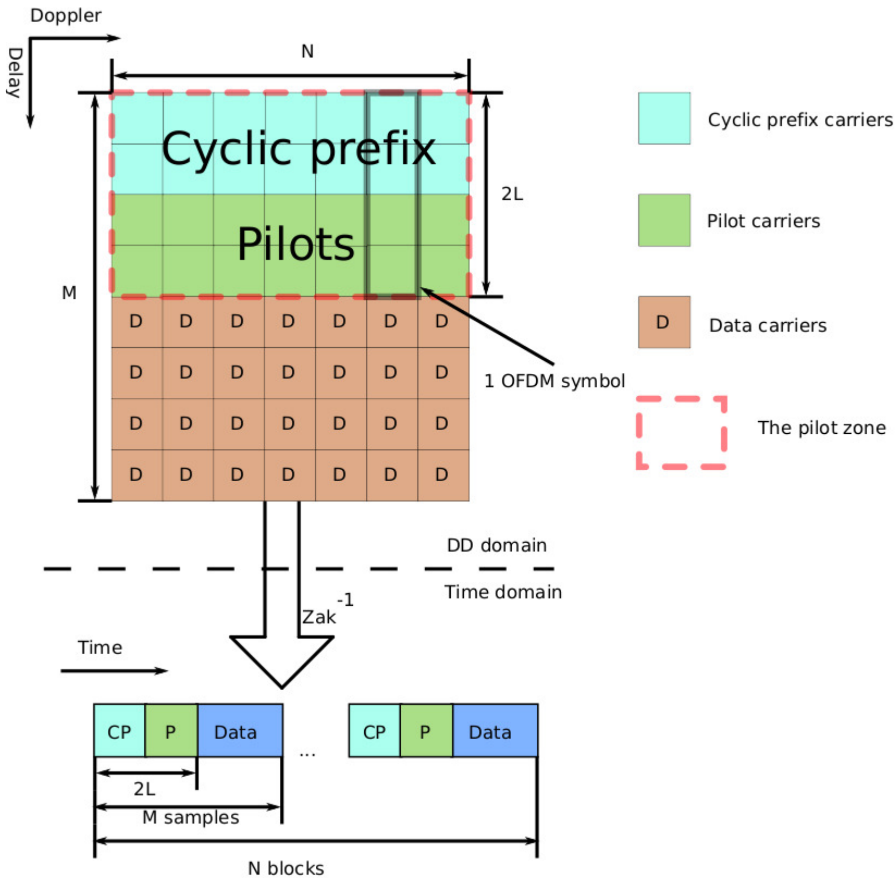

Figure 3.1: The RP-OTFS frame structure in two domains: delay-Doppler (DD), up, and time, down. In the time domain, the signal consists of alternating OFDM pilots and samples corresponding to the columns of the data zone in the DD domain. The RP-OTFS OFDM-based pilots do not carry any data.

The RP-OTFS frame begins with a pilot cyclic prefix, which makes it possible to avoid inter-symbol interference. In this work, we will assume that the cyclic prefix length is sufficient to consider each frame as independent.

Typically, the length of the cyclic prefix determines the maximum duration of the impulse response of an OFDM signal, ensuring that the linear convolution of the channel with the transmitted signal can be treated as a cyclic convolution. The main "body" of the conventional (non-RP-OTFS) OFDM symbol, the part without the cyclic prefix, is significantly longer, as it carries more information for the receiver. This information includes pilots (for channel estimation in the frequency domain) and actual data.

However, in the case of OFDM-like pilot symbols used in RP-OTFS, the situation is different. OFDM-like pilot symbols do not contain any data, and they are used only for instantaneous channel estimation (to be discussed later in this chapter). The maximum delay that can be estimated by the OFDM-like pilot symbol is $\tau_{max} = 1/\Delta f_{pilot}$, where Δf_{pilot} is the pilot spacing inside the OFDM symbol [65]. As in this work, we consider a critically sampled signal ($B/f_s = 1$) and based on the reasoning presented in the previous paragraph, the maximum delay that could be estimated by an OFDM pilot symbol is:

$$\tau_{max} = \frac{1}{\Delta f} = \frac{L}{B} = \frac{L}{f_s}, \tag{3.1}$$

where L is the number of sub-carriers in the OFDM symbol.

To estimate the optimal balance in the length of the cyclic prefix of the OFDM pilot symbol and the OFDM symbol itself, we consider two requirements: the OFDM symbol should be long enough to estimate τ_{max}, but not too long to deal with Doppler. Based on the above requirements and (3.1), the optimal length of the cyclic prefix is L and the OFDM whole pilot symbol is $2L$.

Another consideration that should be taken into account in RP-OTFS is the Doppler frequency shift estimation. Later in this chapter, we will discuss the channel estimation procedure in RP-OTFS: OFDM pilot symbols are used for instantaneous estimations of the channel. Then the Doppler shift estimation is done based on multiple instantaneous estimations of the channel. This means that the distance in time between consecutive OFDM pilot symbols should satisfy the Nyquist criterion from the maximum Doppler frequency shift point of view.

The distance between two consecutive OFDM pilot symbols is equal to M samples (see the structure of the RP-OTFS frame in Figure 3.1). This guarantees the coverage of the Doppler frequency range specified in Table 2.1.

3.1.2 Generation of RP-OTFS Pilots

The generation of OFDM pilot symbols starts in the TF domain. Pilot carriers are modulated using pseudo-random numbers z_k. From the perspective of maintaining constant energy across each sub-carrier, a suitable choice would be quadrature phase shift keying (QPSK), i.e. $\Re(z_k)$ and $\Im(z_k) \in \{-1, +1\}$. The real and imaginary parts of the modulating sequence are distributed uniformly; therefore $\Re(z_k)$ and $\Im(z_k)$ are i.i.d. with the Rademacher distribution. After switching to TD or DD, the pilot samples will have an approximately normal distribution. The last statement is based on two facts:

- the discrete Zak transform is based on the DFT with some rearrangements;
- the DFT of the random variable has approximately a normal distribution (Theorem 4.4.1 in [66]) with some limitations that are not applicable for our case.

The Rademacher distribution of complex pilot values z_k in FD ensures a uniform energy distribution within OFDM-based pilot symbols [67]. This prevents the situation of having zero magnitude carriers in the OFDM-based pilot zone in FD, which causes division by zero in some types of receivers, for example, for a zero forcing one [68].

After the generation of OFDM-based pilot symbols z_k in TF, they are transformed into TD by the DFT, and the CP is added.

It should be noted that OFDM pilots are not strictly part of the DD grid in the conventional sense, as they operate within the TF and TD domains and do not participate in the Zak transform. Instead, the pilots are directly injected into the TD domain. During data signal modulation in the DD domain, the subcarriers corresponding to pilot positions remain inactive. It is only after the combination of pilots and the data samples in TD domain, all sub-carriers become active. Strictly speaking, there are no fundamental limitations preventing the generation of OFDM pilots directly in the DD domain; however, this approach is computationally more complex (as the pilots would then participate in the Zak transform) and, in the author's opinion, less intuitive.

The channel estimation approach proposed within the RP framework can be applied not only with a random sequence inside OFDM pilot symbols, but also using structured sequences, such as Zadoff-Chu (ZC) sequences [69]. However, regardless of the specific sequence used, the principles outlined in this work are fundamental and remain applicable to any sequence used to fill OFDM pilot tones or similar approaches.

3.1.3 Peak-to-Average Power Ratio of the RP-OTFS

When working with OFDM signals, particular attention must be paid to the PAPR. In this subsection, we will analyze the PAPR level of the OFDM pilot symbols and compare it with other OTFS types. The level of PAPR in the case of OFDM is generally characterized by the complementary cumulative distribution function (CCDF) [70].

When evaluating the PAPR, it should be considered that in our case the number of subcarriers in the OFDM symbol is relatively small. In our research, we will use the PAPR CCDF estimate for a small number of subcarriers [71]:

$$CCDF(PAPR) = -\sum_{p=1}^{L} \frac{\binom{L}{p}(-1)^p}{(1+\frac{p\Theta_L \overline{PAPR}}{L-1})^{L-1}}, \tag{3.2}$$

where:

$$\overline{PAPR} = \frac{PAPR}{1-\frac{PAPR}{L}}, \quad \Theta_L = 1 - \sum_{p=0}^{L-1} \frac{\binom{L-1}{p}(-1)^p}{(p+1)^2}. \tag{3.3}$$

The $CCDF(PAPR)$ estimates for OFDM pilot symbols with different L are shown in Figure 3.2, that is, the probability (y-axis) that the PAPR will be equal to or greater than some fixed level (x-axis).

Next, we compare the performance of RP-OTFS (with randomly filled OFDM pilot symbols) with ZP-OTFS and RP-OTFS (with ZC-filled pilots, as a future option). In case of ZC filling of the pilots and ZP-OTFS, the pilots use deterministic patterns. For evaluation of the PAPR in this case we will use the formula from the PAPR definition [72]:

$$PAPR = \frac{max|\breve{x}(t)|^2}{\mathbb{E}\{|\breve{x}(t)|^2\}}, \tag{3.4}$$

where $\breve{x}(t) = \sqrt{2}(\Re x(t) + \Im x(t))$, here we estimate PAPR at the amplifier input (after the quadratures were summed up).

The results of the PAPR evaluations for different pilot schemes are presented in Table 3.1. For RP-OTFS with random sequences, we assumed the acceptable CCDF at 0.2. This means that in 80% of cases of pilot realizations, the PAPR will be smaller than in the table. Data for RP-OTFS with ZC filling (and for ZP-OTFS) were modeled in MATLAB based on (3.4) for all possible combinations of ZC roots.

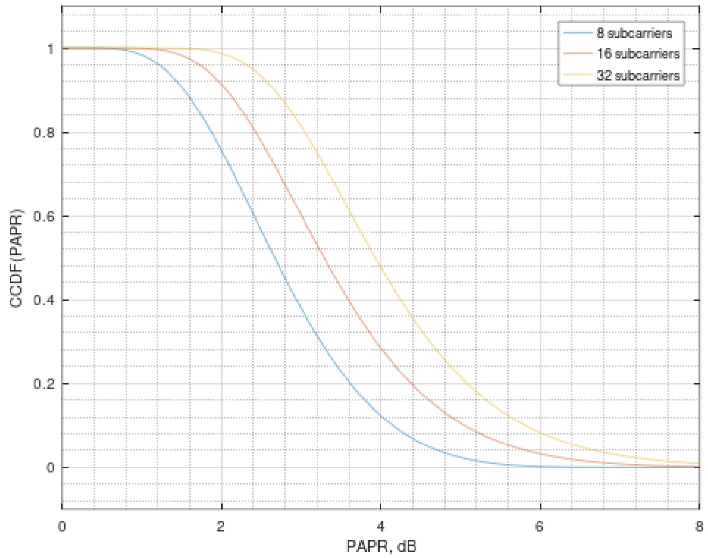

Figure 3.2: The CCDF of the PAPR for OFDM pilot symbols with different length.

Table 3.1: PAPR for different pilot configurations

Waveform name	$L = 8$	$L = 16$	$L = 32$
RP-OTFS	3.8	4.2	5
RP-OTFS (with ZC filling)	3	3	3
ZP-OTFS	9.2	12	14.9

In Figure 3.3, the RP-OTFS and ZP-OTFS waveforms are shown in different domains. This figure clearly illustrates the difference in PAPR between RP-OTFS and ZP-OTFS.

3.1.4 Inter-Carrier Interference in RP-OTFS Pilots

In the case of OTFS orthogonality violation, ICI occurs in OTFS, similarly to the OFDM. In this subsection, we examine the impact of the Doppler effect on RP-OTFS pilot performance. Since the RP-OTFS pilots have the standard OFDM structure with number of sub-carriers L, these pilots are susceptible to the influence of the Doppler effect. Based on the reasoning presented in the previous chapters (e.g. Section 2.2), it can be concluded that the number of subcarriers will be one of the key parameters that will have a great influence on the performance of the RP-OTFS pilot. From this point of view, it is necessary to keep the pilot symbol as short as possible. But, on the other hand, it defines the maximum delay that can be estimated with its help, including fractional delay side lobes, mentioned in the introduction.

We start the analysis with an estimate of the carrier-to-interference ratio (C/I ratio). The C/I ratio represents the ratio of the average power of a given sub-carrier to the total interference power contributed by all other sub-carriers due to loss of orthogonality between sub-carriers:

$$CI(i) = \frac{1}{\frac{(L/f_s \cdot f_d)^2}{2} \sum_{\substack{j=1 \\ j \neq i}}^{L} \frac{1}{(j-i)^2}}, \tag{3.5}$$

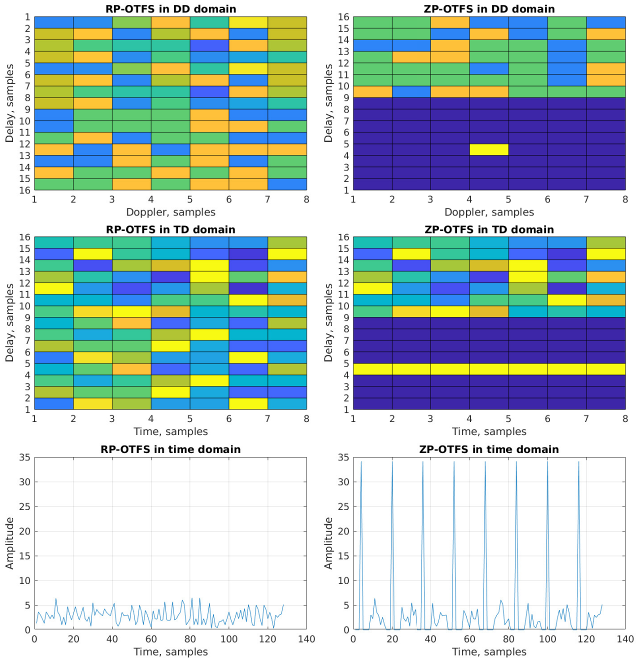

Figure 3.3: The RP and ZP OTFS waveforms in different domains: DD, TD and time.

where f_s - sampling frequency and f_d - Doppler frequency shift. The formula (3.5) is derived in [73].

In Figure 3.4, the dependence of the C/I ratio on the Doppler frequency shift is shown for different lengths L of the pilot symbol. The carrier frequency in this example is 70 GHz. This frequency was chosen to be very close to the maximum carrier frequency (71 GHz) from the 5G specification [12]. It results from Figure 3.4 that RP-OTFS usage is possible in scenarios with a short impulse response. In Table 3.2, maximum velocities of moving objects are shown, for which the C/I ratio of the pilots is kept at least at the level of -40 dB and -50 dB.

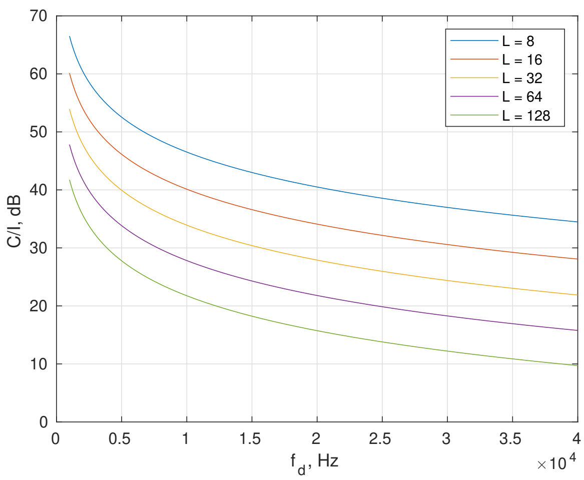

Figure 3.4: The C/I ratio as a function of Doppler frequency shift for different lengths of the pilot symbol L.

Table 3.2: Maximum operating velocity of the 70 GHz RP-OTFS.

	40 dB threshold		**50 dB threshold**	
L	f_d, Hz	v, km/h	f_d, Hz	v, km/h
8	20 000	431	6 900	148
16	9 930	214	3 089	67
32	5 000	108	1 567	34
64	2 465	53	0	0
128	1 336	29	0	0

Several sources in the literature (e.g. [74, 73] and others) suggest that the distribution of interference is approximately Gaussian. Based on this, we will consider the interference between sub-carriers just as an additional source of noise in channel estimation.

We will use a similar approach to [73] to derive the expressions for probability density and joint moments of the ICI, but in the context of the assumptions we made in Subsection 3.1.2.

Let Z be the ICI random variable [73]:

$$Z = \sum_{k=1}^{L} a_k X_k d_k, \tag{3.6}$$

where a_k are real-valued constants, d_k is a QAM symbol assigned to the k-th carrier, the sets of random variables $\{X_K\}_{k=1}^{L}$ and $\{d_k\}_{k=1}^{N}$ are independent. $\Sigma = \mathbb{E}[\tilde{\mathbf{X}}\tilde{\mathbf{X}}^H]$ is the covariance matrix of $\tilde{\mathbf{X}} := (X_1, ..., X_L)^T$. We decompose X_k into real and imaginary parts, $X_k = X_{k,r} + jX_{k,i}, k = 1...L$ and define $\mathbf{X} := [X_{1,r}, ...X_{L,r}, X_{1,i}, ...X_{L,i}]^T$. Currently, the $2L \times 2L$ real-valued covariance matrix $\Sigma = \mathbb{E}[\mathbf{X}\mathbf{X}^T]$ is given by [75]:

$$\Sigma = \frac{1}{2}\begin{bmatrix} \Re[\tilde{\Sigma}] & \Im[\tilde{\Sigma}] \\ -\Im[\tilde{\Sigma}] & \Re[\tilde{\Sigma}] \end{bmatrix} = \begin{bmatrix} \Sigma_{11} & \Sigma_{12} \\ \Sigma_{21} & \Sigma_{22} \end{bmatrix}. \tag{3.7}$$

Based on the reasoning presented in Subsection 3.1.2, the constellation points d_k are i.i.d. with the same probability $p_{k_{r,l},k_{i,l}} = p$. We can also decompose d_k into real and imaginary parts $d_k = d_{k,r} + jd_{k,i}$, $Z := Z_r + jZ_i$. Let us denote the number of constellation points Q.

Let $f_{Z_r,Z_i}(u, v)$ be the joint probability density of the real and imaginary parts of Z.

$$f_{Z_r,Z_i}(u, v) = \sum_{k_{r,1}=1}^{Q} \sum_{k_{i,1}=1}^{Q} ... \sum_{k_{r,,L}=1}^{Q} \sum_{k_{i,L}=1}^{Q} (\prod_{l=1}^{L} p_{k_{r,n},k_{i,n}}) f_{Y_1,Y_2}(u, v), \tag{3.8}$$

where $f_{Y_1,Y_2}(u, v)$ is a bivariate Gaussian density with zero means and 2×2 dimensional covariance matrix whose entries depend on the values of the real and imaginary parts of the OFDM pilot constellation points $\{d_k\}_{k=1}^{L}$. Moreover, one can verify that under our assumptions we have $cov\{Y_1, Y_2\} = 0$, whereas the variance of Y_1 and Y_2 are identical and given by [73]:

$$\sigma_Y^2 = \sum_{i=1}^{L} \sum_{k=1}^{L} a_i a_k \sigma_{11}(i, k)[b_{l_i} b_{l_k} + c_{m_i} c_{m_k}] + \sigma_{12}(i, k)[-c_{m_i} b_{l_k} + b_{l_i} c_{m_k}], \tag{3.9}$$

where $\sigma_{11}(i,k)$ is the (i,k)-th entry of Σ_{11} and $\sigma_{12}(i,k)$ is the (i,k)-th entry of Σ_{12} from (3.7).

Now we rewrite (3.8) considering the same probability p for all modulation symbols and independency of real and imaginary symbol parts:

$$f_{Z_r,Z_i}(u,v) = 2L^2p^N f_{Y_1}(u)f_{Y_2}(v). \tag{3.10}$$

Joint moments of the (Z_r, Z_i) are equal [73]:

$$\mathbb{E}[Z_r^{k_1}Z_i^{k_2}] = 2L^2p^N\mathbb{E}[Y_1^{k_1}]\mathbb{E}[Y_2^{k_2}]. \tag{3.11}$$

In this work, we limit our analysis to second-order moments. Using the Gram-Charlier expansion from [73], it can be shown that

$$\begin{aligned}
&\mathbb{E}[Z_rZ_i] = 2L^2p^N\sigma_Y^2,\\
&\sigma_Y^2 = \left(\frac{LTf_{doppler}}{2}\right)^2 \sum_{r=1,r\neq k}^{L}\sum_{s=1,s\neq k}^{L} \frac{\Re[\psi(\Delta f(r-s))](d_{s,r}d_{r,r}+d_{s,i}d_{r,i})}{(r-i)(s-i)}\\
&+\frac{\Im[\psi(\Delta f(r-s))](-d_{s,i}d_{r,r}+d_{s,r}d_{r,i})}{(r-i)(s-i)},
\end{aligned} \tag{3.12}$$

where ψ is the Fourier transform of the channel coefficient distribution, Δf is the subcarrier spacing in the OFDM symbol pilot.

3.1.5 RP-OTFS Pilot-to-Data Interference

In the context of analyzing different pilot signal design schemes, interference between pilots and data plays an important role. The reasons for the violation of orthogonality are discussed in Section 2. Let us recall that the most significant among them are the fractional Doppler frequency shift and the fractional time delay (i.e. the reflections that are inconsistent with the DD grid). Later in the system model section, we will give the exact equations that describe fractional reflection effects in the context of the OTFS waveform.

The absence of a guard interval between pilots and data leads to interference between pilot and data symbols. This phenomenon is not necessarily related to fractional delays or similar effects; such interference will occur in any multipath channel. A similar phenomenon can be observed in OFDM systems when the length of the cyclic prefix is insufficient.

In the case of RP-OTFS, the data symbols are transmitted without any cyclic prefix at all. Naturally, this approach leaves the data completely unprotected against interference from pilot symbols. On the other hand, data symbols already interfere with each other. As discussed in Section 2, the DD grid exhibits quasi-periodic properties. In multipath channels, shifted copies of the DD grid are superimposed, leading to overlapping of data symbols and resulting in inter-symbol interference. In the case of pilot symbols, knowledge of the transmitted signal and having the estimation of the CSI make it possible to minimize the impact of pilot-induced interference. Figure 3.5 illustrates the process by which interference arises between the pilot and the data symbols.

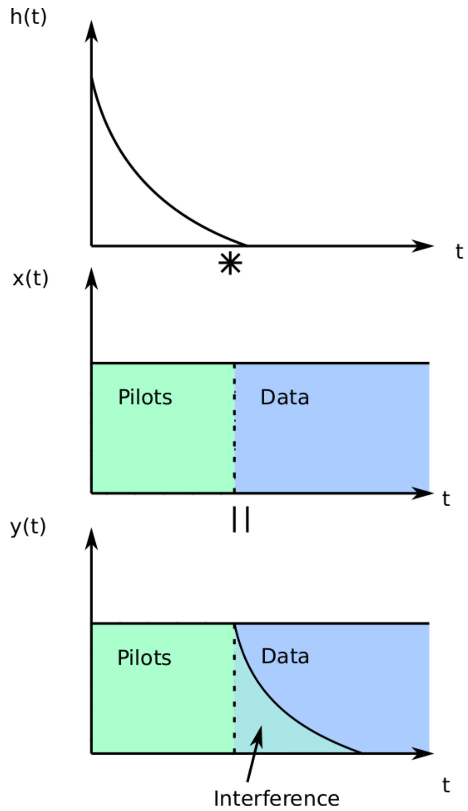

Figure 3.5: Explanation of origin of pilot-to-data interference. After the convolution of the transmitted signal $x(t)$ with the channel, part of the pilot signal starts to interfere with the data. See figure 3.1 to recall the locations of data and pilots of the RP-OTFS in time domain.

Interference Power Re-distribution

The method introduced here is based on DFT properties for periodic signals [76]. If a signal consists of $K \in \mathbb{N}$ repetitions of some basis N samples long sequence $z(n), n \in 0 \cdots N-1$, that is, $\widetilde{z}(n) = \{\underbrace{z(0), z(1), \cdots, z(N-1)}_{z(n)}, \underbrace{z(0), z(1), \cdots, z(N-1)}_{z(n)}, \cdots\}$, and if $\widetilde{z}(n)$ has zero mean, then the DFT of $\widetilde{z}(n)$ will be equal to the $K-1$ times upsampled DFT of $z(n)$:

$$\widetilde{Z}_k = \begin{cases} Z_k, & k \in \{0, K, 2K, \cdots, NK\}, \\ 0, & \text{otherwise}, \end{cases} \tag{3.13}$$

where $Z_k = \mathcal{F}(z(n))$. This effect is also observed in Figure 3.11: it was assumed there that the pilot samples repeat $K = 3$ times and, as a result, $K-1 = 2$ zeros are present between non-zero values of the pilot DFTs in the resulting matrix.

On the receiver's side, in case of a fractional delay, the pilot of the RP-OTFS will interfere with the data. In case of pilot repetition in the **slow-time direction** in the TD domain (corresponds to **Doppler direction** in the DD domain), the interference signal will also repeat. Hence, using the above property, the ICI power distribution on the DD grid could be controlled.

As an example, the DD grid without data (that is, for pilots only) is shown for the new RP-OTFS in two figures: for $K = \frac{N}{2}$ in Figure 3.6 and for $K = \frac{N}{8}$ in Figure 3.7. In both cases, the total power of the pilots

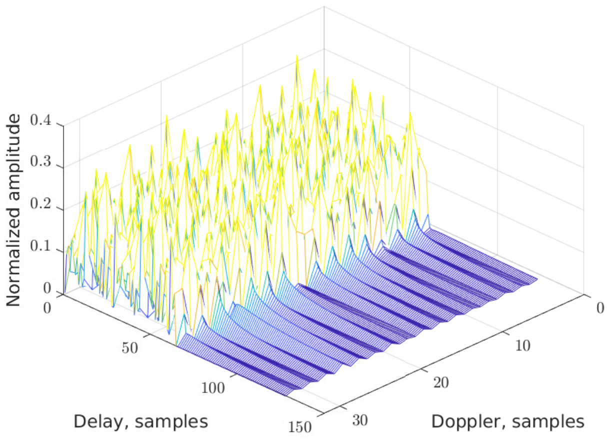

Figure 3.6: The DD map for RP-OTFS with $K = \frac{N}{2}$: every 2nd value in Doppler axis/dimension is different from zero in data zone.

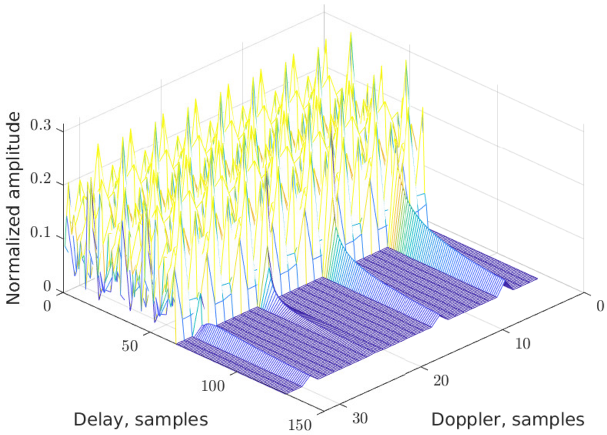

Figure 3.7: The DD map for RP-OTFS with $K = \frac{N}{8}$: every 8th value in Doppler axis/dimension is different from zero in data zone.

is the same, and fractional signal reflections are present. It is clearly visible that interference from pilot to data zone is distributed in completely different manner: in the first case they are smeared equally in the data zone, while in the second case they are concentrated locally only in several stripes (see Figure 3.8).

The columns in the DD grid, where the ICI will be concentrated, can be chosen by multiplying the rows of the TD matrix (only the part of the matrix that contains the pilot samples) by $e^{2j\pi ku/N}$, $u = 0, 1, ..., N-1,$, $k \in 0...K-1$. This will shift the ICI stripes in the Doppler direction by the u columns of the DD grid and can be used to compensate the Doppler offset of the strongest reflection. Only the following columns of the DD grid will be corrupted by ICI :

$$n = u + Ki,\ i \in \{0, 1, ..., N/K\}. \tag{3.14}$$

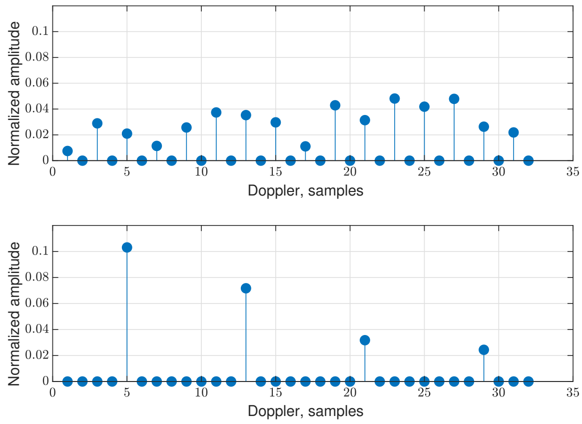

Figure 3.8: Intersections of DD maps along the Doppler axis for the RP-OTFS with $K = \frac{N}{2}$ (up) and $K = \frac{N}{8}$ (down).

It should be noted that the number of repetitions can be equal to any integer number from $0...N$. The boundary case, where $K = N$, means that all pilot symbols are the same. In this case, all ICIs from objects with the same Doppler will be concentrated in one single column. On the other hand, case $K = 0$ means that all OFDM-like pilots are different. In this situation, all ICIs from the objects are uniformly spread across all carriers of the DD grid.

By choosing values for the parameters K and u, the ICI caused by the pilots can be adapted to different scenarios. For example, $K = 0$ could be useful when there is no expectation of strong reflections with fractional delays. In cases when the amount of data to transmit is not very high, some of the carriers of the DD grid could be excluded from data transmission. It makes sense to use these data-free columns to concentrate ICI on them. This can be done by increasing K and choosing an appropriate u if the non-zero pilot slices, present in the DD grid, should be shifted.

The pilot repetition is also particularly important in scenarios where multiple mobile terminals (MTs) transmit data over the same DD grid, by sharing different parts of the grid, e.g. different columns of DD matrix. Each MT uses its own pilots and data symbols, while the data occupy only a portion of the grid (as illustrated in Figure 3.9). Since, in general, MTs are located in different positions, each of them experiences a distinct channel characterized by unique delays and Doppler shifts, resulting in fractional data path on one of the MT's DD grid.

If, for instance, the channel of one MT (MT-1) is not aligned with the grid of another MT (MT-2), pilots of MT-1 can induce oscillations within the grid region of MT-2. Repetition of the pilots redistributes the power of the interference and allows these oscillations to be concentrated in specific regions of the grid while suppressing them in some other, more critical regions. Moreover, due to the random phase of the complex channel coefficients, the resulting interference adds up incoherently, which further improves the signal-to-interference power ratio. This makes multiple MT transmission more reliable.

The figure below illustrates the case of interference between MT-1 and three other mobile terminals (MT-2, MT-3, MT-4), where the same channel is used in all cases. It can be observed that the use of repeating pilot patterns significantly reduces the level of interference.

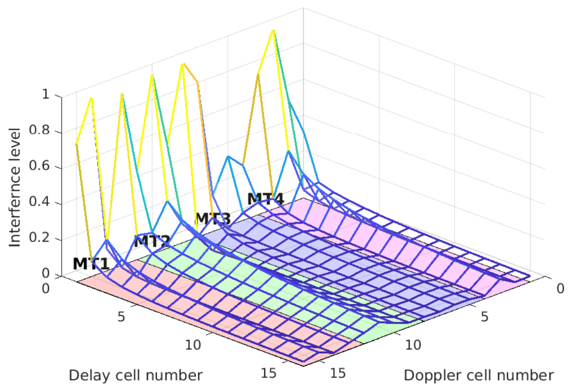

(a) 4 MTs with disabled pilot repetition

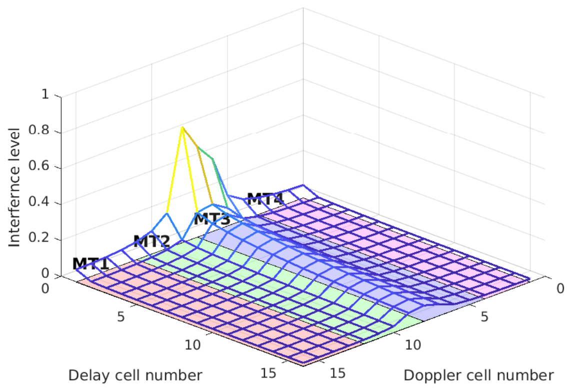

(b) 4 MTs, $K = N$ and $u = N/2$

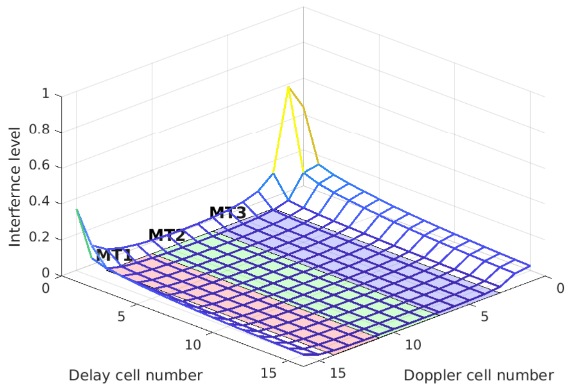

(c) 3 MTs, $K = N$ and $u = 0$

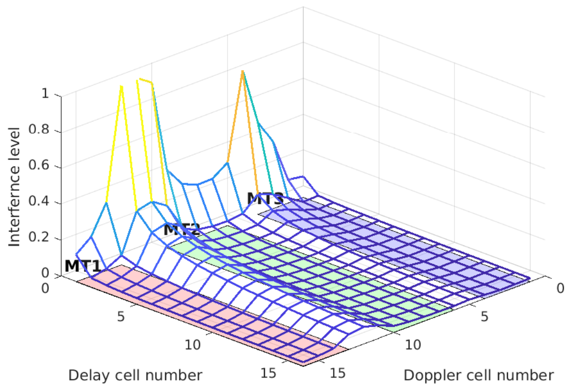

(d) 3 MTs, $K = N/2$ and $u = 0$

Figure 3.9: Different scheduling MT scenarios with different pilot repetition parameters, but the same channel. Without the pilot repeating feature, the interferences from pilots has the highest level (a). Only MT-2 and MT-3 has significant interferences (b). In the case of 3 MTs, two options could be used to reduce interference between (c) and (d). The interferences are combined incoherently.

3.1.6 RP-OTFS Transmitting Process

The principle of the OTFS-based transmitter system with random padding, is explained in Figure 3.10.

The process of generating a RP-OTFS signal begins with the selection of the size and structure of the DD grid. This grid plays a critical role in defining how information is distributed across both the delay and Doppler dimensions. A more detailed discussion of grid dimensioning strategies and parameter selection for various channel conditions from radar system prospective will be presented later in this chapter, specifically in subsection 3.3. These considerations are essential for adapting RP-OTFS to different mobility scenarios.

From a telecommunications standpoint, the primary physical layer constraints that influence the choice of grid parameters are the maximum Doppler shift and the delay spread (or the length of the channel impulse response). These limitations have previously been outlined in Section 3.1.1, where the relationships between channel characteristics and grid resolution were explored.

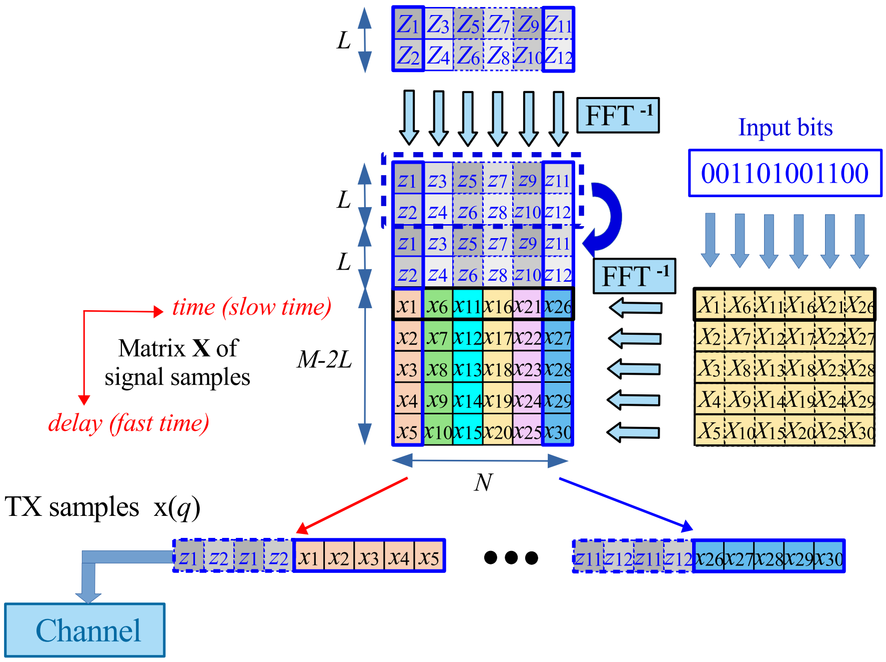

Figure 3.10: The process of combing OFDM pilot symbols into the transmitted RP-OTFS signal (without pilot repetition along Doppler axis) and generating TD samples.

Once the grid parameters have been determined, the next step involves the generation of RP-OTFS pilot symbols. As discussed in Subsection 3.1.2, pilot generation is carried out in the TF domain, which is the native domain for the OFDM waveform. This allows for the use of existing OFDM infrastructure and facilitates a straightforward implementation of pilot design. During this stage, a periodic pilot structure is also selected according to the design principles outlined in Subsection 3.1.2. These pilots are placed in the TF domain, as they are not utilized directly in the DD grid.

In contrast to the pilot placement, the DD grid is exclusively used for data symbol transmission. The process of populating the DD grid with information-bearing symbols is conceptually similar to the allocation of resources within a TF domain resource grid used in traditional OFDM-based systems. Following QAM modulation, the modulated symbols are mapped onto all data region cells within the DD grid. Since pilot symbols are not inserted into the DD domain, the total number of usable data slots per OTFS frame is $M - 2L$.

It is important to note that RP-OTFS does not employ any additional windowing functions in the DD-to-TD conversion process. Therefore, the transformation between the DD domain and the TF domain is accomplished using a straightforward DFT operation. This simplicity not only reduces computational complexity, but also aligns with the modular structure of RP-OTFS signal processing.

After both pilot and data symbols are prepared, they are merged to form a composite TD grid that fully describes the signal to be transmitted. The final stage of transmitter-side signal processing involves reshaping this two-dimensional TD matrix into a one-dimensional vector of size $1 \times MN$.

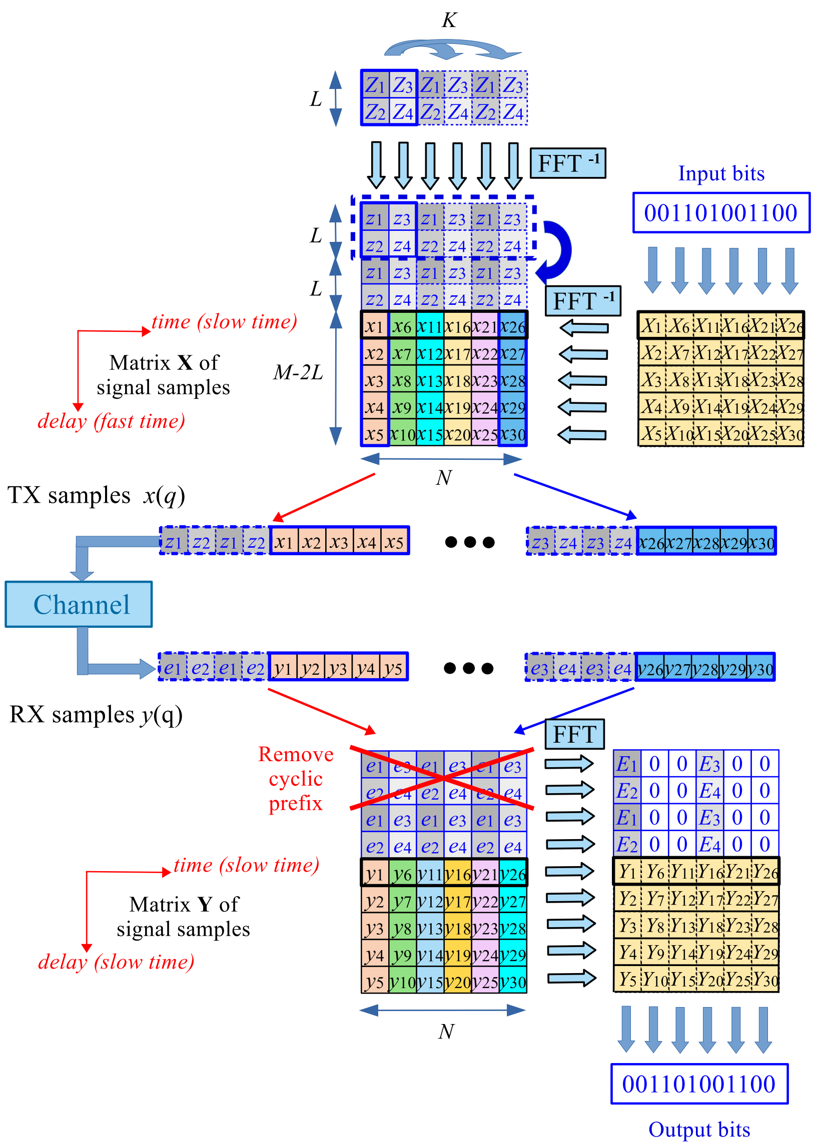

Figure 3.11: Principle of the RP-OTFS-based communication system with pilot repetition.

3.2 RP-OTFS Receiver

The operation of the OTFS signal receiver begins with synchronizing the receiver with the transmitter. In practice, the presence of OFDM pilot symbols allows the use of synchronization methods developed for OFDM systems [77]. Therefore, in this work, we assume that the receiver is already synchronized in time and frequency, and we proceed directly to channel estimation.

We begin the description of the RP-OTFS receiver with the system model. Then we will discuss the channel estimation, equalization, and bit detection procedures. It is well established in the literature that the Mean Square Error (MSE) criterion is optimal under the assumption of AWGN [78]. In this work, we assume that the noise exhibits AWGN characteristics and thus adopt the MSE criterion for RP-OTFS receiver design. In the second part of this Section, we will discuss the radar part of the RP-OTFS ISAC system.

3.2.1 System Model

At the beginning, let us recall the notation that was used in the previous section. The signal received on the DD grid will be denoted as $\mathbf{Y_{DD}} \in \mathbb{C}^{M\times N}$. $\mathbf{x}_m = [X_{DD}(m,0), X_{DD}(m,1), X_{DD}(m,2), ...X_{DD}(m, N-1)]^T$ and $\mathbf{y}_m = [Y_{DD}(m,0), Y_{DD}(m,1), Y_{DD}(m,2), ...Y_{DD}(m, N-1)]^T$ are columns $\mathbb{C}^{N\times 1}$ containing the m-th row of $\mathbf{X_{DD}}$ and $\mathbf{Y_{DD}}$. The column vector contains all samples from the DD grid on the transmitter side $\mathbf{x_{DD}} = [\mathbf{x}_0, \mathbf{x}_1, ..., \mathbf{x}_M]^T$, $\mathbf{x}_{DD} \in \mathbb{C}^{MN\times 1}$ and on the receiver side $\mathbf{y_{DD}} = [\mathbf{y}_0, \mathbf{y}_1, ..., \mathbf{y}_M]^T$, $\mathbf{y}_{DD} \in \mathbb{C}^{MN\times 1}$.

For now, let us focus our attention on the multipath channel representation in the DD-domain. Each reflection in the environment has three parameters that will identify the source of the reflection on the DD-grid. The parameters are the complex path gain, the Doppler frequency offset, and the delay. Let us denote the complex gain of the pth path h_p, the delay τ_p, and the Doppler offset ν_p. For simplicity, we will normalize delay and Doppler to the grid element resolution in the following way: $\ell_p = \tau_p \times \frac{T}{MN}$ is normalized delay, and $\kappa_p = \nu_p \times NT$. Here, it is important to notice that l_p and k_p are not necessarily integers. We will denote the set of delays as $\mathcal{L} = \{\ell_p\}$, and $K_\ell = \{\kappa_p \mid \ell = \ell_p\}$. In this work, we will assume that maximum delay does not exceed the length of the OFDM pilot symbol, L, and the Nyquist criterion in the Doppler direction is also met $(-N/2 \leq k_p \leq N/2)$.

It is shown in [4], a channel with fractional Doppler and fractional delay could be modeled in the DD domain, by the following formula:

$$\boldsymbol{\nu}_{m,l}(k) = \frac{1}{\sqrt{N}} \sum_{\ell\in\mathcal{L}} \left(\sum_{\kappa\in K_\ell} \nu_\ell(\kappa) e^{j2\pi k(m-l)} \zeta_N(\kappa - k) \right) sinc(l-\ell), \tag{3.15}$$

where $\zeta_N(x) = \frac{1}{\sqrt{N}} \frac{\sin(\pi x)}{\sin(\frac{\pi x}{N})} e^{\frac{j\pi x(N-1)}{N}}$ is a periodic sinc function, m is a coordinate of some reference sample in the delay direction (as the channel impulse response changes in time), l is an amount of delay samples from the reference sample, k is a Doppler offset normalized to the resolution of the grid.

The result signal after passing the Doppler multipath wireless channel could be obtained as the sum of circular convolutions in the DD domain for each delay

$$\mathbf{y}_m = \sum_{l\in\ell} \boldsymbol{\nu}_{m.l} \circledast \mathbf{x}_m \tag{3.16}$$

For more convenient usage, circular convolution in (3.16) could be replaced by multiplication by matrix $\mathbf{G}$. The matrix $\mathbf{G}$ consists of the submatrices $\mathbf{K_{m,l}} \in \mathbb{C}^{\mathbf{N}\times\mathbf{N}}$. Each submatrix $\mathbf{K_{m,l}}$ is defined [4]:

$$\boldsymbol{K}_{m,l} = \begin{bmatrix} \boldsymbol{\nu}_{m,l}(0) & \boldsymbol{\nu}_{m,l}(N-1) & \boldsymbol{\nu}_{m,l}(N-2) & \dots & \boldsymbol{\nu}_{m,l}(1) \\ \boldsymbol{\nu}_{m,l}(1) & \boldsymbol{\nu}_{m,l}(0) & \boldsymbol{\nu}_{m,l}(N-1) & \dots & \boldsymbol{\nu}_{m,l}(2) \\ \vdots & \vdots & \vdots & \ddots & \vdots \\ \boldsymbol{\nu}_{m,l}(N-1) & \boldsymbol{\nu}_{m,l}(N-2) & \boldsymbol{\nu}_{m,l}(N-3) & \dots & \boldsymbol{\nu}_{m,l}(0) \end{bmatrix}. \tag{3.17}$$

The arrangement of the submatrices $\boldsymbol{K}_{m,l}$ from (3.17) in $\mathbf{G}$ is as follows:

$$\mathbf{G}[\, mN+1...(m+1)N,\ (m-l)N+1...(m-l+1)N \,] =$$

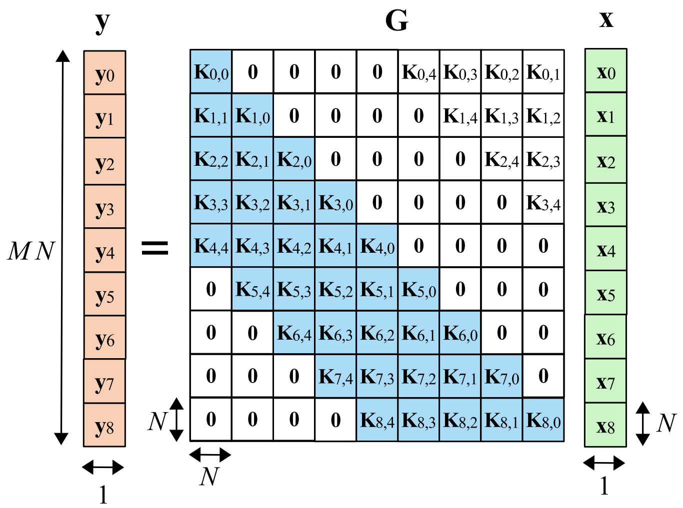

Figure 3.12: The example of the placement of submatrices $\mathbf{K_{m,l}}$ within matrix $\mathbf{G}$ [4].

$$= \begin{cases} \mathbf{K}_{m,l}, & m \in 0 \cdots M-1, \;\; l \in 0 \cdots (M-m)N, \\ 0, & \text{otherwise.} \end{cases} \tag{3.18}$$

The visualization of the placement of the submatrices $\mathbf{K}_{m,l}$ within the matrix $\mathbf{G}$ is given in Fig. 3.12.

Based on the above description, the signal that passes through the multipath channel with Doppler frequency shifts can be written in Bayesian General Linear Model (BGLM) form [79]:

$$\mathbf{y} = \mathbf{G} \times \mathbf{x} + \mathbf{w}, \tag{3.19}$$

where $\mathbf{w}$ is a noise vector in the DD domain.

The vector $\mathbf{w}$ is defined as $\mathbf{w}_m = [W_{DD}(m,0), W_{DD}(m,1), ..., W_{DD}(m,N-1)]^T$, $\mathbf{w} = [\,\mathbf{w}_0,\, \mathbf{w}_1,\, ...,\, \mathbf{w}_{M-1}\,]^T$. The matrix $\mathbf{W}$ is the result of the Zak transform performed on the time domain noise vector $w \sim \mathcal{N}(0, \sigma^2)$, where σ^2 is the variance of the noise (here we assume that the rectangle windowing function was used in the Zak transform). After the Zak transform of w, one obtains $\mathbf{w} \sim \mathcal{N}(0, \sigma^2/N)$ [80].

The representation of the channel model in the form of BGLM in the DD domain allows us to directly use the well-known estimators from OFDM to OTFS signals, for example, the Minimum Mean Square Error (MMSE) estimator. It is worth noting that sometimes estimation of $\mathbf{G}$ may be impossible to obtain "directly from pilots", as in the OFDM case. The example of such a situation will be discussed in the next subsection.

Although the OFDM pilot signals of the RP-OTFS are defined in the TF domain, it nevertheless has its representation in the DD domain. Therefore, using the model presented above, it is possible to apply it to the entire RP-OTFS grid without separating it into pilots and data.

3.2.2 Channel Estimation and Equalization

Channel Estimation

The RP-OTFS channel estimation process begins with an initial estimate of the instantaneous channel coefficients $h[l, q]$, where l is a delay index and q is an index of the sample starting from the beginning of the RP-OTFS frame (see Figure 3.13).

At this stage, each OFDM pilot symbol is processed independently and separately, resulting in stable channel estimations. For this instantaneous channel estimation, any standard algorithm suitable for OFDM can be used. The RP-OTFS instantaneous channel estimator RP-OTFS could be built on the approach described in [81, 78], with some modifications. Here we will provide an example of the linear estimator. The initial channel coefficient estimation is done making use of the least squares (LS) criterion and the n-th pilot signal:

$$[h[0,nM-L],...,h[L-1,nM-1]] = \mathscr{F}^{-1}\frac{\mathscr{F}\{c[n*M-L],...,c[n*M-1]\}}{\mathcal{F}[z[n*M-L],...,z[n*M-1]]},\ n = 0...N-1. \quad (3.20)$$

where $\mathscr{F}$ - the Fourier transform and $\mathscr{F}^{-1}$ - the inverse Fourier transform. Then $h[l,q]$ should be filtered by LMMSE filter as was previously discussed in Subsection 2.3.

It is important to highlight two key points here. First, in (3.20), we obtain averaged channel estimates, within the OFDM pilot symbol (as previously discussed). Second, channel estimates are not continuous: there is a gap of $M-2L$ samples between successive estimates.

The common point for OFDM and RP-OTFS waveforms is that the data are located between pilots. But the main peculiarity is that in the case of OFDM, the data and the pilots are both inside an OFDM symbol, and in the case of the RP-OTFS, the data subcarriers are separated by OFDM-based pilots.

After obtaining the estimation of the instantaneous CIR for each delay in the range of $[0\cdots L]$ samples, samples at positions $n = L+l+iM$, $i \in \{0,\cdots,N-1\}$, $l \in \{0\cdots L\}$ contain instantaneous CIR information at the delay of l samples, estimated at different moments of time. In the RP-OTFS, we obtain the CIR estimate for the delay l once per M samples. The complete CIR can be recovered by interpolating the instantaneous CIR estimations for each l separately (in OFDM, the channel frequency response (CFR) estimates are interpolated).

The choice of the interpolation method was discussed by us in [43]. Here we briefly recall the main conclusions. The choice of the interpolation method is based on the expected behavior of the CIR function, mainly on its derivatives. We will base our interpolation analysis on (3.15), which takes into account the effect of fractional reflections. However, during analysis of the CIR function, we do not consider the particular DD grid; therefore, for simplicity, we can assume that no fractional reflection occurs. Then we can also assume that $(\kappa-k)$ and $(l-\ell) \in \mathbf{Z}$, hence $\zeta_N(\kappa-k) = \sqrt{N}$, $\mathrm{sinc}(l-\ell) = 0$ and

$$\nu_{m,l}(k) = \begin{cases} \nu_\ell(\kappa)e^{2\pi j\kappa(m-l)/MN}, & \text{if } l=\ell \text{ and } k=[\kappa]_N, \\ 0, & \text{otherwise.} \end{cases} \quad (3.21)$$

By calculating the derivatives of (3.21) over m, one obtains the following recurrent formula:

$$\frac{\nu_{m,l}(k)}{m} = (2\pi j\kappa/MN)^p e^{2\pi j\kappa(m-l)/MN}. \quad (3.22)$$

As $\lim_{p\to\infty}(2\pi j\kappa/MN)^p = 0$ for $MN >> \kappa$, the magnitude of the derivatives will decrease with increasing p. The rate of decrease in derivatives depends on the size of the grid MN and on the Doppler frequency shift κ. This means that for the same grid size, the optimal interpolation method depends on the environment. For the cases where the Doppler effect is not very high, low-order interpolating polynomials can be used, for example, simple linear interpolation. At the same time, when the value of κ increases, more advanced interpolation methods, such as cubic spline interpolation, should be exploited. Generalizing to the more general case: when the Doppler frequency shift is not constant during the RP-OTFS frame, for example, when a target is accelerating, analysis of Equations (3.21) and (3.22) is more complicated. In this case, κ becomes dependent on m and additional degrees of freedom of an interpolation function are required to fit it.

After obtaining CSI estimation in the time domain (i.e., CIR $\nu_{m,l}(k)$), Equations (3.15)–(3.18) are used to transform CSI into the DD domain and model data transmission directly in the DD domain with (3.19).

The idea of the channel estimation algorithm, specified here, is summarized in Alg. 1, however, without precise indexing of elements of all vectors.

The example of the channel estimation process of the RP-OTFS receiver is shown in Figure. 3.13. In this example, the following DD grid parameters were used: $M = 7$, $N = 4$, and $L = 2$. The first four samples of each received block (symbol) are reference ones, e.g., repeated (CP of the RP-OTFS OFDM symbol and symbol itself) pilot pairs ($L = 2$): $[z_1, z_2]$, $[z_3, z_4]$, $[z_5, z_6]$ and $[z_7, z_8]$. They are used to calculate the momentum (instantaneous) values of all CIR taps, that is, $h_0(n)$ and $h_1(n)$. Since reference samples are sent only from time to time, not all channel taps are calculated, but only some of them. In our example, the following ones: $[h[0, 2], h[1, 3]]$, $[h[0, 9], h[1, 10]]$, $[h[0, 16], h[1, 17]]$ and $[h[0, 23], h[1, 24]]$. The remaining values must be found by interpolation or extrapolation. In the simulation section, different interpolation techniques are tested: 0-order, linear, pchip, and spline.

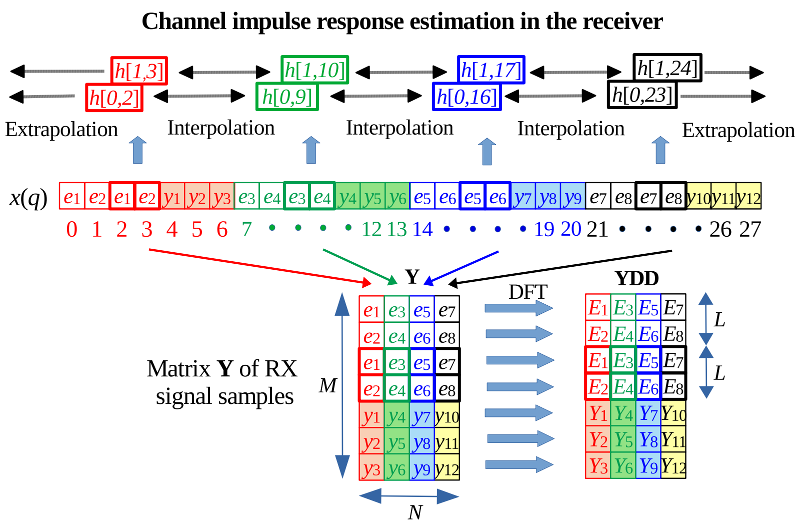

Figure 3.13: Diagram explaining calculation of all momentum CIR taps $h[0, 2], h[1, 3], ...,$ $h[0, 9], h[1, 10], ...,$ using pilot data and interpolation/extrapolation.

An alternative approach to the interpolation above is to build a 2D interpolator (or filter), where we use pilots in the Doppler direction and delay direction at the same time, by appling separable filters. This implies that we use two one-dimensional filters, one in the delay direction and the other in the Doppler direction. The resulting increase in performance has been shown to dominate over the loss in optimality when going from general two-dimensional filters to separable ones based on two-dimensional filters [48].

Data-to-Data Interference Reduction

The data-to-data interference reduction is based on extrapolating the CIR, which was obtained in the previous step. The fractional delay component in (3.15) is represented by the sinc function and the Doppler component does not depend on the fractional part of the delay. This means that any fractional delay will produce sinc oscillations in the CIR in the DD domain, the ocillations are not limited by the length of the OFDM pilot symbol L. It is evident that the part of the impulse response beyond the sample with index L cannot be estimated using OFDM-pilot symbol of length L. This will generate interference not only between pilots and data, but also between data carriers. Since the RP-OTFS pilot zone are represented by independent OFDM-pilots in every column of the DD grid, we can treat each particular column of the received DD grid as a separate one in the context of this algorithm. We also assume that in the propagation channel the maximum reflection delay corresponds to the delay $L-2$ in the DD grid, i.e. there is no reflection at least in the last two samples of the CIR.

Based on the assumptions above, we can reconstruct the oscallations generating factor using the following formula, which is based on (3.15).

$$F(q) = A \cdot \mathrm{sinc}(0.5 + q), \tag{3.23}$$

where q is the sample number ($q = 0...M - L - 1$) and A is a complex parameter that should be estimated. After receiving and estimating the channel, we use the last two samples of CIR to estimate the complex parameter A:

$$A = \frac{h[q, L-2] + h[q, L-1]}{2}. \tag{3.24}$$

Estimation of A is done separately for each column of the DD grid. Let us denote the part of the CIR that could be estimated with RP-OTFS pilots as $\hat{h}$. Then we append the extrapolated part ($F(q)$) to $\hat{h}$ and get the reconstructed CIR response of the arbitrary length. The sinc oscillations attenuate relatively fast with the distance and extrapolating $M - 2L$ is enough to get a sufficiently (for further processing) reconstruction of the channel.

To check the efficiency of the data interference compensation method based on sinc extrapolation, proposed above, we provide the results in the simulation Section 4.2.

LMMSE Channel Equalization in RP-OTFS

In the RP-OTFS system model subsection 3.2.1, the input-output RP-OTFS system model was derived. The Equation (3.19) describes the relationships between the transmitted and received signal in the DD domain. This representation is very convenient, as it allows the use of well-studied algorithms of linear receivers, for example, LMMSE. After channel estimation and CSI interpolation, we need to estimate $\hat{\mathbf{G}}$ based on $h[q, l]$. This could be done using the formulas below.

Let denote:

$$\tilde{\nu}_{n,m,l} = h\big[l,\, m + (n-1)M\big], \quad n = 1, \ldots, N,\ m = 1, \ldots, M,\ l \in L. \tag{3.25}$$

Algorithm 1 Algorithm of CIR estimation and sinc extrapolation in the RP-OTFS-based ISAC

for each OFDM-pilot symbol j **do**
    Channel estimation
    Remove CP in z_j
    $E \leftarrow \mathrm{DFT}\{e_j\},\ Z \leftarrow \mathrm{DFT}\{z_j\}$
    $H \leftarrow \mathrm{LMMSE}\{E, Z\}$
    $h_j \leftarrow \mathrm{IDFT}\{H\}$
end for
for each delay tap j in h_j **do**
    Channel interpolation
    Interpolate between $h_j(n + j)$ and $h_l(M \cdot n + j)$
end for
for each symbol j **do**
    Data ICI cancellation
    for each delay tap j **do**
        $A_j \leftarrow 0,\ A_j \in \mathbb{C}^M$
        for $l \leftarrow L - 2$ to L **do**
            $A_j \leftarrow h[l, j \times M + l]$
        end for
        $A_j \leftarrow A_j/2$
        for $q \leftarrow L$ to M **do**
            $F_j \leftarrow A \times \mathrm{sinc}(0.5 + q)$
            $h[l, q] \leftarrow F_j$
        end for
    end for
end for

The estimate of $\boldsymbol{\nu}_{m,l}(k)$ could be derived from (3.25):

$$\hat{\boldsymbol{\nu}}_{m,l}(k) = F_N \, \tilde{\nu}_{m,l}, \quad m = 1, \ldots, M, \; l \in L, \tag{3.26}$$

where

$$\tilde{\nu}_{m,l} = \begin{bmatrix} \tilde{\nu}_{1,m,l} \\ \tilde{\nu}_{2,m,l} \\ \vdots \\ \tilde{\nu}_{N,m,l} \end{bmatrix},$$

and F_N is the DFT matrix of size N. Next:

$$\hat{\mathbf{K}}_{m,l} \;=\; F_N \, \mathrm{diag}\big(\tilde{\nu}_{m,l}\big) \, F_N^H, \quad m = 1, \ldots, M, \; l \in L. \tag{3.27}$$

Finally, reconstructing the estimation of $\mathbf{G}$ based on the same approach as in 3.18 (and Fig. 3.12)

$$\begin{aligned} &\hat{\mathbf{G}}[\; mN+1...(m+1)N, \; (m-l)N+1...(m-l+1)N \;] = \\ &= \begin{cases} \hat{\mathbf{K}}_{m,l}, & m \in 0 \cdots M-1, \; l \in 0 \cdots (M-m)N, \\ 0, & \text{otherwise.} \end{cases} \end{aligned} \tag{3.28}$$

In such case, the LMMSE equalizer for the RP-OTFS could be written as:

$$\widehat{\mathbf{d}} = \mathbf{G}^{\dagger} \left[\mathbf{G}\mathbf{G}^{\dagger} + \frac{\sigma_w^2}{\sigma_d^2} \mathbf{I} \right]^{-1} \mathbf{y}, \tag{3.29}$$

where $\dagger$ denotes complex conjugation and transposition, σ_w^2 and σ_d^2 are variances of noise and data, respectively. A fast algorithm to solve (3.29) is proposed in [49].

3.2.3 Bit Detection

Each equalized data cell in the DD grid contains QAM constellation point estimation. The equlized data cell are demodulated using the Maximum A Posteriori Probability (MAP) approach to produce values representing beliefs regarding a received bit b being equal to 0 or 1, expressed in a form of Log-Likelihood Ratio (LLR):

$$LLR(b) = log \frac{P(b=0|y[q])}{P(b=1|y[q])}, \tag{3.30}$$

where s is an element of the data vector received after equalization $\hat{s}$.

For the sake of receiver design, a simplified MAP demodulator proposed by Viterbi [82] could be used, which approximates the logarithmic LLR value of a bit b based on the distance difference between the closest constellation points:

$$LLR(b) \approx -\frac{1}{\sigma^2} \left(\underset{\lambda_0 \in \Lambda_0}{\mathrm{argmax}} |s - \lambda_0|^2 - \underset{\lambda_1 \in \Lambda_1}{\mathrm{argmax}} |s - \lambda_1|^2 \right), \tag{3.31}$$

where Λ_0 and Λ_1 are the sets of ideal constellation points corresponding to bit states 0 and 1 respectively, whereas σ^2 is a noise variance of a sub-carrier over which the constellation point being demodulated was conveyed.

3.3 Sensing with RP-OTFS

3.3.1 General Considerations

In this dissertation we focus on the CSI based approach, in this case sensing processing begins with the $\mathbf{G}$ matrix estimation. The estimation process was discussed before, now let us focus on format of $\mathbf{G}$. Each subdiagonal of the $\mathbf{G}$ contains information about specific ℓ, κ and $\nu_\ell(\kappa)$. This property arises from the internal structure of the matrix $\mathbf{K}_{m,l}$ (consists of cyclic shifts of $\boldsymbol{\nu}_{m,l}(n)$) and the arrangement of $\mathbf{K}_{m,l}$ in $\mathbf{G}$ (see (3.17), (3.18) and Figure 3.12). This way of presenting information is not suitable for standard radar processing algorithms. Therefore, before target detection, an additional step is needed to map $\mathbf{G}$ to the standard DD grid format (different delays in rows, different Doppler frequency shifts in columns). This mapping should be performed as follows:

$$\mathbf{G}_{DD}[m,n] = \mathbf{G}[m \cdot N + n, l_0 \cdot N], \tag{3.32}$$

where l_0 is the time shift of the CSI estimation relatively to the begging of the OTFS frame. In most practical cases $l_0 = 0$, the range of l_0 is $0 \ldots L-1$.

In Figure 3.14 an example of the matrix $\mathbf{G}_{DD}$ after the mapping is shown. Reflections from two *static* objects (so-called *clutter*) and from one moving object/target are visible in it.

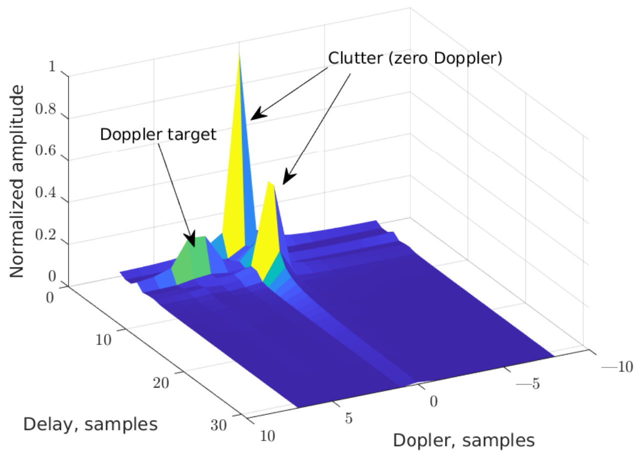

Figure 3.14: $\mathbf{G}_{DD}$ after mapping from $\mathbf{G}$.

After the mapping, the standard radar processing techniques can be applied.

Figure 3.15 illustrates the summary block diagram of the ISAC receiver processing. It is assumed that the signal is perfectly synchronized with the strongest path of the multipath environment. It is also assumed that the signal is already transformed to the DD domain, so the processing is done mainly in the DD domain, except the channel estimation part because of the nature of OFDM-based pilots. The subsequent processing is divided into two branches: radar system processing and communication system processing.

In the radar subsystem only OFDM pilots are processed, the rest of the DD grid is ignored. First, the pilots are transformed to the TF domain where the instantaneous CFRs are estimated. The CFR estimates are then transformed to the TD to obtain an instantaneous CIR. The CIR estimates are used in the communication processing branch. Finally, a total of N CIR estimates are used to construct the DD map for the radar detector.

The results of the channel estimation are also utilized in the second branch—the communication processing path as it was discussed in Section 3.2.2.

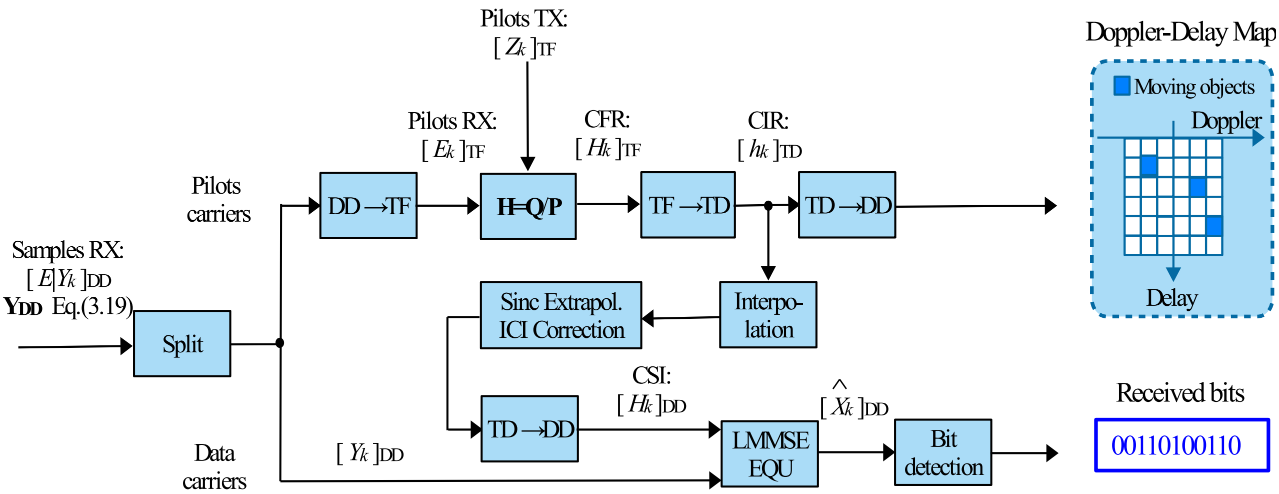

Figure 3.15: The system model based processing diagram.

3.3.2 Sensing Use-Cases

In this subsection, we will present an example of choosing values of the global parameters (M, N, and L) of the DD grid in the radar context. We start a discussion with an introduction of *use case* scenarios, and then present an adaptation of the grid parameters. We define three use-cases for ISAC:

A. **very high speed**: civil airplanes, high speed trains and etc; in this group we consider flying objects with speed v in the range 120...340 m/s;

B. **medium speed**: vehicular, drones; in this group we have moving objects with speed v in the range 10...60 m/s;

C. **very low speed**: pedestrians, low speed vernaculars; to this group belongs objects moving with speed v up to 2 m/s.

As the Doppler frequency shift depends not only on the movement velocity of the objects but also on the carrier frequency, we assume to choose the carrier frequency the same as in the previous section, i.e. equal to 70 GHz:

$$f_{d_{max}} = \frac{v}{\lambda} = \frac{v f_c}{c}, \tag{3.33}$$

where $\lambda = \frac{c}{f_c}$ denotes a wavelength. For unambiguous Doppler measurements, the sampling rate in the Doppler direction should satisfy the Nyquist theorem and, therefore, could be defined as $\frac{f_s}{M}$. Using (3.33), the maximum value of the parameter M that meets this requirement is given by:

$$M_{max} = \frac{f_s}{2 \cdot f_d}. \tag{3.34}$$

Next, we take into account the range resolution of the DD grid. Communication systems operating in the range of tens of gigahertz typically make use of the bandwidth (BW) of tens or even hundreds of megahertz. As a sampling rate $f_s = B$ of the complex signal, this gives a very high range resolution. For example, $BW = f_s = 100$ MHz gives range resolution up to 3 m. Such a high resolution will be useless for use-case A, but could be sufficient for use-case B. The range time resolution of 3 m may not be enough for some applications with targets from use-case C. In such cases, increasing of the BW should be considered.

Another aspect that should be taken into consideration for ISAC systems in the context of their radar sections is the value of integration time, that is, how long targets from different use cases (A, B or C) can stay in one resolution element of the DD grid. For resolution in range direction, the calculations are trivial: the time required for a moving object to cross the resolution element is $\Delta t_{el} = \frac{c}{f_s \cdot v}$. In order to be able to combine the reflection coherently during the Zak transform, the frame time duration should be much shorter than the time spent by the target in one resolution element [22]:

$$\frac{NM}{f_s} \ll \Delta t_{el}. \tag{3.35}$$

By changing the parameters of the DD grid M and N (keeping their product MN constant), different resolutions in Doppler and maximum unambiguous Doppler can be achieved. In terms of computational complexity, decreasing N (and increasing M) is more efficient than decreasing M (and increasing N). The reason is the computational complexity of the discrete Zak transform is $\mathcal{O}(MN \log N)$. In terms of RP-OTFS, keeping N as small as possible is also more profitable because the pilot overhead of RP-OTFS is directly proportional to N. N defines the number of the OFDM pilots. On the other hand, the decrease in the value of N will result in worse Doppler resolution.

Below an example is presented on how to choose the RP-OTFS parameter values in use case B. At the end of this part, for illustration purposes, we provide a general table with results for the three use cases. Before we start, it is important to note that applying the RP-OTFS to targets from the use case A is possible in an environment where all propagation paths have practically the same delay (see Table 3.2). Nevertheless, case A is retained in our example for potential applicability with alternative pilot configurations.

We are making the following assumptions:

- the carrier frequency equals 70 GHz, as before;
- BW of the signal equals 100 MHz;
- the signal is critically sampled, i.e. $f_s = 100$ MHz.

We start by defining the maximum Doppler value based on (3.33): $f_d = 14$ kHz. Now, the maximum value of M could be defined, based on (3.34). After rounding the obtained value down to the power of 2, the maximum M equal to 2048 is obtained.

For $f_s = 100$ MHz, the size of the resolution element in the range direction is 3 m. In the calculation of $\Delta t_{element}$, the maximum velocity of the use case considered should be used.

In use case B, $\Delta t_{element} = 50$ ms. To define the number of samples in one RP-OTFS frame, we assume that the time duration of the OTFS frame in (3.35) should be at least ten times smaller than $\Delta t_{element}$. Thus, the number of samples in one OTFS frame in use case B is equal to 500000. Rounding this value down to the nearest power of two, one obtains $MN = 262144$. The final step is to choose concrete values of M and N. Based on considerations about computational complexity, discussed before, and on the maximum value M calculated in the example, we get $M = 2048$, $N = 128$. The values of the OTFS parameters, together with the resolution values, calculated for the three considered use cases A, B, and C, are presented in Table 3.2.

Table 3.3: The parameter of the RP-OTFS-based radar (70 GHz, BW 100 MHz, $L = \frac{M}{4}$)

Speed	N	M	**Velocity [m/s]**		**Range [m]**	
			Resol.	Max/Min	Resol.	Max/Min
A	128	512	2.65	± 170	3	384
B	128	2048	0.47	± 30	3	1534
C	128	65536	0.01	± 0.64	3	49152

Chapter 4

Results from Practical Experiments Results and Simulations

In this chapter, the results of a practical experiment and simulations of the RP-OTFS based transmission in various scenarios are presented. Both aspects of the ISAC system are investigated: telecommunications and radar. First, results from field tests are discussed since, thanks to them, simulation conditions were set appropriately.

Initially, OTFS signal simulations were carried out using models and prototype programs provided in [36]. Based on them, our own framework for OTFS testing (including the RP-OTFS) was developed. It is important to note that from release R2024a, MATLAB includes an OTFS demonstration program (`https://www.mathworks.com/help/comm/ug/otfs-modulation.html`); however, it is highly limited and does not account for fractional reflections (at least in the most recent version R2025a).

4.1 Results from Field Tests

The trials were carried out in the spirit of the short-range system, allowing the detection of the object in the bistatic range of less than 1 km. The objective of the experiment was to validate both the telecommunication and the sensing subsystems, as well as to decode bits and detect objects. That is, the signal was transmitted as in a classical wireless system to exchange data between the transmitter and the receiver, and simultaneously the CSI was calculated, allowing a moving object to be detected.

The block diagram of the experiment is shown in Figure 4.1.

The predefined pseudo-random data stream was generated offline in MATLAB. The RP-OTFS test signal was prepared so that the DD matrix had dimensions $M = 256$, $N = 64$. 4-QAM modulation was used. The offline generated data sequence contained a number of samples equivalent to one second of a continuous, non-repetitive signal sampled at 20 MHz. The transmitter and receiver consisted of a National Instruments USRP 2953R SDR equipped with two UBX-160 daughterboards and were synchronized through the GPS-disciplined oscillator. The signal was then passed to a high-power amplifier and transmitted by an antenna with a beam width of approximately 16 degrees in both azimuth and horizontal dimensions and a directivity of approximately 19 dBi. The ISAC experiment specification is given in Table 4.1.

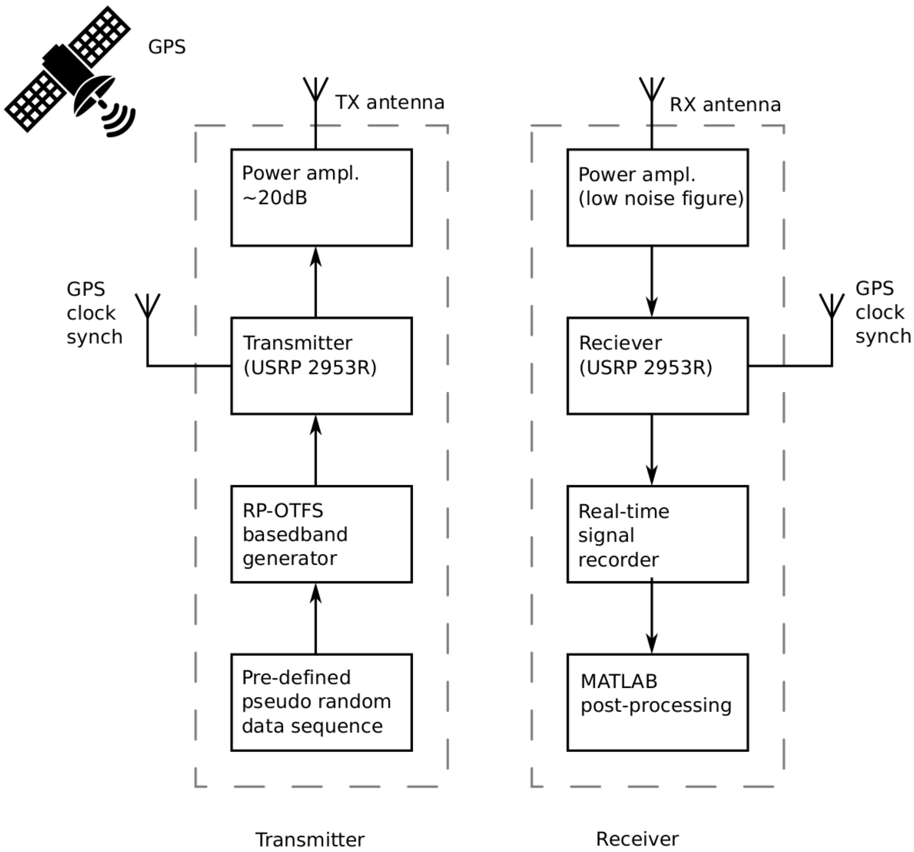

Figure 4.1: The block diagram of the data processing during the experiment.

The geometry of the measurement can be seen in Figure 4.2. The tests were carried out at the campus of the Warsaw University of Technology, Poland. The objects used in this study were vehicles that were moving along a street oriented at an angle of approximately 50 degrees relative to the transmitter–receiver line. The street is fairly busy, with a maximum speed limit of 80 km/h, however, due to the presence of a junction near the experimental area, the actual vehicle speeds during the daytime are typically much lower. The propagation of the signal along part of the street was obstructed by a large building.

The transmitter was placed around 20 m above ground level, ensuring illumination of the area of interest (road). The receiver was placed in the parking lot at a range of about 50 m from the transmitter in the illuminated sector. The transmitter-object range was ca. 180 m, and the object-receiver range was ca. 110 m. The total bistatic range [23] can be assumed to be 240 m. The ISAC receiver acquired the signal after passing through a set of low-noise amplifiers and bandpass filters between the antenna and the SDR. The amplifier gain was 20 dB. The signal reflected from objects of interest (mainly moving cars) reached the receiver and was digitized, stored, and processed offline.

The CIR-based approach for sensing was used during the experiment. Thus, on the receiver side mainly only one antenna was used. However, for future validation during offline processing of the experimental results, an additional reference antenna was used in the receiver (it is not shown in Figure 4.1, as it was not involved in the main experiment). Data from the reference antenna were also recorded. In fact, it can be stated that the sensing tests were performed simultaneously using two approaches; however, the CAF-based approach was employed solely to verify the results obtained with the CIR-based approach.

Table 4.1: In-field ISAC experiment specification

Parameter	**Value**	**Comments**
M	256	Number of samples in delay direction
N	64	Number of samples in Doppler direction
L	64	Pilot length without cyclic prefix
Modulation	4-QAM	Type of carrier modulation
f_c	5.8 [GHz]	Carrier frequency
B	20 [MHz]	Bandwidth of the signal
Br	20 [Mb/s]	Maximum data transmission bit rate
T_i	200 [ms]	Integration time of the radar sub-system
ΔR	15 [m]	Radar bistatic range resolution
ΔV	0.26 [m/s]	Radar bistatic radar velocity resolution
β	16 [°]	Beam width in both azimuth and elevation dimensions
G_{tx}/G_{rx}	19 [dBi]	Antenna gain
P_{tx}	30 [dBm]	Max transmit power

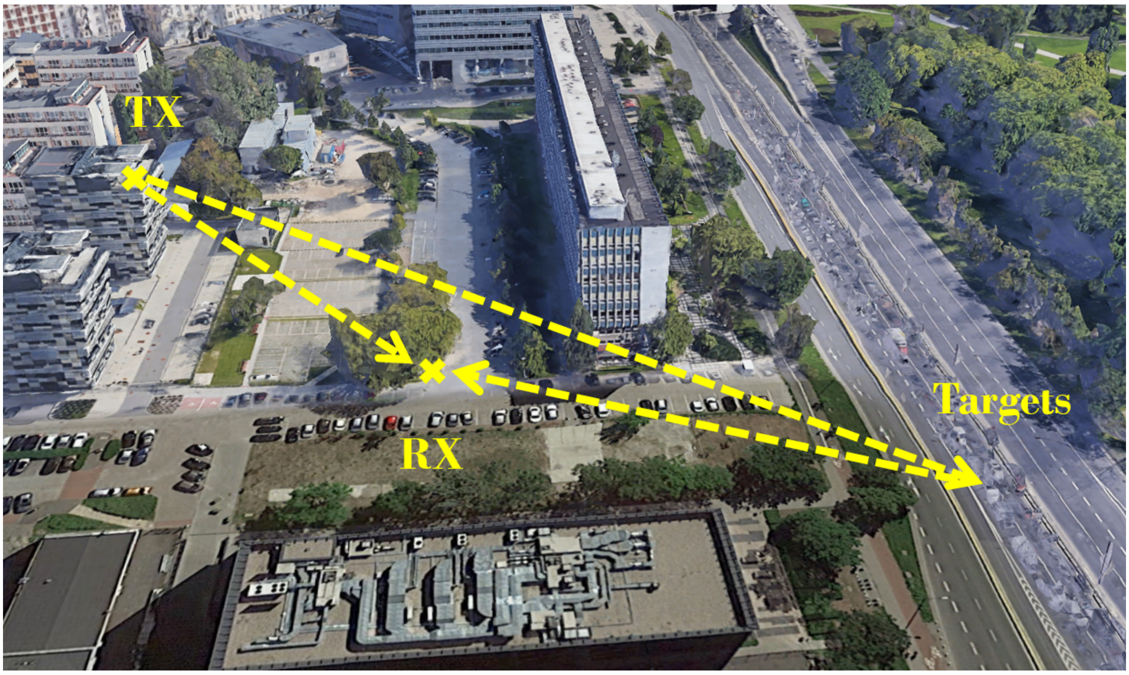

Figure 4.2: Setup of the ISAC experiment.

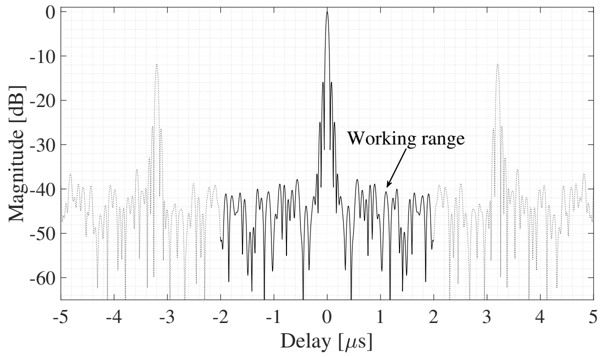

(a) Cross-section for the AF at zero Doppler shift.

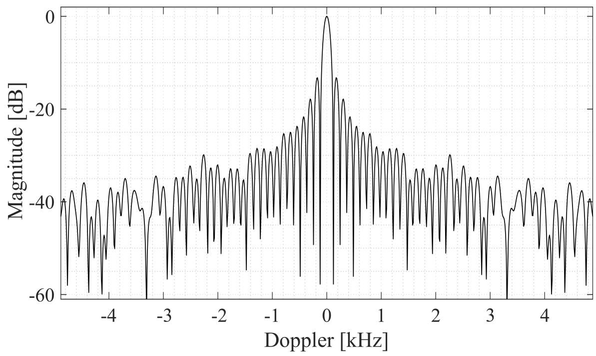

(b) Cross-section for the AF at zero delay.

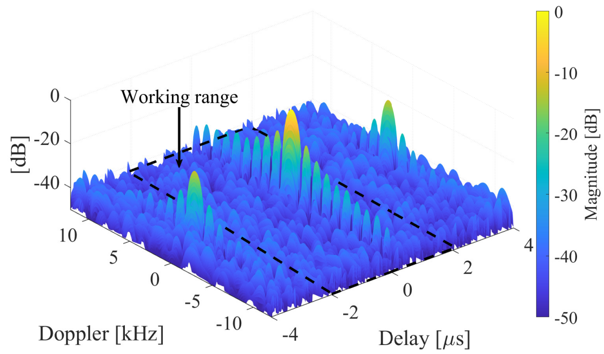

(c) AF of the RP-OTFS waveform.

Figure 4.3: Results from the **radar sub-system**: application of RP-OTFS waveform for moving car detection using Ambiguity Function (AF).

Figure 4.3 illustrates the ambiguity function of the investigated signal, shown as an example without pilot repetition along the Doppler axis of the DD grid (this method of interference power redistribution was discussed in 3.1.5 subsection). As evident in the subfigures 4.3a and 4.3c, the presence of a cyclic prefix in the OFDM-based pilot symbols, used in RP-OTFS, leads to the emergence of unwanted peaks, often referred to as ghosts. Although the amplitude of the peaks from the repeated parts of the signal is more than 10 dB lower than the main peak, they can still lead to false detections, especially in scenarios with a large number of objects exhibiting different motion parameters or, for example, in configurations with multiple transmitters operating on the same frequency (as is possible in DVB-T2) [62]. This phenomenon considerably constrains the unambiguous object detection interval. Despite the presence of peaks, the ambiguity function of the RP-OTFS signal exhibits fairly good characteristics, with the noise level being approximately 40 dB below the main peak. The comb-like structure with sidelobes of around 13 dB at zero Doppler can be attributed to the use of a time-limited signal with a rectangular window in the simulation of the ambiguity function.

Figures 4.4 and 4.5 illustrate the results of the experiments, pertaining to the communication and radar subsystems, respectively. During post-processing, signal synchronization was initially performed by identifying the peak of the correlation function between the transmitted and received signals. This was followed by estimation of the channel impulse response and bit detection using the LMMSE approach. For simplicity, the communication subsystem did not incorporate any error correction mechanisms. The

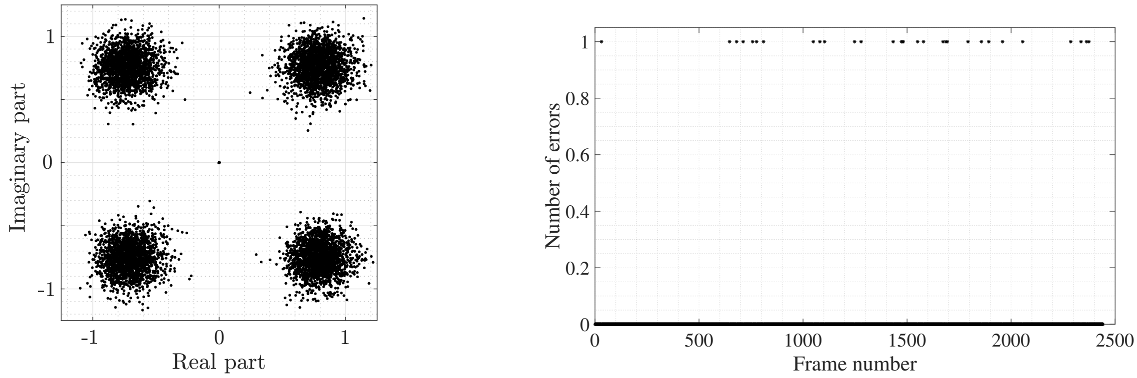

(a) Demodulated IQ constellation

(b) Errors per RP-OTFS frame

Figure 4.4: Results from **communication sub-system**: correct channel estimation and equalization result in a clear IQ constellation and low frame error rate.

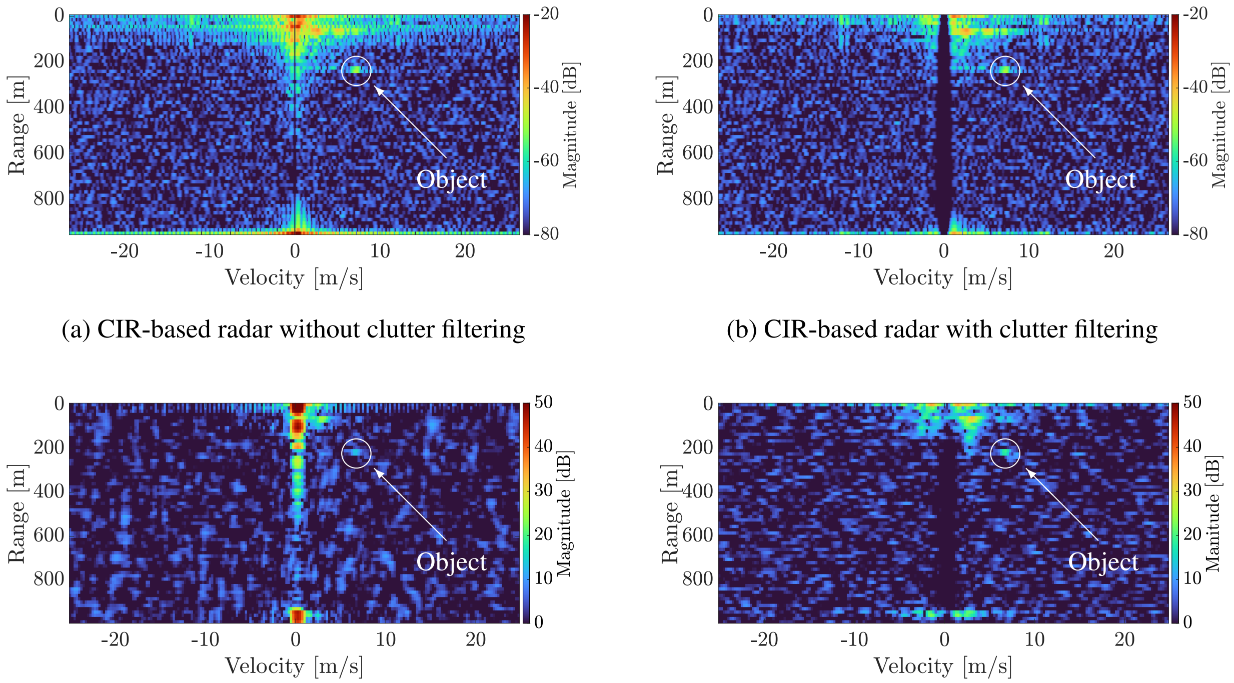

(a) CIR-based radar without clutter filtering

(b) CIR-based radar with clutter filtering

(c) CAF-based radar without clutter filtering

(d) CAF-based radar with clutter filtering

Figure 4.5: Measurement results. The moving object (car) is visible at $R_b = 240$ m and $V_b = 7.24$ m/s.

algorithms used for channel estimation and equalization were described in detail in the preceding sections. Finally, in Figure 4.4a, the constellation of demodulated signals from the reference antenna (the antenna pointing toward the receiver) is presented. The demodulated signal constellation of the signal from the main (surveillance) antenna (the antenna pointed toward the area of radar interest, and away from the receiver) is presented in Figure 4.4a. In the case of the reference antenna, the LOS signal path results in perfect radio conditions, and the 4-QAM constellation points are very well separated, one can expect that the bit error rate (BER) is very low. In the experiment, the error was minimal: no error or only one bit per RP-OTFS frame, giving the BER at $10-7$. Performance was notably worse when the main antenna was used, as the telecommunication signal was received close to the null of its radiation pattern, resulting in substantial signal attenuation. As a result, the BER at this antenna was 0.06. The use of a narrow beam antenna was necessary to enable comparison of radar detection results with the classical CAF-based approach. As mentioned earlier, the CAF architecture requires two independent reception channels: a reference channel and a surveillance channel — that are highly isolated from each other. In contrast, this requirement is not present in CIR-based systems. Therefore, antennas with wider beam patterns, capable of simultaneously receiving both radar and communication signals, can be employed.

The second system's task, namely the detection of moving objects, was performed in the next step. In the radar results discussion part, the DD grid is replaced by the range–velocity (RV) representation, which conveys the same information. However, in the RV domain, delay and Doppler frequency are expressed in the International System of Units (SI). RV maps without and after ECA-CD-based clutter removal [83] depicted in Figures 4.5a and 4.5b were obtained based on the spectral analysis performed on 128 frames (8192 samples per CIR tap - 128 frames with N = 64 samples). As can be seen, a moving object in the range of 240 m with a velocity of approximately 7.24 m/s is apparent. After applying the Aboutanios-Ye method [84] for a more accurate frequency estimation, the value 7.206 m/s was obtained, although the true data is unknown since real-world traffic was monitored. The echo originates from cars moving on the road, as the ISAC system observes. In addition, a few more objects can be seen in the range of 50 m, resulting from traffic in the illuminated parking lot. The detection results coincide with the results obtained using the classical bistatic radar processing based on the CAF calculation. In the experiment, the integration time was 105 ms, which corresponds to the signal length used in the CIR-based method. The results of the CAF-based radar processing are shown in Figures 4.5c and 4.5d (before and after additional clutter filtering using a lattice filter, respectively). These results exhibit cohesion with the CIR-based approach, as both allow object detection in the same range and velocity. For the CIR-based method by combining frames, the output SNR value of the detection peak is equal to 27.8 dB. In the reference CAF-based method, it equals 18.6 dB.

The observed discrepancy in performance may not be immediately apparent. However, it is important to note that, in the CAF-based approach, the reference signal is acquired over the air and has an unknown structure from the ISAC receiver's perspective, making it susceptible to channel-induced distortions. In contrast, the CIR-based approach utilizes a priori known reference signals (e.g. pilot sequences) that are available to the receiver before transmission. A natural extension of the CIR-based approach in this context would involve complete demodulation of the received signal and its subsequent use as a reference.

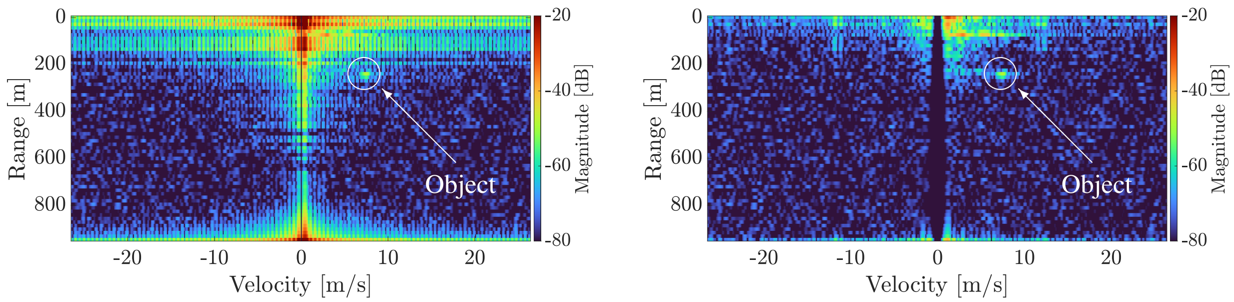

(a) RV map without ECA clutter removal.

(b) RV map with ECA clutter removal.

Figure 4.6: Measurement results obtained for large time and frequency synchronization errors for CIR-based radar.

A rather subtle but important distinction exists between the two approaches to object detection in ISAC systems. In the CIR-based approach, synchronization is performed at the receiver by estimating the parameters of the received signal. This estimation may have errors, particularly in the case of low input SNR conditions. In contrast, the CAF-based approach achieves implicit synchronization, as the system utilizes two antennas that receive the "physical" analog signal rather than its digital copy.

To investigate the robustness of the methods, an additional experiment involving intentional receiver desynchronization was conducted. The received signal was randomly desynchronized by several samples in both the time (delay) and frequency (Doppler) domains. The consequences of the wrong TF synchronization in the CIR-based radar are shown in Figure 4.6. Before further processing, the received signal was first shifted relative to the RV sampling grid, that is, in time and frequency. As observed from the resulting RV grid, the signal desynchronization concerning the RV grid results in severe smearing of the RV map, especially in regions with strong clutter components (compare Figure 4.5a with Figure 4.6a). However, the application of the ECA-CD clutter cancellation algorithm [83] can remedy this problem, as presented in Figure 4.6b.

4.2 Results of Simulations

4.2.1 Sinc Extrapolation-Based Data-to-Data Interference Reduction

At the very beginning of the simulation subsection, we present our sinc extrapolation-based interference reduction results, based on (3.23). For the test, we used the regular RP-OTFS, i.e. without repetition of pilot carriers, but all of the data zone carriers of the DD grid were inactive, i.e. filled with zeros.

We simulated the propagation of the OTFS signal through the channel with fractional delays, as described in Section 3.2.1. After that, we estimated the channel and extrapolated it with the sinc function. The initial signal was transmitted through the reconstructed channel for the second time. And finally, two signals (one was transmitted through the original channel and the other was transmitted through reconstructed channel) were subtracted from each other. The simulation was repeated several times for different input SNR. The data zone of the grid (initially filled with zeros) was used to estimate the magnitude of the remaining interference.

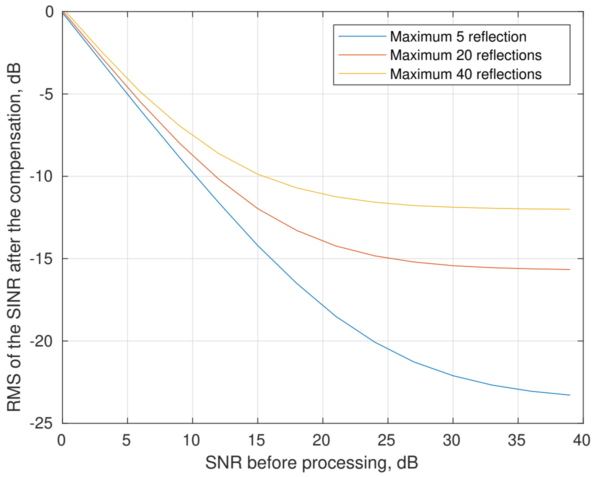

Figure 4.7: The efficiency of the data-to-data interference compensation in regular RP-OTFS without pilot repetition for different numbers of maximum reflections.

The objective of the simulation was to evaluate the dependence of the RMS of the difference in resulting signals from two channels on the SNR of the signal before applying the channel, for different numbers of reflections. The reflection coefficient had a normal distribution with the same variance as active data cells, delays had a uniform distribution in the range of $0..L-2$, the Doppler was also distributed uniformly in the range of $-0.3 \cdot N...0.3 \cdot N$. The other parameters of the grid had the following values: $M = 32, N = 128, L = 8$. The results of the simulation are shown in Figure 4.7.

It is clearly seen in Figure 4.7 that for a high SNR the sinc extrapolation-based interference reduction algorithm becomes saturated, which results from the estimation error of the sinc function parameter. Also, in the algorithm we use, we assume that the fractional part of the delay equals 0.5 (coefficient 0.5 in (3.23)), which is also a source of inaccuracy. We do not know the real delay, so we choose the value in the middle of the possible fractional delay interval $(0...1)$.

In the next and all following simulations of the communication subsystem, we will evaluate the performance with BER characteristic for different application scenarios to estimate the performance of the different waveforms. The OTFS parameters (common for RP and ZP) are given in Table 4.2. M and N were reduced to speed up the simulation.

Table 4.2: Values of simulation parameters

Parameter	**Value**	**Description**
Modulation	4-QAM	Type of carrier modulation
f_c	70 GHz	Carrier frequency
f_s	100 MSPS	Sampling rate
M	32	No of samples in delay direction
N	16	No of samples in Doppler direction
L	8	Number of pilot samples

It is assumed that there is only one path with zero Doppler and there are 10 randomly scattered fractional reflections. The zero Doppler path is assumed to be the main propagation path and all levels for the reflections are refereed to it. Also, we assume that the receiver is perfectly synchronized to the main propagation path. In this scenario, we fix the number of reflections, but the variance of the magnitudes of the CIR coefficients was not constant. The simulation was carried out for three variances: -18 dB, -24 dB, and -30 dB (relatively to the power level of the main propagation path). There was no sufficient difference in the OFDM performance results, so we put only one BER curve for OFDM with its best results. The CIR coefficients have a normal distribution and zero mean. The delays and Doppler are uniformly distributed in the same range as in the previous case. No pilot repetition was applied.

The results of the simulation without and with the data-to-data interference reduction (sinc extrapolation algorithm) are presented in Figures 4.8a and 4.8b, respectively.

In the figures, one can see that OFDM is inefficient in such a strong Doppler environment. Also, regular RP-OTFS outperforms ZP-OTFS in case of low SNRs, but for higher SNRs, interference compensation is needed for regular RP-OTFS to outperform ZP-OTFS. In case of lower SNRs, the dominant source of errors is noise, and since RP-OTFS has more active carriers, it is more efficient despite the greater interference from the pilot zone. As the SNR increases, the interference becomes the dominating factor that determines the efficiency of the system. The interference compensation is not as efficient in the case of ZP-OTFS as it has less power in the pilot zone. One of the obvious solutions could be to increase the power of the ZP-OTFS pilot to the level of the regular RP-OTFS pilot zone. However, this will lead to an extremely high peak-to-average ratio, which in turn will make the transmission in real systems extremely difficult.

4.2.2 Repetition-Based Pilot-to-Data Interference Reduction

In this simulation scenario, sinc extrapolation-based data-to-data interference compensation is always enabled, and we compare only the system performance with and without pilot-to-data interference compensation (by the introduced pilot repetition in the Doppler direction of the DD grid), proposed in Section 3.1.5 and graphically explained in Figure 3.9.

At present, we simulate a strong clutter reflection. We use Doppler reflection parameters the same as in the simulations from the previous subsection, but pick only one magnitude -18 dB. However, we also add a strong reflection on zero Doppler, the magnitude of the reflection being -3 dB. The magnitudes of Doppler reflections are normalized to the main LoS propagation path. The maximum delay of the clutter reflections does not exceed $L - 2$. Here, it is important to notice that for moving transmitter or receiver, the reflections from static object will also have Doppler. For this case, the parameters of the pilot repetitions K and i should be chosen to exclude the influence of these strong reflections in the DD domain. In the cases where pilot repetition was enabled, the column of the DD grid where the interferences were concentrated was excluded from processing, for both types of signal ZP-OTFS and RP-OTFS. This scenario is intended to simulate the case of interference between MTs described in Section 3.1.5.

The results of the simulation are shown in Figure 4.9 and are denoted as "with pilot repetition" and "without pilot repetition", respectively. In the case of strong reflections the fractional delay oscillations significantly reduce the performance, even in cases where sinc extrapolation is enabled. The additional

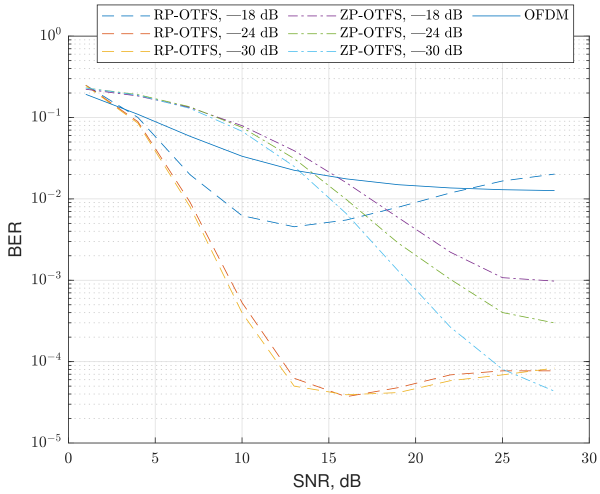

(a) BER for channels with 10 reflections for different modulation types and channel coefficient variances **without** sinc extrapolation based data-to-data interference compensation. The type of modulation and variance of the channel coefficients are indicated in the legend of the Figure.

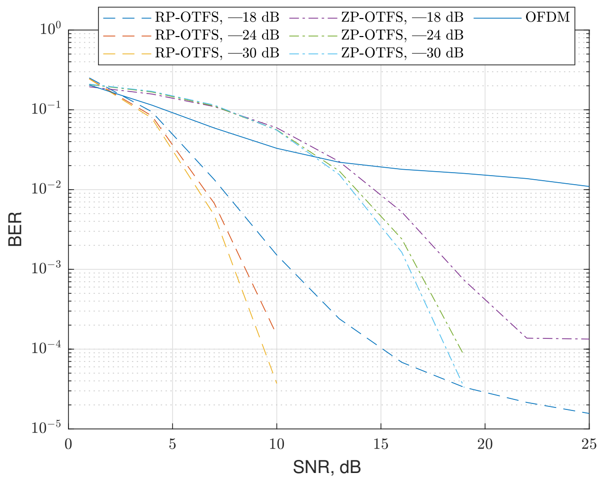

(b) BER for channels with 10 reflections for different modulation types and channel coefficient variances **with** sinc extrapolation based data-to-data interference compensation. The type of modulation and variance of the channel coefficients are indicated in the legend of the Figure.

Figure 4.8: Comparison of BER performance for channels with 10 reflections **with and without sinc extrapolation** based data-to-data interference compensation.

pilot-to-data interference compensation technique allows efficient elimination of pilot sidelobes in DD grid regions used by data and reduction of the BER. In the case of ZP-OTFS, the performance gain from pilot repetition is due to the removal from processing the column where the interference is concentrated, as stated in the experiment description.

4.2.3 Interpolation of the Instantaneous CIR Estimation

To verify the assumptions about the interpolating algorithms that were made during the discussion of the RP-OTFS receiver, simulations of different interpolating algorithms were performed.

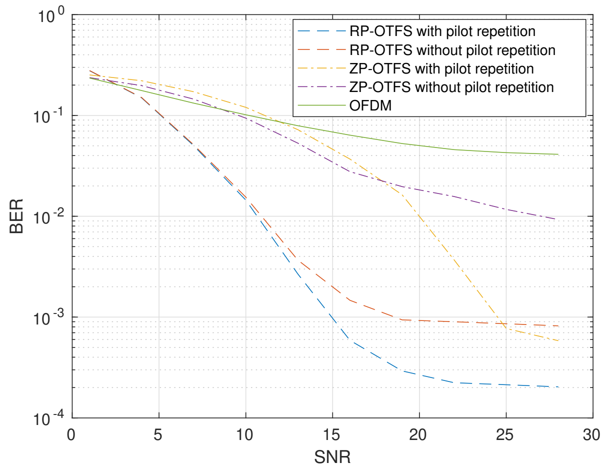

Figure 4.9: BER for channels with 10 reflections and strong reflection on zero Doppler with enabled and disabled the proposed pilot-to-data interference compensation technique.

For this test, the high-speed train (HST) model [12] with a velocity of 500 km/h was used; the size of the Doppler delay grid was $M = 64$, $L = 4$, $N = 16$. We simulated relatively short pulse characteristics of the channels: 3 taps only. The carrier frequency was 7.1 GHz – this is the maximum carrier frequency in frequency range 1 of 5G. The sampling rate of 20 MSPS and the subcarrier spacing (for OFDM baseline results) of 15 kHz were used. Two types of modulation (QAM-4 and QAM-16) were also tested to investigate modulation dependence. An OFDM signal with 56 carriers and an 8-samples-long cyclic prefix was added to the simulation as a reference to compare performance with it. The parameters of the high-speed train scenario are given in Table 4.3. In order to show the dependency of BER from velocity for different interpolation methods, we performed one more simulation for QAM-16 and a maximum train speed of 250 km/h.

Table 4.3: Parameters of performed high-speed train simulation

Parameter	**Value**	**Comments**
D_s	2000 [m]	$D_s/2$ initial distance
D_{min}	100 [m]	Distance from TX to track
v	250, 500 [km/h]	Speed of the train

The channel was initially estimated and then equalized. The simulation results for the 500 km/h train speed are shown in Figures 4.10a and 4.10b, for 250 km/h in Figure 4.10c. It is observed that the OTFS performs much better than the OFDM. The better OTFS performance for the HST channel can be explained by the fact that, in the case of HST, we have only one strong Doppler reflection. As a result, the channel only causes pilot rotation in the complex plane with some Doppler frequency without much interference. In this test, no interference reduction techniques were used. Until the criteria of the Nyquist sampling theorem are met, this rotation can be easily reconstructed and compensated for.

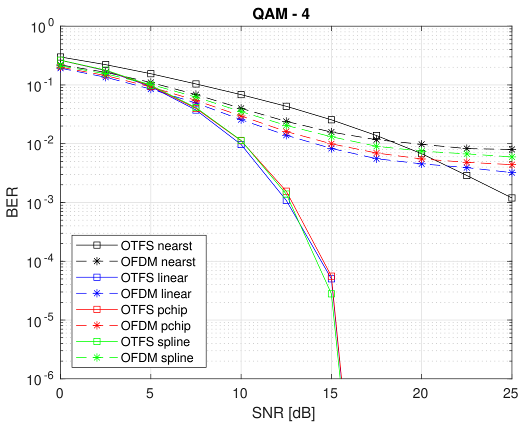

(a) Modulation QAM-4. Velocity 500 km/h

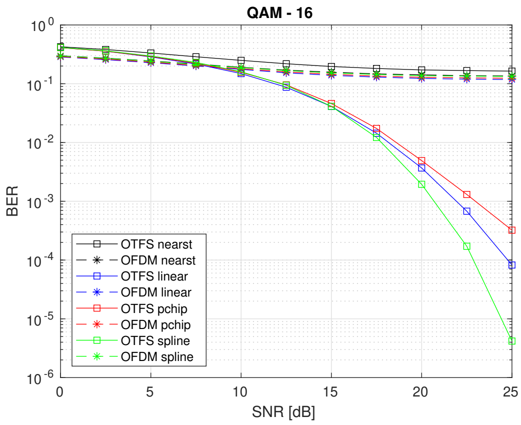

(b) Modulation QAM-16. Velocity 500 km/h

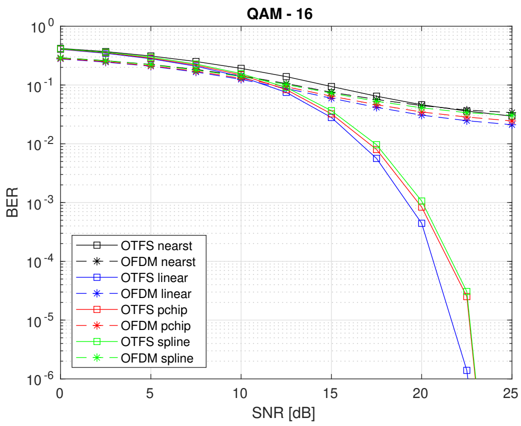

(c) Modulation QAM-16. Velocity 250 km/h

Figure 4.10: BER for unknown, estimated and corrected mobile 3GPP HST channel for different channel interpolation methods and modulations. RP-OTFS without sinc extrapolation and pilot repetition is used. OFDM is for reference.

Another conclusion from the simulation is that even simple low-cost interpolation schemes can be used in the RP-OTFS-based data transmission, which makes its real-time application/implementation easier.

4.2.4 Sensing Performance Simulation

We begin the evaluation of the radar subsystem by simulation of the potential processing gain for different types of OTFS. The simulation was provided for two types of RP-OTFS with and without pilot repetition for $L = M/4$ for different grid sizes: 64×16 and 32×8. The purpose of the simulation is to test the hypothesis that pilot repetitions do not impact the gain in the radar subsystem processing. ZP-OTFS results were added here as a baseline.

As the data transmission is not taken into account in CSI based approach, only pilots are used for object detection, we defined input SNR as the ratio of the average power of active pilot carriers (for both cases ZP-OTFS and RP-OTFS) to noise on the input of the receiver here. During simulation, the channel was modeled as a single echo source with a random delay in the range 0 to L and varying signal-to-noise ratios. The output SNR in the context of current simulation is the average power of the detected peak compared to the average power in the DD grid cells without any objects.

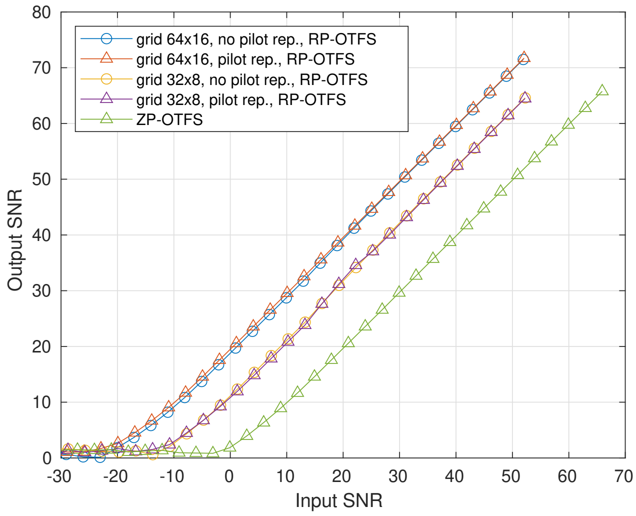

Figure 4.11: SNR_{out} as a function of SNR_{in} for different modulation techniques.

The results obtained are presented in Figure 4.11. As expected, the ZP-OTFS has no processing gain, and the processing gain of the RP-OTFS depends on the number of pilot carriers and does not depend on pilot repetition.

In the next scenario, the probability of the right detection was simulated depending on SNR_{in}, for a constant false alarm rate 10^{-4} and for different pilot lengths L and different object velocities. The simulation parameters are in Table 4.4.

OFDM and RP-OTFS had the same number of pilots for a fair comparison. In the simulation, we took into account the interferences between carriers. The ZP-OTFS was used as the baseline for our simulations. Performance in the case of ZP-OTFS does not depend on the velocity of the object. In this simulation, we do not take into account the cell migration of the object.

It is clearly seen from the simulation results (Figure 4.12) that RP-OTFS outperforms the ZP-OTFS and OFDM waveforms. The RP-OTFS requires the lowest input SNR to maintain the desired probability of detection.

Table 4.4: Detection probability simulation parameters

Parameter	**Value**	**Comments**
M	512	Number of samples in delay direction
N	128	Number of samples in Doppler direction
L	8,32	Number of pilot subcarriers
f_c	70 [GHz]	Carrier frequency
Br	20 [Mb/s]	Maximum data transmission bitrate
P_{fa}	10^{-4}	Probability of false alarm
v	2,30,230	Velocities of the object

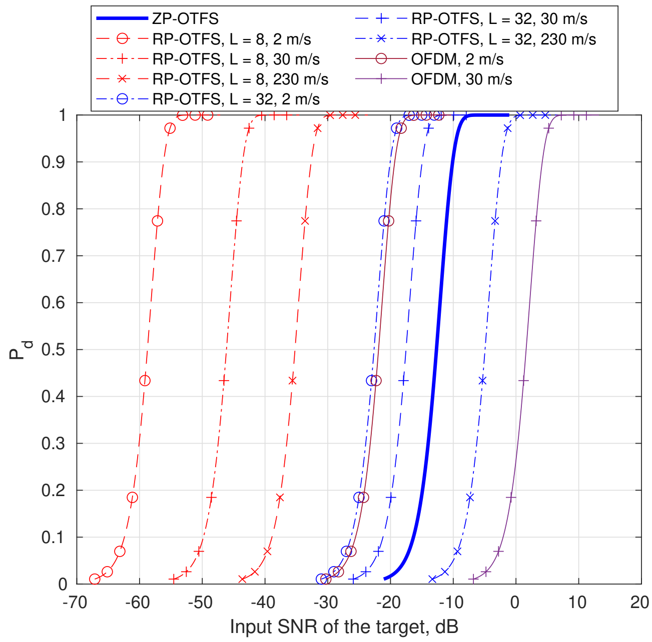

Figure 4.12: The detection probability in case of constant false alarm. RP-OTFS without sinc extrapolation and pilot repetition is used. $N = 128$.

In the absence of Doppler frequency shift, coherent combining of multiple pilot subcarriers provides a theoretical processing gain that increases linearly with the number of pilots, resulting in a significant enhancement of detection performance. However, when Doppler shifts are present, the orthogonality of OFDM subcarriers is disrupted, and ICI is introduced. This interference behaves as a noise-like component that scales with the signal power and does not vanish under averaging. As a result, while noise can be effectively suppressed through coherent combining, the contribution of ICI imposes a hard ceiling on the achievable post-combining SINR. The SINR, therefore, exhibits an initial growth with the number of coherently combined pilots, but eventually saturates at a value determined solely by the Doppler-induced interference level. This effect fundamentally limits the coherent processing gain of OFDM-based sensing and communication systems. From a radar perspective, it constrains the maximum detection probability attainable for a given false-alarm rate, independent of the number of integrated subcarriers. From a communications viewpoint, it highlights the trade-off between spectral efficiency and robustness to mobility. Overall, Doppler acts not only as a fading mechanism but also as a structural barrier to unlimited coherent integration gain in multicarrier integrated sensing and communications.

Three important observations can be made from Figure 4.12. First, as the length of the RP-OTFS pilot signals increases, the detection performance degrades significantly, mainly due to ICI. Second, under the conditions of these simulations, OFDM does not benefit from increasing the number of pilots, since ICI dominates the SINR; as noted above, adding more pilots in this regime does not improve SINR. Reducing the interference in this scenario would require decreasing the number of subcarriers, i.e., shortening the length of the OFDM symbol, which is not permissible given the constraints of the experiment. Finally, for a object velocity of 230 m/s, the Doppler shift becomes sufficiently large that such objects cannot be reliably detected using OFDM pilots.

4.2.5 Sensing System Level Simulations

To validate the performance of the ISAC RP-OTFS-based system, system-level simulations of its radar subsystem were also performed. A conventional OFDM system was used as the baseline for the simulations.

The simulation results for four different scenarios are presented below. In all scenarios, a single transmitter and a single receiver were used. Depending on the scenario, the number of moving objects varied from one to three. In model we set the power of the echo signal from the object to the level that corresponds to -10 dB SNR at the receiver input. In addition to moving objects, 200 static objects with random coordinates were included in the analysis area.

The RP-OTFS (or OFDM) signal is transmitted from the transmitter (base station, BS) to the receiver (mobile terminal, MT). On the receiver side, it is assumed that the received signal is perfectly synchronized. Based on the pilot signals, the receiver estimates the CSI and makes decisions regarding the presence or absence of objects. Subsequently, this information about the objects can be utilized locally by the receiver and transmitted to the BS through the uplink channel. The receiver used the LMMSE algorithm to estimate the CSI.

The carrier frequency was 30 GHz, OFDM symbol length 2048 samples at 50 MSPS. The duration of the RP-OTFS pilot is $L = 32$, the OTFS sample rate was the same as for OFDM. The plots below (Figures 4.13- 4.16) are based on a coherent combining of 24 OFDM frames (or $(24 \times 2048/32 = 1536$ RP-OTFS frames). The transmitter antenna was omnidirectional. In the receiver side antenna array with two elements was used, the antenna array was steered to focus the beam toward the moving objects. Each set of output data consists of 3 figures:

- The scenario visualization (index (a)). In this figure, the mutual positions of the transmitter, receiver, and object are shown. The arrow near the object mark (red cross) also shows the direction of movement. The blue points show the positions of the static scatters. The BS (green) and MT (pink) marks have an arrow that shows the normal to its antenna.

- The RP-OTFS simulation results (index (b)). In this figure the amplitude (in dB) of the echos with Doppler are shown in a Cartesian coordinate system for RP-OTFS simulation. The red cross on the pictures shows the actual object position. The detector was out of the scope of this simulation. The target position was determined based on (2.48) and the beampattern of the antenna array.

- The OFDM simulation results (index (c)). In this figure the amplitude (in dB) of the echos with Doppler are shown in a Cartesian coordinate system for OFDM simulation. The red cross on the pictures shows the actual object position. The detector was out of the scope of this simulation. The target position was determined based on (2.48) and the beampattern of the antenna array.

In the following part of this subsection, we will describe the details of different scenarios and discuss the results.

Scenario 1

In this scenario, the object is located on a straight line in front of BS and MT (Figure 4.13). The object velocity was 19.2 m/s, the object moves practically towards the MT and BS. Such movement characteristics generates practically maximum Doppler frequency offset at the receiver from the bistatic geometry point of view. However, despite the fact that the bistatic angle is equal to zero, which creates favorable conditions for radar operation ($\beta = 0$, hence $\cos(\beta/2) = 1$, see (2.49)), the velocity vector of the object deviates from the transmitter-receiver line by approximately 30 °, which slightly reduces the Doppler shift multiplying it by a factor of $\cos(30°) = 0.86$.

It is clearly seen in Figure 4.13b that detection could be easily done with RP-OTFS (SINR around 30 dB), but in the case of OFDM (Figure 4.13c) due to ICI the channel estimation was corrupted. Due to the low bistatic angle, relatively small angle of the velocity vector, high velocity and high carrier frequency the Doppler is too high to handle with a relatively long OFDM symbol. On the other hand, RP-OTFS's pilot, with a significantly shorter OFDM-based pilot, can process it.

Two additional object echos are also observed to the left and right of the transmitter–receiver line. These echos can be explained by the presence of sidelobes in the radiation pattern of the reception antenna array. As discussed in Section 2.4.2, the range and velocity resolution in bistatic radars also depend on the accuracy of the estimation of the angular coordinates.

In fact, the object can be located at any point for which the sum of the distances to the receiver and the transmitter remains constant ($R_T + R_R = const$). The determining a unique point with object from this set can be achieved through spatial filtering by the antenna system of the receiver (or transmitter), or by employing a multi-station system in which several receivers and/or transmitters simultaneously perform measurements of the same object.

Scenario 2

This scenario and the simulation results are shown in Figure 4.14. In the scenario, the mutual position of the object, BS, and MT was changed to reduce Doppler.

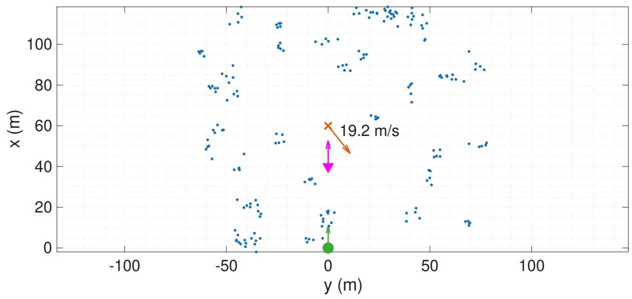

(a) The visualization of the scenario.

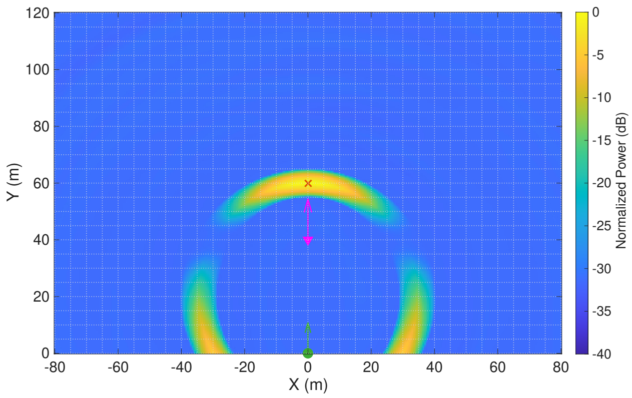

(b) The results for the RP-OTFS waveform.

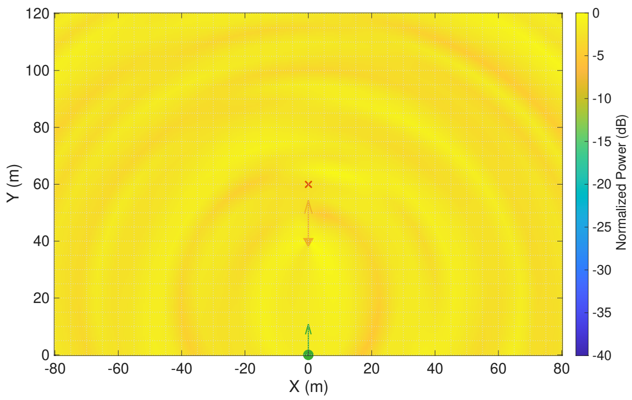

(c) The results for the OFDM waveform.

Figure 4.13: Scenario 1. MT (receiver) is located between the BS (transmitter) and receiver in front of receiver.

The velocity magnitude remains the same as in the previous scenario, at 19.2 m/s. Moreover, the velocity vector is now even closer to the bisector of the bistatic angle ($\cos(\delta) \approx 1$), which at first glance should generate the maximum Doppler shift as in Scenario 1. However, the relative positioning of the object and the ISAC system elements is chosen such that the bistatic angle becomes large. In this scenario, $\beta = 122°$ and $\cos(\beta/2) = 0.5$, which reduces the Doppler shift observed by the receiver by practically two times.

In the conclusions to this scenario, it should be noted that, in fact, the only change is the position of the receiver. This modification made it possible to reduce the Doppler shift observed at the receiver, and in the OFDM-based ISAC system, the level of ICI was also reduced, which enabled object detection. In case of

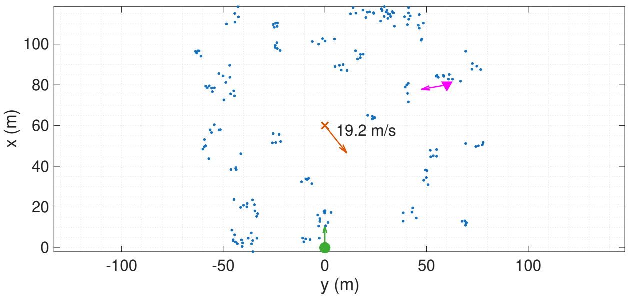

(a) The visualization of the scenario.

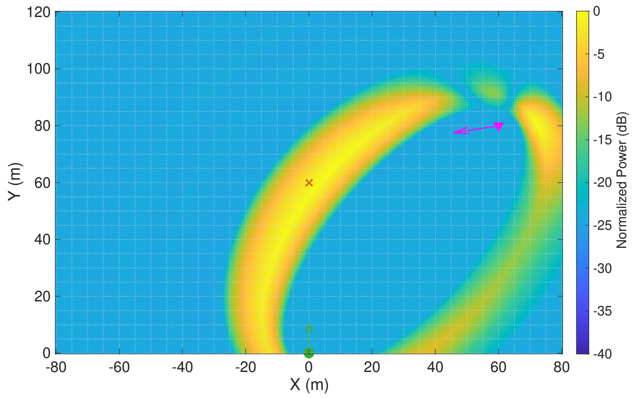

(b) The results for the RP-OTFS waveform.

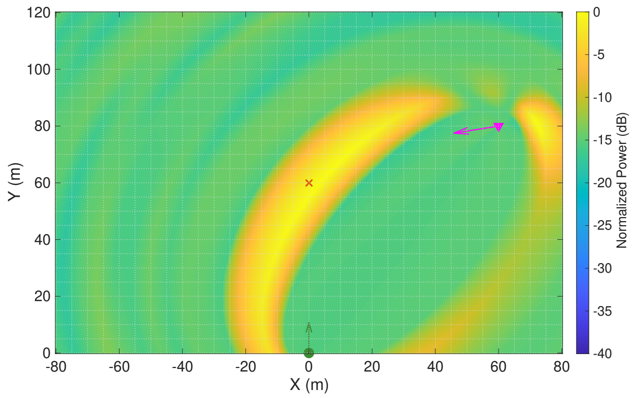

(c) The results for the OFDM waveform.

Figure 4.14: Scenario 2. The object is located between the MT and BS, but away from the baseline (the line between MT and BS). This significantly reduces Doppler frequency offset at the receiver side. Also the trace of the object become wider.

OFDM, the SINR was around 15 dB. In addition, the set of possible object locations has changed (yellow ellipse) . It is evident that the true object position will belong to both sets of possible points (from Scenario 1 and 2). By overlapping the measurements obtained in these two scenarios, it is possible to determine the true position of the object.

The increase in the bistatic angle also affects the resolution capability, which is clearly seen from the Figure 4.14c. The marks corresponding to possible object positions have become noticeably thicker compared to Scenario 1. This is consistent with the theoretical derivations presented in Subsection 2.4.2, see (2.50).

Scenario 3

This scenario and the results of the simulation are shown in Figure 4.15. In this scenario the object is located between the BS and MT.

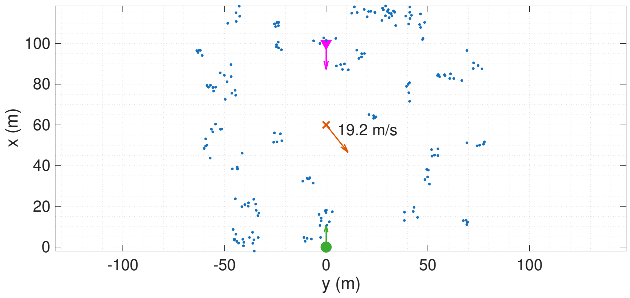

(a) The visualization of the scenario.

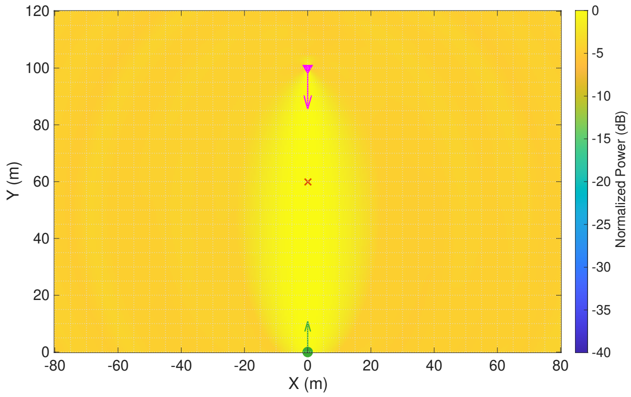

(b) The results for the RP-OTFS waveform.

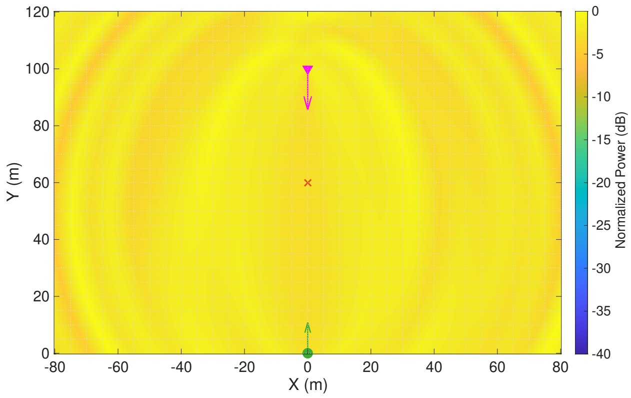

(c) The results for the OFDM waveform.

Figure 4.15: Scenario 3. The object is on the baseline between MT and BS.

The theoretical conclusions drawn in Section 2.4.2 are confirmed by the simulations. This represents a special case of ISAC system geometry in which range and velocity resolution are absent, since $\beta/2 = 90°$ and $\cos(\beta/2) = 0$. However, in this region, the so-called forward scattering occurs. Thus, while the presence of a object within this zone can be established, its coordinates cannot be measured. In fact, none of the radars (neither OFDM-based nor RP-OTFS-based) possess sufficient resolution to detect the object at this position.

Scenario 4

This scenario and the results of the simulation are shown in Figure 4.16. In this scenario, we tested the work of the ISAC system in case of multiple reflections. The object with velocity 22.4 m/s is very close to the base line between the transmitter and the receiver, but not exactly on it.

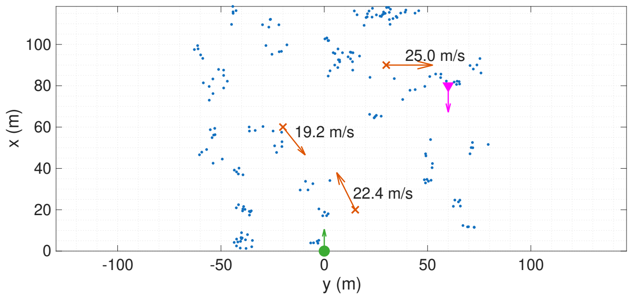

(a) The visualization of the scenario.

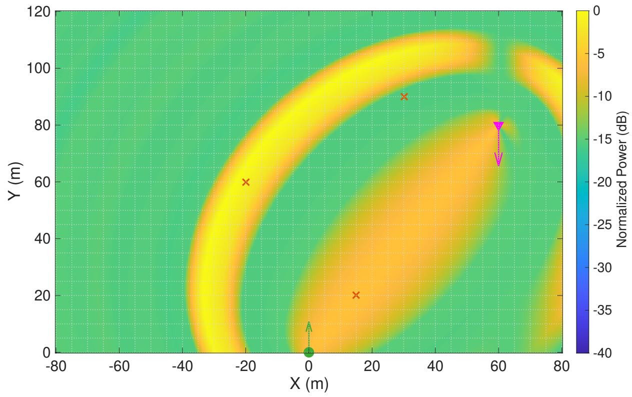

(b) The results for the RP-OTFS waveform.

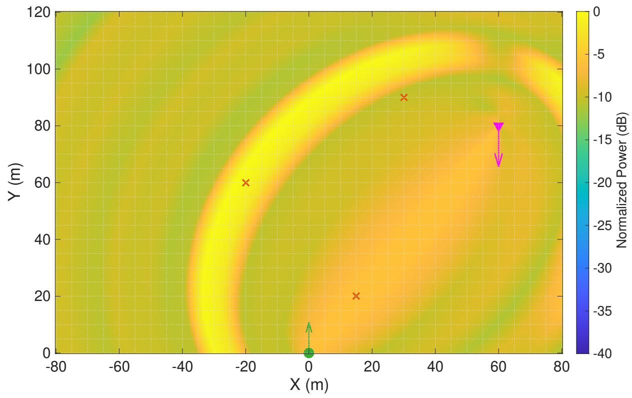

(c) The results for the OFDM waveform.

Figure 4.16: Scenario 4. Multiple objects in different position, object with 22.4 m/s move perpendicularly to the baseline, but still very close to it.

However, the most important result of this scenario is that one of the objects was not detected. The object with a velocity of 25 m/s remained undetected due to the fact that the receive antenna array consists of only two elements, which is less than the number of objects. In such a configuration, it can form only two beams, which is fewer than the number of objects with non-zero Doppler shifts. In the general case, the receiver behavior in the situation described in Scenario 4 depends on the beamforming control algorithm. In some cases, it is possible to form a beam that simultaneously covers two objects. However, this issue lies beyond the scope of the present work.

Conclusions

Based on provided scenarios, it can be concluded that the geometrical characteristics of bistatic radars, analyzed in the theoretical section, were validated through simulations. Another important conclusion is that the resolution and echo traces from the objects are not sufficient (at least in the reasonable MT antenna configuration) to track the object in a bistatic radar configuration when relying solely on a single MT, even under relatively high SINR conditions. Conversely, the shape of the object traces in the coordinate domain is determined by the relative positions of the MT, BS, and the object. These findings indicate that the use of multiple receiving points or transmitter beamforming and the joint processing of the information collected from them can substantially improve the resolution capability of ISAC-based bistatic radar systems. An important observation was done in Scenario 4 when the number of antenna elements is smaller than the number of objects, the receiver cannot generate orthogonal beams for every object. This introduces a considerable limitation on the ISAC system.

Chapter 5

Conclusions

This dissertation has addressed one of the key challenges of OTFS-based waveforms, namely the inherently low average power of pilot symbols in the most widely adopted OTFS modifications, such as ZP-OTFS, ZP-BOX, and others. By employing a more efficient utilization of subcarriers in the pilot zone, the proposed RP-OTFS scheme enables a significant increase in average pilot power, which directly improves the accuracy of channel estimation. Since in CSI-based sensing, the quality of channel estimation directly impacts both the sensing and communication subsystems, this enhancement represents a major step toward the development of reliable ISAC systems based on the OTFS modulation.

One of the main drawbacks of this solution is that this gain in average pilot power comes at the expense of removing the guard interval, which results in increased interference between pilot and data symbols. To mitigate this issue, in the dissertation, a solution based on repeated pilots was proposed. In addition, this approach can be extended to multiuser RP-OTFS systems, where it provides a mechanism for constructing orthogonal pilot structures. Furthermore, the ability of the dynamic change the location of the pilot interference in the Doppler frequency shift direction allows one to adjust the grid to different Doppler without changing processing on the receiver side.

Another fundamental challenge of OTFS in general (not limited to RP-OTFS) is the fractional reflection effect. To address this, a sinc-based extrapolation method has been introduced, derived from the system model, and validated through MATLAB-based simulations.

Performance analysis has demonstrated that RP-OTFS outperforms other OTFS-based waveforms as well as OFDM under strong Doppler conditions, both in terms of data transmission (see Figure 4.8) and in CSI-based target detection (see Figures 4.12- 4.16).

In addition, several practical experiments were conducted to validate the proposed RP-OTFS waveform, with results presented in Figures 4.3- 4.6. The dissertation has also examined channel estimation and equalization methods for RP-OTFS, with particular emphasis on classical linear receivers based on the LMMSE criterion.

Furthermore, different RP-OTFS application scenarios have been analyzed from the perspective of the sensing subsystem, and guidelines have been provided for selecting global delay Doppler grid parameters. Analytical expressions have also been derived for evaluating various characteristics of RP-OTFS, including the PARP and the dependence of pilot interference levels on Doppler spread, etc.

Together, these results confirm that RP-OTFS constitutes a promising foundation for the design of future ISAC systems, providing both theoretical contributions and practical validation.

Bibliography

[1] Gerald Matz Franz Hlawatsch. *Wireless Communications over Rapidly Time-Varing Channels*. Elsevier, 2011.

[2] William A. Holm Mark A. Richards, James A. Scheer. *Principles of Modern Radar*. Scitech Publishing, 2010.

[3] Daniel W. O'Hagan, Motlatsi Setsubi, and Stephen Paine. Signal reconstruction of dvb-t2 signals in passive radar. In *2018 IEEE Radar Conference (RadarConf18)*, pages 1111–1116, 2018.

[4] T. Thaj and E. Viterbo. Low complexity iterative rake decision feedback equalizer for zero-padded otfs systems. *IEEE Transactions on Vehicular Technology*, 69(12):15606–15622, December 2020.

[5] Harish Viswanathan and Preben E. Mogensen. Communications in the 6g era. *IEEE Access*, 8:57063–57074, 2020.

[6] H. Tataria, M. Shafi, A. F. Molisch, M. Dohler, H. Sjöland, and F. Tufvesson. 6g wireless systems: Vision, requirements, challenges, insights, and opportunities. *Proceedings of the IEEE*, 109(7):1166–1199, July 2021.

[7] Emil Björnson. Intelligent reflecting surfaces for wireless communications [globecom 2021 tutorial]. `https://www.youtube.com/watch?v=PmTjNGabrkA`.

[8] M. Honkala, D. Korpi, and J. M. J. Huttunen. Deeprx: Fully convolutional deep learning receiver. *IEEE Transactions on Wireless Communications*, 20(6):3925–3940, June 2021.

[9] T. Wild, V. Braun, and H. Viswanathan. Joint design of communication and sensing for beyond 5g and 6g systems. *IEEE Access*, 9:30845–30857, 2021.

[10] C. de Lima, D. Belot, R. Berkvens, A. Bourdoux, A. Dardari, M. Guillaud, M. Isomursu, E.-S. Lohan, Y. Miao, A. N. Barreto, M. R. K. Aziz, J. Saloranta, T. Sanguanpuak, H. Sarieddeen, G. Seco-Granados, J. Suutala, T. Svensson, M. Valkama, H. Wymeersch, and B. van Liempd. 6g white paper on localization and sensing. `http://urn.fi/urn:isbn:9789526226743`, 2020.

[11] H. Chen, H. Sarieddeen, T. Ballal, H. Wymeersch, M.-S. Alouini, and T. Y. Al-Naffouri. A tutorial on terahertz-band localization for 6g communication systems. *IEEE Communications Surveys Tutorials*, 24(3):1780–1815, 2022.

[12] User equipment (ue) radio transmission and reception; 3gpp ts 38.101-1. `https://www.3gpp.org/ftp/Specs/archive/38_series/38.101-1`.

[13] G. Barb, M. Otesteanu, F. Alexa, and F. Danuti. Ofdm multi-numerology for future 5g new radio communication systems. In *2020 International Conference on Software, Telecommunications and Computer Networks (SoftCOM)*, pages 1–3, Split, Croatia, 2020.

[14] T. Levanen, O. Tervo, K. Pajukoski, M. Renfors, and M. Valkama. Mobile communications beyond 52.6 ghz: Waveforms, numerology, and phase noise challenge. *IEEE Wireless Communications*, 28(1):128–135, February 2021.

[15] R. Hadani et al. Orthogonal time frequency space modulation. In *2017 IEEE Wireless Communications and Networking Conference (WCNC)*, pages 1–6, San Francisco, CA, USA, 2017.

[16] Y. Hong, T. Thaj, and E. Viterbo. *Delay-Doppler Communications: Principles and Applications*. Academic Press, 2022.

[17] L. Gaudio, M. Kobayashi, G. Caire, and G. Colavolpe. On the effectiveness of otfs for joint radar parameter estimation and communication. *IEEE Transactions on Wireless Communications*, 19(9):5951–5965, September 2020.

[18] P. Raviteja, K. T. Phan, Q. Jin, Y. Hong, and E. Viterbo. Low-complexity iterative detection for orthogonal time frequency space modulation. In *2018 IEEE Wireless Communications and Networking Conference (WCNC)*, pages 1–6, Barcelona, Spain, 2018.

[19] Lorenzo Gaudio, Giulio Colavolpe, and Giuseppe Caire. Otfs vs. ofdm in the presence of sparsity: A fair comparison. *IEEE Transactions on Wireless Communications*, 21(6):4410–4423, 2022.

[20] Pavel Karpovich and Tomasz P. Zielinski. Testing zero-padded otfsm with additional pilot in high doppler transmission scenarios. In *2022 Signal Processing: Algorithms, Architectures, Arrangements, and Applications (SPA)*, pages 116–121, 2022.

[21] Shuangyang Li, Jinhong Yuan, Weijie Yuan, Zhiqiang Wei, Baoming Bai, and Derrick Wing Kwan Ng. Performance analysis of coded otfs systems over high-mobility channels. *IEEE Transactions on Wireless Communications*, 20(9):6033–6048, 2021.

[22] M. I. Skolnik. *Radar Handbook*. McGraw Hill, 1990.

[23] M. Malanowski. *Signal Processing for Passive Bistatic Radar*. Artech House, 2019.

[24] P. Raviteja, K. T. Phan, and Y. Hong. Embedded pilot-aided channel estimation for otfs in delay–doppler channels. *IEEE Transactions on Vehicular Technology*, 68(5):4906–4917, May 2019.

[25] Fei Liu, Zhengdao Yuan, Qinghua Guo, Zhongyong Wang, and Peng Sun. Message passing-based structured sparse signal recovery for estimation of otfs channels with fractional doppler shifts. *IEEE Transactions on Wireless Communications*, 20(12):7773–7785, 2021.

[26] Fei Liu, Zhengdao Yuan, Qinghua Guo, Zhongyong Wang, and Peng Sun. Message passing-based structured sparse signal recovery for estimation of otfs channels with fractional doppler shifts. *IEEE Transactions on Wireless Communications*, 20(12):7773–7785, 2021.

[27] P. Karpovich and T. P. Zielinski. Random-padded otfs modulation for joint communication and radar/sensing systems. In *2022 23rd International Radar Symposium (IRS)*, pages 104–109, Gdansk, Poland, 2022.

[28] Lorenzo Gaudio, Mari Kobayashi, Giuseppe Caire, and Giulio Colavolpe. On the effectiveness of otfs for joint radar parameter estimation and communication. *IEEE Transactions on Wireless Communications*, 19(9):5951–5965, 2020.

[29] Weijie Yuan, Zhiqiang Wei, Shuangyang Li, Jinhong Yuan, and Derrick Wing Kwan Ng. Integrated sensing and communication-assisted orthogonal time frequency space transmission for vehicular networks. *IEEE Journal of Selected Topics in Signal Processing*, 15(6):1515–1528, 2021.

[30] Shuangyang Li, Weijie Yuan, Chang Liu, Zhiqiang Wei, Jinhong Yuan, Baoming Bai, and Derrick Wing Kwan Ng. A novel isac transmission framework based on spatially-spread orthogonal time frequency space modulation. *IEEE Journal on Selected Areas in Communications*, 40(6):1854–1872, 2022.

[31] Tomasz P. Zieliński, Pavel Karpovich, Karol Abratkiewicz, Radosław Maksymiuk, Piotr Samczyński, Krzysztof Duda, and Marek Wypich. Wireless otfs-based integrated sensing and communication for moving vehicle detection. *IEEE Sensors Journal*, 24(5):6573–6583, 2024.

[32] O. Zacharia and M. Vani Devi. Fractional delay and doppler estimation for otfs based isac systems. *IEEE Wireless Communications and Networking Conference (WCNC)*, pages 1–6, 2023.

[33] T. Liang W. Yuan G. Lei, Y. Qiao and T. Zhang. Low-complexity channel estimation in otfs systems with fractional effects. *IEEE Wireless Communications Letters*, pages 1–6, 2025.

[34] A. S. Sümer S. E. Zegrar and H. Arslan. Fractional delay and fractional doppler estimation and mitigation framework in otfs systems. *IEEE Transactions on Vehicular Technology*, 2:2884–2896, 2025.

[35] Pavel Karpovich and Tomasz P. Zieliński. Integrated sensing and communication using random padded otfs with reduced interferences. *Sensors*, X(Y):p1–p2, 2025.

[36] Emanuele Viterbo Yi Hong, Tharaj Thaj. *Delay-doppler communications*. Academic Press, 2022.

[37] G. D. Surabhi and A. Chockalingam. Low-complexity linear equalization for otfs modulation. *IEEE Communications Letters*, 24(2):330–334, 2020.

[38] Zhou Zhou, Lingjia Liu, Jiarui Xu, and Robert Calderbank. Learning to equalize otfs. *IEEE Transactions on Wireless Communications*, 21(9):7723–7736, 2022.

[39] P. Karpovich, T.P. Zielinski, R. Maksymiuk, P. Samczyński, K. Abratkiewicz, and P. Tomikowski. Field tests of a random-padded otfsm waveform in a joint sensing and communication system. In *ICC 2023 - IEEE International Conference on Communications*, pages 6442–6448, 2023.

[40] P. Karpovich, T.P. Zielinski, R. Maksymiuk, K. Abratkiewicz, P. Tomikowski, and P. Samczyński. Experimental testing of an otfs-modulated waveform in a joint radar-comm system. In *2023 IEEE Radar Conference (RadarConf23)*, pages 1–6, 2023.

[41] Pavel Karpovich and Tomasz P. Zielinski. Channel estimation and equalization in otfs transmission system with random padding. In *2023 Signal Processing Symposium (SPSympo)*, pages 67–72, 2023.

[42] Pavel Karpovich and Tomasz P. Zieliński. Vehicle detection in 6g systems with otfs modulation — detekcja pojazdów w systemach 6g z modulacją otfs. *Przegląd Telekomunikacyjny, Wiadomości Telekomunikacyjne*, 96(4):73–76, 2023. Accessed: 2023-09-29. Conference: Konferencja Radiokomunikacji i Teleinformatyki KRiT 2023, 20–22 września 2023, Kraków. Affiliations: Nokia Solutions and Networks, Kraków.

[43] Pavel Karpovich and Tomasz P. Zielinski. Integrated sensing and communication using random padded otfs with reduced interferences. *Sensors*, 25(15), 2025.

[44] Saif Khan Mohammed, Ronny Hadani, and Ananthanarayanan Chockalingam. *OTFS Modulation: Theory and Applications*. Wiley-IEEE Press, November 2024.

[45] R. Hadani; S. Rakib; M. Tsatsanis; A. Monk; A. J. Goldsmith; A. F. Molisch; R. Calderbank. Orthogonal time frequency space modulation. In *2017 IEEE Wireless Communications and Networking Conference (WCNC)*, 2017.

[46] Tianyao Ma, Yin Xu, Xiaowu Ou, Yihang Huang, Dazhi He, and Wenjun Zhang. Iterative channel estimation for otfs using zc sequence with low peak-to-average power ratio. In *ICC 2023 - IEEE International Conference on Communications*, pages 2276–2281, 2023.

[47] John G. Proakis and Masoud Sakehi. *Digital Communications*. McGraw-Hill Higher Education, 5th edition, 2007.

[48] A. F. Molisch. *Wireless Communications*. John Wiley & Sons Ltd., 2011.

[49] Shashank Tiwari, Suvra Sekhar Das, and Vivek Rangamgari. Low complexity lmmse receiver for otfs. *IEEE Communications Letters*, 23(12):2205–2209, 2019.

[50] Qi Li, Jinhong Yuan, and Hai Lin. Iterative mmse detection for orthogonal time frequency space modulation. In *2022 IEEE International Conference on Communications Workshops (ICC Workshops)*, pages 01–06, 2022.

[51] Zhenduo Wang, Zhipeng Liu, Fangyuan Xing, Rongchen Sun, and Xiaoyan Ning. Low complexity mmse-sic receiver for otfs in high-speed mobile scenarios. *IEEE Communications Letters*, 28(3):667–671, 2024.

[52] P. Raviteja, Khoa T. Phan, Yi Hong, and Emanuele Viterbo. Interference cancellation and iterative detection for orthogonal time frequency space modulation. *IEEE Transactions on Wireless Communications*, 17(10):6501–6515, 2018.

[53] Weijie Yuan, Zhiqiang Wei, Jinhong Yuan, and Derrick Wing Kwan Ng. A simple variational bayes detector for orthogonal time frequency space (otfs) modulation. *IEEE Transactions on Vehicular Technology*, 69(7):7976–7980, 2020.

[54] Shuangyang Li, Weijie Yuan, Zhiqiang Wei, Jinhong Yuan, Baoming Bai, Derrick Wing Kwan Ng, and Yixuan Xie. Hybrid map and pic detection for otfs modulation. *IEEE Transactions on Vehicular Technology*, 70(7):7193–7198, 2021.

[55] F.R. Kschischang, B.J. Frey, and H.-A. Loeliger. Factor graphs and the sum-product algorithm. *IEEE Transactions on Information Theory*, 47(2):498–519, 2001.

[56] K. R. Murali and A. Chockalingam. On otfs modulation for high-doppler fading channels. In *2018 Information Theory and Applications Workshop (ITA)*, pages 1–10, 2018.

[57] Shuangyang Li, Weijie Yuan, Zhiqiang Wei, and Jinhong Yuan. Cross domain iterative detection for orthogonal time frequency space modulation. *IEEE Transactions on Wireless Communications*, 21(4):2227–2242, 2022.

[58] Martin Braun. Ofdm radar akgorithms in mobile communication networs. 2014.

[59] Marek Wypich and Tomasz P. Zielinski. 5g nr based radar-on-demand using channel impulse response estimate. In *2023 Signal Processing Symposium (SPSympo)*, pages 220–225, 2023.

[60] F. Colone, D. W. O'Hagan, P. Lombardo, and C. J. Baker. A multistage processing algorithm for disturbance removal and target detection in passive bistatic radar. *IEEE Transactions on Aerospace and Electronic Systems*, 45(2):698–722, 2009.

[61] Daniel W. O'Hagan, Motlatsi Setsubi, and Stephen Paine. Signal reconstruction of dvb-t2 signals in passive radar. In *2018 IEEE Radar Conference (RadarConf18)*, pages 1111–1116, 2018.

[62] Pavel Karpovich, Sviatoslav Kareneuski, and Tomasz P. Zieliński. Practical results of drone detection by passive coherent dvb-t2 radar. In *2020 21st International Radar Symposium (IRS)*, pages 77–81, 2020.

[63] K.M. Siegel et al. Bistatic radar cross sections of surfaces of revolution. *Journal of Applied Physics*, 26:297–305, 1955.

[64] Nikolas J. Willis. *Bistatic Radar*. Scitech, 2005.

[65] El Abbadi Jamal Youssefi My Abdelkader. Optimal spacing design for pilots in ofdm systems over multipath fading channels. *Communications and Network*, (2):221–229, 2010.

[66] David R. Brillinger. *Time Series Data Analysis and Theory*. Society for Industrial and Applied Mathematics, 2001.

[67] Kwapien S. Hitczenko P. On the rademacher series. *Probability in Banach Spaces. Progress in Probability*, 35(12):31–36, 1994.

[68] *Wireless Communication and Networking*. Prentice Hall, 2003.

[69] Adolf Finger Hans-Jurgen Zepernick. *Pseudo Random Signal Processing*. John Wiley & Sons, 2005.

[70] Xiaoran Liu, Lei Zhang, Jun Xiong, Xiaoying Zhang, Li Zhou, and Jibo Wei. Peak-to-average power ratio analysis for ofdm-based mixed-numerology transmissions. *IEEE Transactions on Vehicular Technology*, 69(2):1802–1812, 2020.

[71] Vincent Savaux and Yves Louët. Papr analysis as a ratio of two random variables: Application to multicarrier systems with low subcarriers number. *IEEE Transactions on Communications*, 66(11):5732–5739, 2018.

[72] Won Yong Yang Chung G. Kang Yong Soo Cho, Jaekwon Kim. *MIMO-OFDM Wireless Communications with MATLAB*. John Wiley and Sons, 2010.

[73] Tiejun Wang, J.G. Proakis, E. Masry, and J.R. Zeidler. Performance degradation of ofdm systems due to doppler spreading. *IEEE Transactions on Wireless Communications*, 5(6):1422–1432, 2006.

[74] M. Russell and G.L. Stuber. Interchannel interference analysis of ofdm in a mobile environment. In *1995 IEEE 45th Vehicular Technology Conference. Countdown to the Wireless Twenty-First Century*, volume 2, pages 820–824 vol.2, 1995.

[75] *Time Series Data Analysis and Theory*. Austin, TX: Holt Rinehart and Winston, 1974.

[76] Alan V. Oppenheim. *Discrete-Time Signal Processing*. Prentice Hall, 1999.

[77] Leila Nasraoui. Advanced synchronization techniques for ofdm systems. *Signal and Image Processing*, 2015.

[78] Nikolaos D. Sidiropoulos Rama Chellappa Sergios Theodoridis, Fulvio Gini. *Academic Press Library in Signal Processing Communications and Radar Signal Processing*, volume 2. Elsevier, 1 edition, 2013.

[79] Steven M. Kay. *Fundamentals of Statistical Signal Processing: Estimation Theory*. Prentice Hall, 1993.

[80] *The Discrete-Time Fourier Transform and Discrete Fourier Transform of Windowed Stationary White Noise*. 2013.

[81] Yves Louet Vincent Savaux. Lmmse channel estimation in ofdm context: a review. *IET Signal Processing*, 2016.

[82] A.J. Viterbi. An intuitive justification and a simplified implementation of the map decoder for convolutional codes. *IEEE Journal on Selected Areas in Communications*, 16(2):260–264, 1998.

[83] Christoph Schwark and Diego Cristallini. Advanced multipath clutter cancellation in ofdm-based passive radar systems. In *2016 IEEE Radar Conference (RadarConf)*, pages 1–4, 2016.

[84] Shanglin Ye and Elias Aboutanios. An algorithm for the parameter estimation of multiple superimposed exponentials in noise. In *2015 IEEE International Conference on Acoustics, Speech and Signal Processing (ICASSP)*, pages 3457–3461, 2015.

Appendix A

Properties of the Zak Transform

The equations are written on the basis of [16].

1. Linearity:
$$\mathcal{Z}[ax(t) + by(t)](\tau, \nu) = a\mathcal{Z}[x(t)](\tau, \nu) + b\mathcal{Z}[y(t)](\tau, \nu) \tag{A.1}$$

2. The Zak transform is periodic in ν with period $\Delta f = 1/T$:
$$\mathcal{Z}[x(t)](\tau, \nu + m\nu_0) = \mathcal{Z}[x(t)](\tau, \nu), m \in \mathbb{Z} \tag{A.2}$$
ν_0 is the basis period, it is defined in the subsection 2.1.1.

3. Translation in time by $0 \leq \tau_0 \leq T$:
$$\mathcal{Z}[x(t + \tau_0)](\tau, \nu) = \mathcal{Z}[x(t)](\tau + \tau_0, \nu) \tag{A.3}$$
If $\tau_0 = mT$, $m \in \mathbb{Z}$, then
$$\mathcal{Z}[x(t + mT)](\tau, \nu) = e^{j2\pi mT\nu}\mathcal{Z}[x(t)](\tau, \nu) \tag{A.4}$$

4. Modulation by a complex sine wave with frequency ν_0:
$$\mathcal{Z}[e^{j2\pi\nu_o t}x(t)](\tau, \nu) = e^{j2\pi\nu_0\tau}\mathcal{Z}[x(t)](\tau, \nu - \nu_0) \tag{A.5}$$
If $\nu_0 = m\Delta f$, $m \in \mathbb{Z}$, then
$$\mathcal{Z}[e^{j2\pi\nu_o t}x(t)](\tau, \nu) = \mathcal{Z}[x(t)](\tau, \nu) \tag{A.6}$$

5. Joint translation by τ_0 and modulation by a complex sine wave with frequency ν_0 :
$$\mathcal{Z}[e^{j2\pi\nu_o t}x(t - \tau_0)](\tau, \nu) = e^{j2\pi\nu_0(\tau - \tau_0)}\mathcal{Z}[x(t)](\tau - \tau_0, \nu - \nu_0) \tag{A.7}$$

6. Conjugation:
$$\mathcal{Z}[x^*(t)](\tau, \nu) = \mathcal{Z}[x(t)](\tau, -\nu) \tag{A.8}$$

7. Symmetry:

$$\mathcal{Z}[x(t)](\tau,\nu) = \mathcal{Z}[x(t)](-\tau,-\nu) \text{ if } x(t) \text{ even, } \mathcal{Z}[x(t)](\tau,\nu) = -\mathcal{Z}[x(t)](-\tau,-\nu) \text{ if } x(t) \text{ odd.} \tag{A.9}$$

8. Product in time:

$$y(t) = h(t)x(t) \tag{A.10}$$

$$\mathcal{Z}[x(t)](\tau,\nu) = \sqrt{T}\int_0^T \mathcal{Z}[h(t)](\tau,u)\mathcal{Z}[x(t)](\tau,u-\nu)du \tag{A.11}$$

9. Convolution in time with changing channel $h(t,\tau)$:

$$y(t) = h(t,\tau) \star x(t) \tag{A.12}$$

$$\mathcal{Z}[y(t)](\tau,\nu) = \int_0^{\tau_p}\int_0^{\nu_p} e^{j2\pi(\tau-\theta)}\mathcal{Z}\{h(t,\tau)\}(\theta,u)x_{dd}(\tau-\theta,\nu-u)\,d\theta\,du. \tag{A.13}$$